Combinaison de la microscopie de fluorescence X et de l'imagerie X par contraste de phase pour l'imagerie clinique sub-cellulaire

Ewelina Kosior

UNIVERSITÉ DE GRENOBLE

THÈSE

Pour obtenir le grade de

DOCTEUR DE L'UNIVERSITÉ DE GRENOBLE

Spécialité : **Physique Appliquée**

Arrêté ministériel : 7 Août 2006

Présentée par

Ewelina Kosior

Thèse dirigée par **Dr Sylvain Bohic, HDR**
et Dr Peter Cloetens

préparée au sein **European Synchrotron Radiation Facility**
et de **l'École Doctorale de Physique**

Combined phase and X-ray fluorescence imaging at the sub-cellular level

Thèse soutenue publiquement le **19/02/2013**,
devant le jury composé de :

M. Laurent Charlet
Professeur, Université de Grenoble, Président

M. Philippe Moretto
Professeur, Directeur du Centre d'Etudes Nucléaires de Bordeaux Gradignan, Rapporteur

M. Stefano Lagomarsino
Directeur de recherche, CNR Rome, Rapporteur

M. Jean Michel Létang
Maître de Conférences, CREATIS INSA-Lyon, Examinateur

M. Sylvain Bohic
Chargé de Recherche, Université de Grenoble, Directeur de thèse

M. Peter Cloetens
Docteur, European Synchrotron Radiation Facility, Co-Directeur de thèse

Université de Grenoble
École Doctorale de Physique

Ewelina Kosior

Combined phase and X-ray fluorescence imaging at the sub-cellular level

PhD thesis

Committee
Prof. Laurent Charlet, Université de Grenoble
Prof. Philippe Moretto, Centre d'Etudes Nucléaires de Bordeaux Gradignan
Dr. Stefano Lagomarsino, CNR Rome
Dr. Jean Michel Létang, CREATIS INSA-Lyon
Dr. Sylvain Bohic, Université de Grenoble
Dr. Peter Cloetens, European Synchrotron Radiation Facility

Grenoble, 19^{th} February 2013

To my Parents
and to Jérôme

Abstract

The PhD project was based on X-ray imaging of biological material. Especially two techniques were exploited in this work: X-ray fluorescence and X-ray phase contrast imaging which were made at the ID22NI beamline of the European Synchrotron Radiation Facility in Grenoble, France. Apart from synchrotron-based techniques other experiments using Atomic Force Microscopy and Scanning Transmission Ion Microscopy were performed. The latter were used mostly for a calibration and comparison purpose. The combined use of X-ray fluorescence and X-ray phase contrast was applied for the absolute quantification of metals at the sub-cellular level and for radiation damage investigations. Apart from the combined use, the sensitivity for heavy metals detection of hard X-ray fluorescence is applied to a nanoparticles study.

Key words

synchrotron, X-ray imaging, fluorescence, phase contrast, sub-cellular level, correlative imaging, nanoparticles

Contents

Chapter 1

Introduction/ Introduction en français

Every discovery brings new opportunities of deepening our knowledge about the world around us. But could have Wilhelm Roentgen ever thought that the basic (X-ray) picture of his wife's hand from 1895 would evolve one day to a sophisticated and extremely detailed image? Probably not.

Roentgen was exploring the path of electrical rays passing from an induction coil through a partially evacuated glass tube. Although the tube was covered in black paper and the room was completely dark, he noticed that a screen covered in fluorescent material was illuminated by the rays. He later realised that other objects could be penetrated by these rays as well, for example a hand. The projected image of the left hand of his wife showed a contrast between the opaque bones and the translucent flesh. He later used a photographic plate instead of a screen, and an image was captured. At that period of time the enigmatic and thus also exciting, new kind of radiation was named the X radiation.

Clearly visible hand's bones and the wedding ring (Fig.1.1) amazed the scientists and provoked further investigations with this unknown radiation. First radiology departments started to appear, like the one at the Glasgow Royal Infirmery. A number of remarkable X-ray images were made there: an X-ray of a kidney stone, an X-ray showing a penny in the throat of a child, etc. New possibilities were discovered, not only to image the body parts but also to treat cancers or skin diseases. By the early 1900s

Figure 1.1: Hand mit Ringen (Hand with Rings): print of Wilhelm Roentgen's first "medical" X-ray of his wife's hand. Source:Wikipedia

the damaging qualities of X-rays were demonstrated as powerful enough to fight these problems. However at the beginning it was not obvious that besides fighting diverse diseases one should consider as well protecting oneself from harmful exposures.
How do we stand nowadays, after more than 100 years from an extraordinary discovery?
If you would like to ask anybody at the street what do they know about X-rays, the answer would probably consists of words: hospital and injuries. This is a common opinion, almost everybody had to at least once exposure their body to X-rays during medical check. But if these people could visit a synchrotron source, such as European

Synchrotron Radiation Facility (ESRF) in Grenoble, their opinion would certainly become richer.
ESRF is the most powerful (also the biggest) synchrotron source in Europe. It offers a brightness, energy range and resolution unachievable with conventional (laboratory) radiation sources. As its possibilities are tremendously higher than the ones assured by conventional sources, also the research is more various.
It is not anymore only a question about exposing one's body in order to settle a diagnosis (like at the hospital). It is about a large range of possible scientific applications and explorations using X-ray properties of the synchrotron radiation. At the ESRF there is a room for (almost?) everyone. Physicists work together with chemists, material scientists, biologists, medical doctors, geophysists, paleontologists, protein crystalographers... Even industry will find the synchrotron source useful for their investigations.
X-rays are used to study the structure, growth processes and morphology of surfaces. They are used to study material behaviours at very high pressures, to reveal the crystal structure by powder diffraction and to "see" the structure of proteins. Finally they are used for biomedical applications at very high resolution (50 nm) like it is done at ID22NI, where most of this Ph.D. project was performed.
The ID22NI nano-imaging end-station is dedicated to hard X-ray micro-analysis and consists of the combination of X-ray fluorescence and 2D/3D X-ray phase imaging techniques. While X-ray fluorescence (XRF) reveals the chemical composition of the scanned sample, the phase imaging completes the view by adding relevant information about the structure of the sample. Both these techniques are exploited in this Ph.D. project in order to deal with some fundamental questions. One of them is the need of knowing the absolute metal concentration at the sub-cellular level, that up to now was not possible with the common accepted quantification methods. They were based on some assumptions on the matrix density and thickness as well as a matrix-match certified X-ray fluorescence standard material. Nowadays as technological developments accelerate and as research is performed at the nanoscale, the standards established years ago at the microlevel are not necessarilly relevant anymore. It is very important to be as close as possible to the real value of metal concentration. This challenge can be reached with the ID22NI beamline and is explained in this work.
Another possibility to get the most out of combining two imaging techniques is to study radiation effects on the cell. No doubt while sample is expose to intense X-ray nanobeam some damages due to irradiation occur. This fact can be easily recognized

when comparing radiographs of an object before the irradiation (occured during the fluorescence scan) and after it. It is also one of the significant problems - how to deal with radiation effects when pushing the X-ray science to the cutting edge.
Apart from combining both techniques they can serve independently as well. As ID22NI is a hard X-ray energy beamline thus XRF analysis can identify heavy metals such as gold (Au) and platinum (Pt) which are widely used in nanoparticles for targeting cancer cell and cancer therapy.
Summarizing: That was a long way from an extraordinary discovery of Wilhelm Roentgen until sophisticated machinery used nowadays to reach the unreachable and to see the invisible. Basic image of human hand converted into extremely detailed and quantitative picture of cellular structure and chemical composition. And likely it is not yet the end of this process.

The Ph.D. work is built as follows:
Chapter 2 describes the characteristics of synchrotron radiation, X-ray interaction with matter and X-ray focusing optics.
Chapter 3 describes synchrotron based X-ray fluorescence imaging.
Chapter 4 describes theory of X-ray phase contrast imaging.
Chapter 5 explores the combination of both techniques described in previous Chapters to image biological samples. Different objects (bacteria E.coli, HEK293 cells) are investigated in this chapter.
Chapter 6 describes the combination of X-ray fluorescence and X-phase to access absolute metal mass fraction (called also concentration in this manuscript) at the subcellular level. Our approach is compared to alternative methods like Scanning Transmission Ion Microscopy and Atomic Force Microscopy. The validation of our method is presented as well.
Chapter 7 presents a study on X-ray radiation effects on cell using ID22NI nanobeam. For these investigations freeze-dried PC12 cells were used.
Chapter 8 presents a study on MRC5 cells incubated with gold and platinum nanoparticles targeting the cell nucleus with the aim to treat tumour.
Chapter 9 summarizes the research and points perspectives.

Introduction en français

Chaque découverte représente une opportunité d'approfondir notre connaissance du monde qui nous entoure. William Roentgen pouvait il lui-même réaliser à son époque, en 1895, découvrant le profil laissé par la main de son épouse, qu'une imagerie par rayon X très sophistiquée et d'une extrême précision, puisse un jour révéler tout autant des détails dépassant l'échelle subcellulaire, et bien au delà encore?
En 1895, Roentgen étudie le phénomène du passage d'un courant électrique à travers un gaz sous basse pression. Il observe qu'à la décharge d'un tube, complètement enrobé de carton noir, scellé pour en exclure toute lumière et ceci dans une chambre noire, un carton couvert d'un côté de baryum platino-cyanide devient fluorescent lorsqu'il est frappé par les rayons émis du tube. Il réalisa par suite, de même que sa main, que d'autres objets étaient également des corps susceptibles d'êtres traversés par ces radiations. Il expérimente avec la main de son épouse placée sur le parcours des rayons puis s'aperçoit au développement, que les os sont entourés d'une pénombre qui représente la chair de la main, la chair est donc plus perméable aux rayons. La nature de ces rayons est encore inconnue et il leur donne le nom de rayons X . L'image capturée sur une plaque photographique est l'ombre des os de la main de son épouse, son alliance y étant visible. Les détails anatomiques observés étaient si époustouflant, que des investigations furent poussées en avant par les scientifiques.
Les premiers départements radiologique virent ainsi le jour, fondés comme ce fut le cas à l'Hospital Royal de Glasgow, à l'origine d'une remarquable série d'images radiographiques : une image représentant un kiste rénal, celle montrant une piéce de monnaie restée bloquée dans l'oesophage d'un enfant, et ainsi etc ... De nouvelles possibilités furent découvertes, non seulement pour révéler les parties du corps, mais également pour proposer des méthodes de traitement à des cancers, ou à des maladies de l'épiderme. Furent démontrées dans les débuts du 20.ème siècles, l'efficacité des rayons-X à combatte ces problèmes médicaux, et à gagner les tissus vivants au moyen de leurs propriétés non invasives. Néanmoins initialement, il n'apparaissait pas évident qu'avec une exposition si fréquente à ces rayons (pendant longtemps, les doses étaient trop fortes), était dangereuse et qu'il y avait une nécessité de s'en protéger, notamment à l'occasion de tels traitements.

Mais de nos jours, suite à plus de 100 ans après cette extraordinaire découverte, où en sommes nous donc arrivés ? En posaant cette question dans la rue sur ce qu'il est connu des rayons X, une réponse sommaire et unanime consisterai probablement en ces mots : fractures et hopital. Ceci n'étant qu'une opinion communément partagée, car d'aucun eu pour généralement, le moins à une occasion, de faire l'objet en propre, lors d'un examen médical, d'une radiographie. Et si ces personnes pouvaient rendre visite aux installation d'une source X tel qu'un synchrotron, comme en est à l'European Synchrotron Radiation Facility (ESRF) se trouvant à Grenoble, leurs notions quant à l'utilisation des rayons X s'en trouveraient grandement étendues.
Le Synchrotron ESRF est une source de rayons X la plus énergétique (et la plus grande installation) en Europe. De plus elle offre un flux inégalé sur une large gamme d'énergie de rayons X et permet d'obtenir des faisceaux d'une taille à ce jour inatteignable par d'autres (en laboratoire) sources conventionnelles. Ainsi, ce type de source offre des possibilités nouvelles de recherches et d'exploration de la matière couvrant de nombreux domaines divers et variés de la science.
Chacun ou presque peut y trouver une place pour mener ses recherches dans son champ scientifique. Sur ce type d'installation des physiciens coopérent avec des chimistes, des chercheurs experts en matériaux, des biologistes, médecins, géophysiciens, paléontologues, cristallographes..., et même l'industrie y trouve une grande utilité pour ses études de recherches et développement.
Les rayons X permettent l'étude de structures, d'étudier la dynamique de processus, l'étude de surfaces. Ils sont très utiles pour l'étude des matériaux à hautes pressions, pour la diffraction des matériaux ou la diffraction de structures protéiques.
S'y trouvent enfin les dispositifs d'expérimentations tel que la ligne de lumière ID22NI notamment dédiée à des applications relevant du domaine de l'imagerie biologique à haute résolution spatiale (50 nm).
Il est possible de travailler à de hautes énergies (rayons X durs) et combinant des techniques d'imagerie par fluorescence X et d'imagerie X de phase 2D/3D. Tandis que la fluorescence par rayons X (XRF) révèle la composition chimique de l'échantillon à l'étude, l'imagerie de phase complète l'analyse en révélant des informations additionnelles concernant la structure détaillée de cet échantillon. Ces deux techniques d'imagerie sont exploitées dans ce projet doctoral afin de proposer un moyen de quantifier de manière absolue les éléments chimiques au niveau subcellulaire. Actuellement les méthodes permettant une quantification à partir des données de fluorescence X nécessitent de faire

une hypothèse sur la densité et l'épaisseur de la matrice ou nécessitent des matériaux standards similaires à l'échantillon analysé et dont les concentrations en élément sont certifiés. Cependant, aux échelles sub-cellulaire (sub-100 nm) les standards d'ordre micrométrique établis voici quelques années ne suffisent plus. Il est ainsi très important d'approcher au plus près la valeur absolue de la concentration dans un endroit précis d'une cellule par exemple. L'approche proposée dans cette thèse et etudiée sur la ligne de lumière ID22NI de l'ESRF a pour objectif de répondre à ce verrou technologique.
Une autre possibilité d'application par ces techniques combinées d'imageries consiste en l'étude des effets de radiations sur des cellules. Des dommages se produisent indéniablement sur les échantillons exposés à d'intenses faisceaux de rayons X. Ceci peut être démontré en comparant des images de phase de cellules précédant et suivant l'irradiation d'un objet (c.à.d. l'influence d'un scan de fluorescence X). Ceci permet de contribuer à mieux comprendre les effets de ces irradiations sur les mesures qui sont collectées, ce qui devient primordial au fur et à mesure que les faisceaux de rayons X des sources synchrotron deviennent de plus en plus intenses et petits. Prises de manière séparée, ces deux techniques d'imagerie peuvent être utiles. Notamment, les hautes énergies (rayons X "durs") obtenues sur ID22NI permettent l'étude par XRF au niveau sub-cellulaire de la distribution quantitative de métaux lourds tel que l'or (Au) ou le platine (Pt) utilisés dans des nanoparticules ciblant les cellules tumorales avec des perspectives thérapeutiques en cancérologie. En résumé, ce fut un long cheminement depuis l'extraordinaire découverte de William Roentgen, jusqu'à des outils sophistiqués employés de nos jour pour rendre visible l'insondable. D'une radiographie X simple de la main, vers l'imagerie quantitative de précision détaillant l'extrême finesse de structures cellulaires, beaucoup de chemin a été parcouru et avec à la clé, de nouvelles possibilités d'imagerie chimique d'objets biologiques.

Ce travail doctoral est structuré de la manière suivante:
Le chapitre 2 décrit les caractéristiques du rayonnement synchrotron, les interactions des rayon X avec la matière, et l'instrumentation permettant la focalisation de ces rayons X.
Le chapitre 3 décrit l'imagerie par fluorescence X.
Le chapitre 4 décrit l'imagerie X par contraste de phase.
Le chapitre 5 explore différentes analyses combinant les techniques de fluorescence X

et dimagerie X de phase décritent aux chapitres 3 et 4 pour l'imagerie d'objets biologiques.
Le chapitre 6 présente l'étude combinant fluorescence X et imagerie X de phase pour l'imagerie quantitative absolue délément l'échelle sub-celulaire. Notre approche a été comparé à celle d'une technique complémentaire : la microscopie ionique en transmission.
Le chapitre 7 présente une étude sur les effets de l'irradiation de cellules analysées par la nanosonde de fluorescence X ID22NI.
Le chapitre 8 présente une étude sur des cellules incubées avec des nanoparticules d'or et de platine ciblant leur noyau en vue d'applications pour le traitement des tumeurs.
Le chapitre 9 constitue un résumé des recherches menées et propose des perspectives.

Chapter 2

Synchrotron radiation

When electrons or positrons are moving at relativistic speed, i.e., close to the velocity of light, they are subjected to a magnetic field, the trajectory follows a circular orbit and synchrotron radiation (SR) is emitted in the tangential direction. The radiated energy is proportional to the fourth power of the particle speed and inversely proportional to the square of the radius of the path. The beam is concentrated into a forward narrow cone with half angle of typically 0.1 to 1 mrad. Synchrotron radiation facilities typically consist of an injection system, a storage ring and beamlines. In the injection system, electrons are generated, pre-accelerated, and sometimes a second accelerator further accelerates these electrons to few GeV before injection into the storage ring. At ESRF, the electrons are accelerated to a nominal energy of 6 GeV. In the ring, bunches of electrons periodically circulate at relativistic speed for periods of up to many hours. The storage ring consists of radio-frequency (RF) cavities, bending magnets, other magnets, insertion devices and different control systems mainly to control the orbit of the electrons (Fig.2.1). The RF cavity system restores energy, which the electrons lose because of the emission of SR, and stabilizes the bunch of electrons. The high energy electrons are maintained in a planar orbit by using bending magnet. Synchrotron radiation is emitted when an electron received centripetal force in the magnetic field of the bending magnets. Synchrotron radiation emitted from an electron traveling at almost the speed of light is highly collimated by relativity effect. Higher brightness synchrotron radiation is produced by insertion devices, such as undulators and wigglers, in the straight sections of the storage ring. They have the common feature of

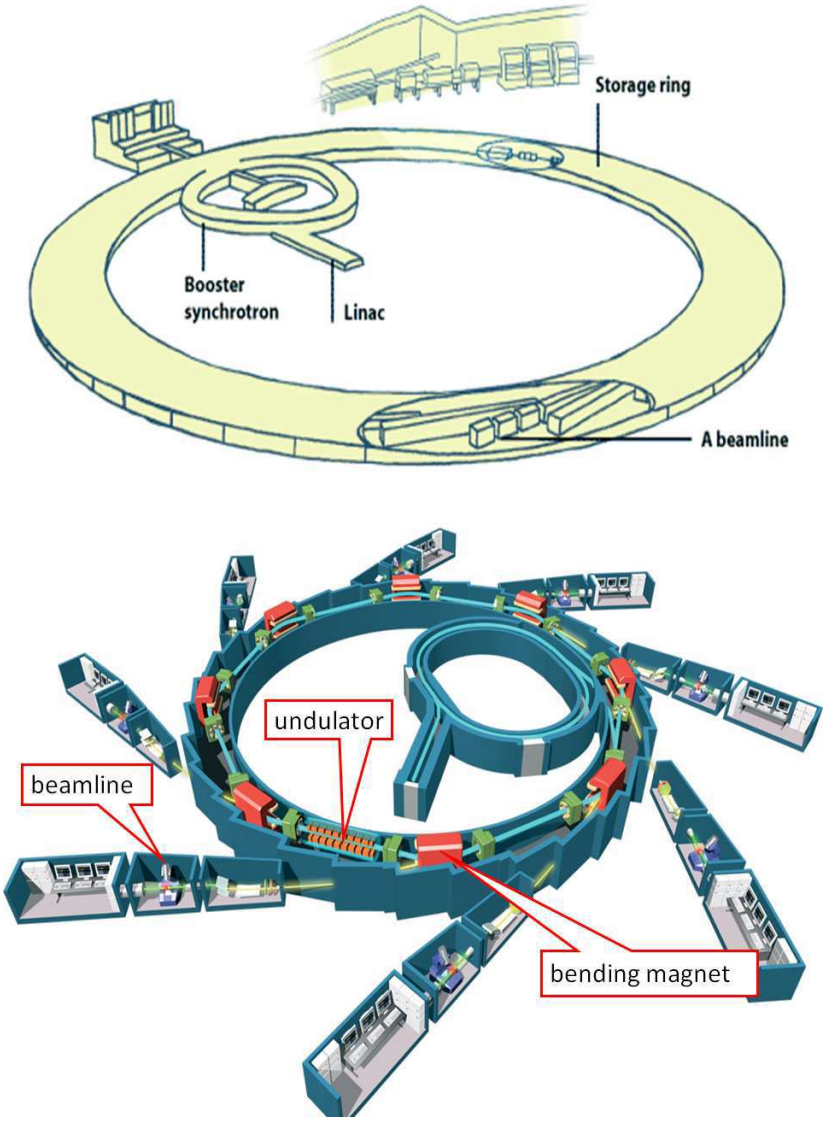

Figure 2.1: Schematic picture of the synchrotron ring of the ESRF (up) and more detailed view (bottom). Electrons are first accelerated in the linear accelerator (linac) and in a booster synchrotron, then they are injected into a storage ring.

producing synchrotron radiation by passing relativistic electron bunches through periodic magnetic structures [1]. The most powerful generators of synchrotron radiation at most modern storage rings are undulators.
The magnetic structure of today's most common (planar) undulator is an array of closely spaced vertically oriented dipole magnets of alternating polarity. As the electron beam passes through the array, it's trajectory oscillates in the horizontal plane. Owing to the relatively weak field, the radiation cones emitted at each bend in the trajectory overlap, giving rise to a constructive interference effect that results in one or a few narrow peaks (a fundamental and harmonics) in the energy spectrum of a beam that is highly collimated in both the horizontal and vertical directions. Tuning the wavelengths of the harmonics is done by mechanically adjusting the vertical spacing (gap) between the pole tips.
The wiggler is often used as a source in order to increase the flux at higher energies (shorter wavelengths). Wigglers are similar to undulators but generally have higher magnetic fields and fewer dipoles, with the result that they produce a continuous spectrum with a higher flux and a spectrum that extends to shorter wavelengths than bending magnets. Despite the similarity, wigglers evolved independently from undulators at the start. Indeed, most scientific experiments usually only need a very narrow range of wavelengths and therefore most of the wiggler radiation power remains unused leading to unwanted heat production within the optical devices.

2.1 Characteristics of synchrotron radiation

2.1.1 Brightness, brilliance and flux

The brightness is the phase-space density of the photon flux [2], evaluated in the forward direction and at the center of the source, i.e., at the origin of the phase space, as follows

$$\mathcal{B}\,[\frac{photons}{(sec)(mm^2)(mrad^2)(0.1\%bandwidth)}] = \frac{d^4\mathcal{F}}{d\theta d\psi dx dy}\ , \tag{2.1}$$

where bandwidth is described as $\delta\lambda/\lambda$. Here $\mathcal{F}$ is the spectral flux, θ and ψ are the horizontal and vertical angles and x, y are the horizontal and vertical coordinates respectively. This quantity is sometimes also called brilliance.

It is possible to obtain spatial or angular density of flux respectively by integrating the phase space density over the angles or the position coordinates:

$$\frac{d^2\mathcal{F}}{dxdy} = \int \frac{d^4\mathcal{F}}{d\theta d\psi dxdy} d\theta d\psi \tag{2.2}$$

$$\frac{d^2\mathcal{F}}{d\theta d\psi} = \int \frac{d^4\mathcal{F}}{d\theta d\psi dxdy} dxdy \tag{2.3}$$

Finally, one obtains the spectral flux by integration, as follows:

$$\mathcal{F}\ [\frac{photons}{(sec)(0.1\%bandwidth)}] = \int \frac{d^2\mathcal{F}}{dxdy} dxdy = \int \frac{d^2\mathcal{F}}{d\theta d\psi} d\theta d\psi \tag{2.4}$$

Some notable properties of synchrotron radiation produced by synchrotron light sources are including:

- high brightness (the emitted flux per solid angle per unit source area), which is the case when the beam size and its divergence is as small as possible while the photonflux remains as large as possible. It can be thousand of million-fold higher than conventional X-ray sources
- high intensity or flux (photons per second) over a large wavelength range.
- high brilliance, the brightness per unit source area
- high level of polarization
- small angular divergence of the beam (high collimation)
- low emittance (product of beam size and divergence)

2.1.2 Coherence

One of the important characteristics of the photon beam is the coherence, described as the degree to which the radiation can exhibit interference patterns [3]. There are two types of coherence [4]: transverse and longitudinal. The transverse coherence refers to the coherence of the electromagnetic disturbances at two points perpendicular to the propagation direction. It is related to the source size and the distance

source-experiment. Longitudinal coherence refers to the case of two points along the propagation direction and is related to the monochromaticity of the beam.
The transversely coherent flux is given by [5]

$$\mathcal{F}_{coh,T} = \mathcal{B}(\lambda/2)^2 \tag{2.5}$$

where λ is the wavelength.
The transverse coherence is characterized by the transverse coherence length. It is related to the angular source size α, the distance to the source L and source size s:

$$l_T = \frac{\lambda}{2\alpha} = \frac{\lambda s}{2L} \tag{2.6}$$

The longitudinal coherence is characterized by the longitudinal coherence length l_c which is related to the bandwidth $\delta\lambda/\lambda$ by

$$l_c = \lambda^2/\delta\lambda \tag{2.7}$$

2.2 X-rays interactions with matter

X-rays are appropriate for the study of matter at atomic level. This section considers the basic interactions of X-rays with matter such as X-ray absorption which produces photoelectrons, diffraction and scattering.

2.2.1 Absorption and photoelectric absorption

The absorption of the X-ray radiation by a material depends on the energy of the X-ray radiation and the following material parameters: thickness, density, atomic number, following the Beer-Lambert law

$$I(t) = I_0 e^{-\mu t} \tag{2.8}$$

where $I(t)$ is the intensity of the beam after traversing the material of thickness t (cm), I_0 is the initial intensity of the beam and μ (cm^{-1}) is the linear attenuation coefficient. It can be formulated as follows:

$$\mu = (N_A/A)\rho_m\sigma_a \tag{2.9}$$

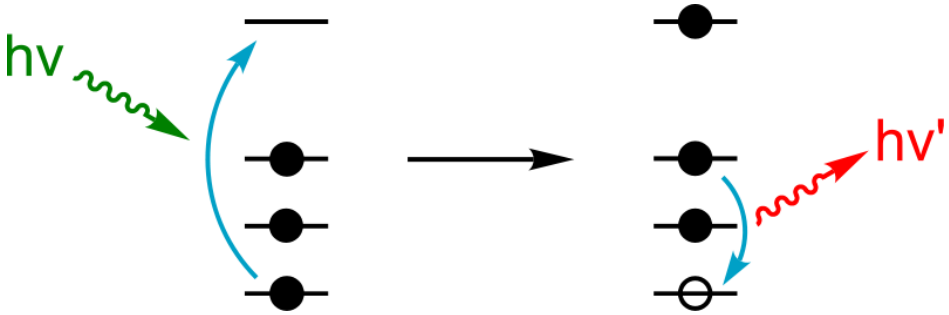

Figure 2.2: Schematic picture of the X-ray fluorescence. The inner shell electron hit by the energetic photon expels from the atom. The vacancy is filled by other electron and characteristic X-ray radiation is emitted.

where N_A is Avogadro's number, A the atomic weight, ρ_m the mass density and σ_a is the attenuation cross section. The attenuation coefficient can be described as linear attenuation coefficient (eq. 2.9) and as mass attenuation coefficient (μ_m). The first one is of more importance in X-ray optics due to the fact that it quantifies the amount of X-rays absorbed per unit length (unit: cm^{-1}) and depends on the physical and chemical state of the absorber as well as on the energy of the incident X-ray. The second one quantifies how much X-rays are absorbed per unit mass of material (unit: cm^2g^{-1}):

$$\mu_m = \mu/\rho_m = (N_A/A)\sigma_a \tag{2.10}$$

As said, when a sample is irradiated with X-rays, the X-rays may undergo either scattering or absorption by sample atoms. This later process is known as the photoelectric effect. When an atom absorbs the source X-rays, the incident radiation dislodges electrons from the innermost shells of the atom, creating vacancies. The electron vacancies are filled by electrons cascading in from outer electron shells. Electrons in outer shells have higher energy states than inner shell electrons, and the outer shell electrons give off energy as they cascade down into the inner shell vacancies. This rearrangement of electrons results in emission of X-rays characteristic of the given atom (Fig.2.2) or so called Auger electrons [6]. The emission of X-rays, in this manner, is termed X-ray fluorescence and emitted isotropically. In addition, each characteristic X-ray line is defined with the letter K, L, or M, which signifies which shell had the original vacancy and by a subscript alpha (α) or beta (β), which indicates the higher shell from which electrons fell to fill the vacancy and produce the X-ray. For example, a K_α line is

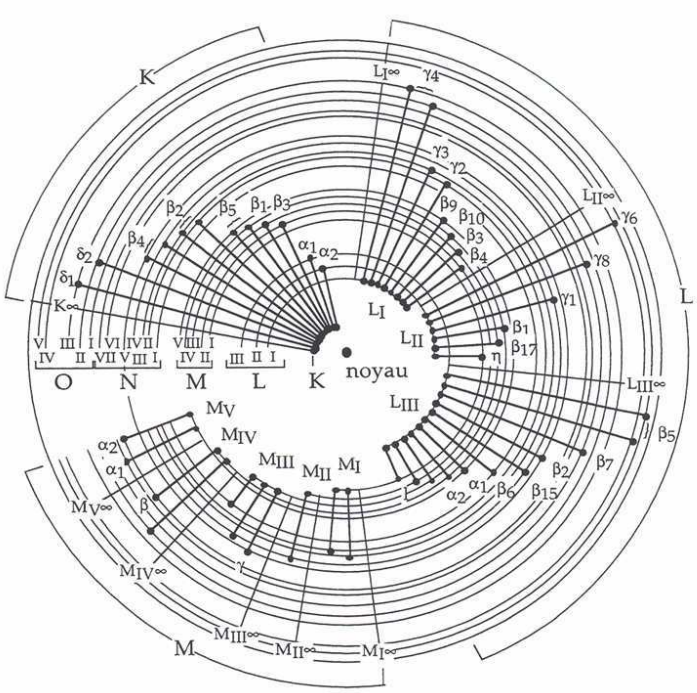

Figure 2.3: Transition levels and emmission lines nomenclature (IUPAC and Siegbahn nomenclature).

produced by a vacancy in the K shell filled by an L shell electron, whereas a K_β line is produced by a vacancy in the K shell filled by an M shell electron. The K_α transition is on average 6 to 7 times more probable than the K_β transition; therefore, the K_α line is approximately 7 times more intense than the K_β line for a given element, making the K_α line the choice for quantitation purposes. The K lines for a given element are the most energetic lines and are the preferred lines for analysis. For a given atom, the X-rays emitted from L transitions are always less energetic than those emitted from K transitions. (Fig.2.3)

2.2.2 Diffraction

X-ray diffraction (XRD) is a versatile, non-destructive technique that reveals detailed information about the crystallographic structure of materials. When a monochromatic X-ray beam with wavelength λ is projected onto a crystalline material at an angle θ,

diffraction occurs only when the distance traveled by the rays reflected from successive planes differs by a complete number n of wavelengths, according to the Bragg's law:

$$n\lambda = 2dsin\theta \tag{2.11}$$

where d is the distance between atomic layers in a crystal.
By varying the angle, the Bragg's Law conditions are satisfied by different d-spacings in polycrystalline materials. Plotting the angular positions and intensities of the resultant diffracted peaks of radiation produces a pattern, which is characteristic of the sample. Where a mixture of different phases is present, the resultant diffractogram is formed by addition of the individual patterns.

2.2.3 Scattering

Two kinds of scattering may take place when a photon interacts with an atom:

- incoherent or inelastic or Compton scattering; the change of propagation direction is accompanied with an increase of wavelength and a change of phase
- coherent or elastic or Rayleigh scattering; phase and energy are not affected

Elastic scattering

Elastic scattering takes place when the incident particles due to interaction with other particles/waves conserve their kinetic energy, while the propagation direction is changed. When considering I_0 as incident particles per unit area per sec., I_s as scattered particles withing the solid angle $\Delta\Omega$ and by use of differential scattering cross section $d\sigma/d\Omega$ one can formulate:

$$I_s = I_0 \Delta\Omega \frac{d\sigma}{d\Omega} \tag{2.12}$$

Inelastic scattering

In an inelastic scattering process the kinetic energy of incident particles is not conserved. One example of inelastic scattering is the Compton effect [7]. The X-rays of a

known wavelength interact with an atom and are scattered through an angle θ. The wavelength of scattered photons is related to θ:

$$\lambda' - \lambda = \frac{h}{m_e c}(1 - cos\theta) \tag{2.13}$$

where λ is an initial wavelength, λ' wavelength after scattering, h the Planck constant, m_e the electron rest mass and c is the speed of light.
The probability for Compton scattering increases with increasing photon energy (up to a certain level, then it decreases) and is proportional to atomic number of the scattering atom. Rayleigh scattering decreases with increasing energy and decreasing atomic number.

2.3 X-ray focusing optics

The third-generation synchrotron radiation sources provide hard X-ray beams with a flux higher than 10^8 photons per second. The availability of such high flux, coherent beams allow to apply the coherence-based techniques already developed for visible light or soft X-rays to the hard X-ray region. Coherent X-ray beams can be focused to very small (diffraction-limited) spot size by using different methods based on grazing incidence mirrors, Fresnel zone plates or compound refractive lenses. Also, total reflection of X-rays can be used for the confinement of X-rays using multiple reflections in a glass capillary. This approach will be not described here but is described elsewhere [8]. Similarly, X-ray waveguides that produces sub-100 nm X-ray beam are not described, but one can refer to major papers on this subject [9], [10]. Each method takes an advantage on another depending upon the application and the way how X-rays interact with matter.

2.3.1 Grazing incidence mirrors

Total external reflection mirrors were used, as one of the first, to focus X-rays. Albert Einstein [11] pointed out that X-rays should undergo total external reflection at grazing angles. This idea was taken up by Kirkpatrick and Baez in the design of the focusing system that bears their names. Their mean of use was based on reflectivity, being the

ratio of the intensity of the total radiation reflected from a surface to the total incident radiation on that surface [12]. To achieve the preferable spot size mirrors are bent to a specific shape. As shown in Fig.2.4, the so-called Kirkpatrick-Baez (KB) mirrors system were the first mirrors that were designed and employed for X-ray microscopy. Two orthogonal coated silicon substrates are bent into elliptical shapes by mechanisms based on flexure hinges. This device provides both very high accuracy and flexibility. It uses precise motors to tune the substrate shape to the experimental conditions such as focal distance and energy. Six degrees of freedom are needed for alignment and focusing. The length of the substrates of the systems developed ranges from 92 to 300 mm. The surface quality of the substrates and the reading accuracies have to be very high. Typically, the final shape can be obtained to within a few nanometres. In such system the astigmatism which results from the first mirror is compensated by that of the second mirror. It is very interesting in the hard X-ray regime where X-ray focusing is difficult to achieve with other optics. Also important for large bandwidth (large flux). Finally, the recent developments in the technology of shaping, polishing, mounting and aligning KB mirrors has lead to focusing X-ray beams to less than 10 nm [13]. One of the important advantages that mirrors have on other X-ray optics such as zone plates is that it is achromatic, meaning that the focal length is independent of energy, which is important in terms of spatially resolved X-ray absorption spectroscopy. It has large acceptance and up to 70-80% efficiency. The performance of grazing incidence mirrors is strongly dependent on the slope errors present on their reflecting surfaces. Slope errors are height errors or bumps that change the angle of the reflected X-rays. The larger the slope errors, the further the X-ray beam will be reflected off its intended path. The main limitations of mirrors are: they are relatively expensive, their performance depends on the quality of the surface of the mirror and the mechanics for dynamical bending of the mirrors is complex.

2.3.2 Fresnel zone plates

Zone plates can be regarded as circular diffraction gratings. Diffraction by gratings leads to constructive interference (of N-th order). Fresnel zone plates are made of plates with circular concentric ribs, alternating between opaque and transparent (Fig. 2.5). They are used to focus monochromatic beams. The focusing is possible due to

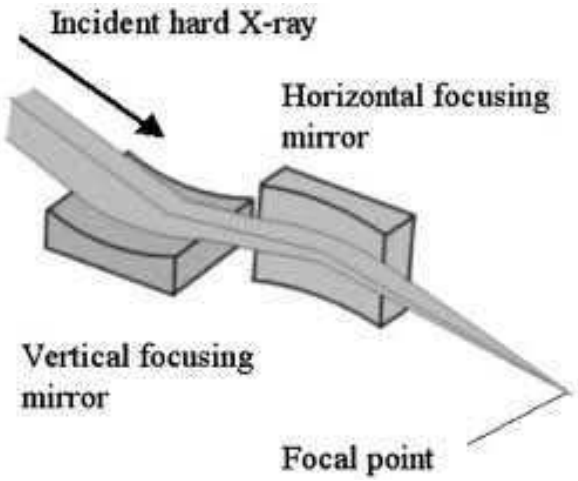

Figure 2.4: Schematic picture of KB optics system. Two orthogonally placed mirrors are focusing the incident beam vertically and horizontally. Source: Spring8

constructive interference of the waves diffracted by the different zones.
The radius of the zone is described by the formula

$$r_n^2 = Nn\lambda f + (Nn\lambda/2)^2 \tag{2.14}$$

where N is the diffractive order used for focusing, n the zone number, λ the wavelenth and f the focal length.
If the focal length is much bigger than the zone plate, the formula 2.14 can be simplified

$$r_n^2 \simeq Nn\lambda f \tag{2.15}$$

The width dr_n of the rings of the circular grating decreases with increasing radius r_n of the rings. Knowing the radius of the outermost ring and its width it is possible to calculate the focal length:

$$f = 2r_n dr_n/\lambda \tag{2.16}$$

The spatial resolution of a Fresnel zone plate is limited by the width of the outermost zone. This value is restricted by the technology (lithography) available to produce them. While lithography technology is developing one can expect an improvement in resolution of zone plates. Still sub-20 nm beam has been produced [14] and images can be created with high spatial resolution. One of the limitations are chromatic aberration, limited aperture size and the fact that their efficiency and resolution drop quickly at higher energies (above 15 keV).

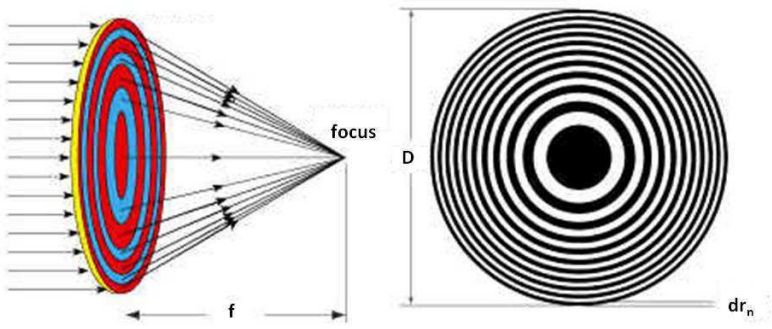

Figure 2.5: Schematic view of Fresnel zone plate which uses constructive interference of ligth from adjacent zones to form a focus. The focal lenth of a zone depends on its diameter D (being equal to $2r_n$) and the outermost zone width dr_n

2.3.3 Compound refractive lenses

Refractive lenses that are used in visible-light optics were considered as inappropriate for focusing X-rays. This is due to the fact that refractive index decrement, δ (see Chapter 4), is very small for X-rays in matter and the absorption effects are strong. To level this problem Yang [15] proposed to use low-Z elements to fabricate the lenses for focusing hard X-rays. Furthermore to face the problem of lens radii of only few micrometers, which is the case when considering low values of δ for low-Z material, Snigirev [16] proposed the construction of a compound refractive lens (CRL), consisting of a linear array of many simple lenses.
Focal distance of a single lens is described as

$$f = R/2\delta \tag{2.17}$$

where R is the radius of the lens. The value of the focal distance for the case of compound lens with N holes is divided by N resulting in an acceptable range for microfocus experiments.
The number of holes N increases linearly with R and quadratically with energy and is limited by the reasonable length of the array as well as the requirement of keeping the value of d (see Fig. 2.6) as small as possible. One of the advantages of compound refractive lenses are simplicity, relatively low cost and the fact that they do not change the beam path, which is the case for bent-mirror optics. Their alignment is straightforward and no bending mechanism is required. One of the limitations are chromatic aberration and the fact that the absorption in the lense material limits the aperture size and efficiency is limited by absorption.

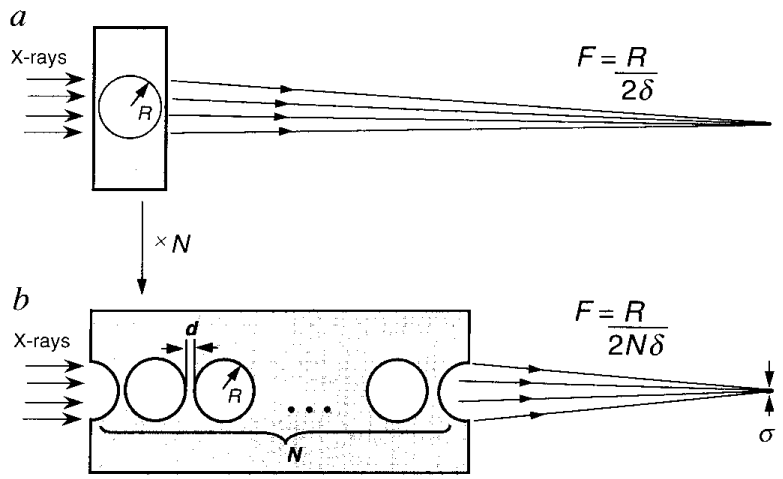

Figure 2.6: Schematic picture of compound refractive lens; a. a simple concave lens fabricated as a cylindrical hole in the material; b. a CRL made of N cylindrical holes, spaced between each other by the distance d. The focal length of a CRL is N times smaller than for the single lens. Source: A.Snigirev, Nature 1996

Résumé du Chapitre 2 en Français

Ce chapitre présente les principes théoriques du rayonnement X généré par un synchrotron tel que celui de l'ESRF. Les différents types d'interactions des rayon X avec la matière sont brièvement abordés et plus particulièrement le principe de la fluorescence X. Les différents systèmes de focalisation des rayons X sont décrits notamment le principe de la focalisation par des optiques réflectives de type miroirs en configuration Kirkpatrick-Baez comme ceux utilisés sur la station de nanoimagerie X ID22NI sur laquelle cette thése a été conduite.

Chapter 3

Synchrotron X-ray fluorescence imaging

3.1 Principles

Synchrotron x-ray fluorescence (XRF) imaging is a powerful technique which exploits the spectrally pure and finely focused X-ray beam from a synchrotron. It has opened up new application modes such as trace element analysis, surface analysis, chemical state analysis and microanalysis [17]. Digital images of microscopic or nanoscopic samples are built, pixel by pixel, by scanning the sample through the beam. The resulting X-ray fluorescence radiation is characteristic of the chemical elements at that pixel. Mathematical deconvolution of the fluorescence spectrum reveals the chemical composition, from which quantitative elemental images of the sample are assembled. They are often displayed as false-colour maps. The combination of high flux and low emittance provided by synchrotron sources has proved to be crucial for the enormous success of experiments in the field of synchrotron-based X-ray fluorescence. It can be applied to solid, powdered and liquid samples. Special attention deserves the application to biomedical research as it provides robust qualitative data about the behaviour and effect of metals and metalloids. The mapping capability essentially provides a picture of the elemental distribution within the material, which very easily provides a tremendous amount of information. In biological applications the maps may give a

direct and clear observation of element occurrences in different regions of the sample. Elemental maps depicting the subcellular distribution and concentration of a certain element have great potential in biomedical research, thanks to a low detection limit and the high spatial resolution of synchrotron X-ray fluorescence microscopy.
Why is this of importance for the biomedical field?
First, living systems, for survival, depend on their ability to accumulate, release and use certain elements, particularly metal ions, to define a certain composition that is held constant within a given homeostatic state. Secondly, several essential metal ions participate in the control of numerous metabolic and signaling pathways, but their rich coordination chemistry and redox properties confer them a propensity to randomly coordinate and catalytically react inside the cell with protein sites other than those tailored for that purpose. Indeed, about one third of all structurally characterized proteins are metalloproteins and bind metal ions or co-factors, which play a pivotal role in the structure function relationship of proteins and other bio-molecules. In addition, all these cellular essential metals are also potentially toxic. Thus, a number of sophisticated networks of trafficking pathways are available to tightly regulate their uptake, intracellular transport and compartmentalization, and to avoid their toxic side effects. Third, in spite of all the progress made, we are still merely on the brink of understanding these processes. Consequently, synchrotron microspectroscopy techniques contribute to elucidating the distribution, concentration and chemical state of metals inside tissues and cells at the organelle level. This contribution is not only highly challenging but represents important objectives in modern analytical chemistry and an essential step towards the precise understanding of some cellular physiopathological or toxicological processes.
To probe the sub-cellular complexity of metal ion homeostasis mechanisms, one requires sub-micrometer resolution together with a sub-femtogram absolute detection limits due to the decreasing quantity of sample probed. X-ray fluorescence analysis with a nanoprobe is the most direct and sensitive method to quantify the distribution of metals and other elements at the sub-cellular level [18], [19]. It provides high sensitivity for transition metals and other relevant trace elements together with the capability of penetrating and mapping whole cells. In the present work we will be mostly interested in biological matrix that is made of low atomic number (Z) elements (carbon, oxygen, hydrogen, nitrogen). This is low scattering material resulting in low spectral baselines that favour a higher sensitivity. There is also signicantly less self-absorption

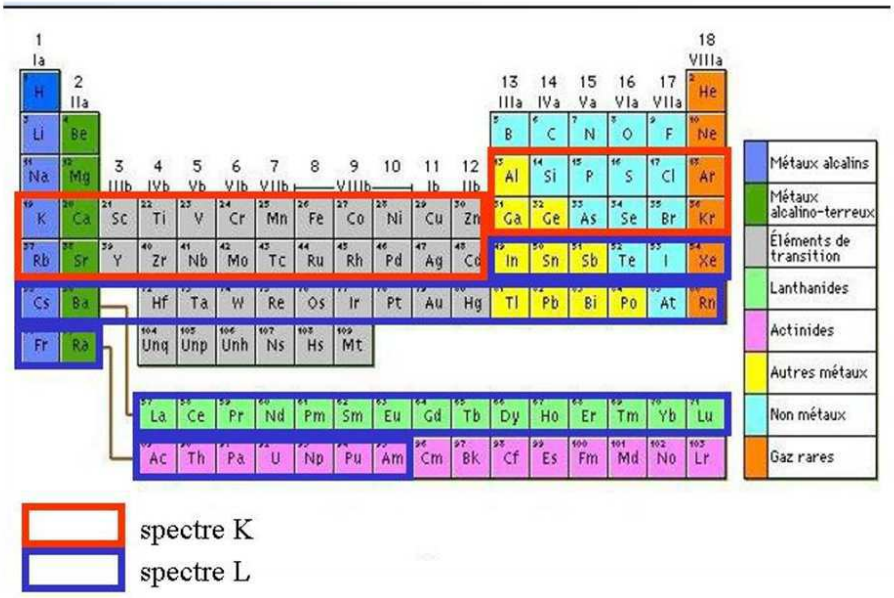

Figure 3.1: The elements accessible for the XRF analysis on the ID22 beamline. In red K-lines and in blue L-lines.

of X-rays by such sample. Thus the detection of high Z elements in such matrix can be considered as the most favourable case for synchrotron X-ray fluorescence imaging. Regarding the beamline ID22NI where this project was made, the elements accessible during the XRF analysis are shown on the Fig.3.1. Although powerful, synchrotron XRF imaging is traditionally slow (100 ms or more per pixel). Its pixel-by-pixel nature, low sensitivity and slow readout of conventional energy dispersive X-ray detectors, and the significant data processing task severely limits the size of images that can be made during a researcher's limited synchrotron time (for example acquiring images of just 200 x 200 pixels with a dwell time of 100 ms would take more than 1 h).
The advantages of synchrotron-based XRF over conventional XRF derive directly from the characteristics of synchrotron radiation (see Chapter.2). While comparing synchrotron-based XRF analysis with other alternative possibilities one must highlight the much higher sensitivities and lower detection limits achievable at synchrotron light sources. The sensitivity, defined as the detected signal intensity from a unit mass per unit of time, is proportional to the incident X-ray intensity. It can be sufficiently

enhanced due to the photon flux density, which at synchrotron sources is modulable through focusing. Also the high degree of polarization of synchrotron radiation is beneficial, causing spectral backgrounds due to scatter to be greatly reduced when the detector is placed at 90° to the primary beam and in the storage ring plane.
An important aspect of XRF analysis is signal to background ratio (S/B). While in the case of continuous (white) spectrum of radiation this value is not the best, it turns out to be optimum with the use of monochromatic excitation. The excitation energy should be slightly higher than the absorption edge to avoid overlapping of the fluorescent signal with the elastically and inelastically scattered radiation. The value closely related to S/B ratio is the minimum detection limit (MDL) formulated as

$$MDL = 3\sigma(I_B)C_F/I_F \tag{3.1}$$

where I_B, I_F are the background and fluorescence signal intensities respectively, C_F is the concentration of the measured sample and $\sigma(I_B)$ is the uncertainty of the I_B below the peak of interest. The value of MDL strongly depends on the experimental conditions and on the sample matrix and for the synchrotron monochromatic radiation it is situated at the sub-ppm level [17].

3.2 X-ray microbeam layout

X-rays are transported from the storage ring to the sample by a beam line. The beam line consists of optical components, a pumping system and shielding with a safety control system. In order to seperate the ultrahigh vacuum of the ring from the low vacuum of the beam line (or the experimental equipment) the hard X-ray beam is usually equipped with Be windows. This is not the case for soft X-ray beam lines which are coupled directly to the ring, to avoid the attenuation. The choice of optical elements depends on the spectrum of radiation.
The simplest way of using continuous radiation for certain experiments is irradiation without specific X-ray focusing optics. It is possible due to the fact that photon flux of such continuum excitation is high and the angular divergence of the beam is small. In this case use of slits is effective enough to achieve a small beam of a few micrometers [20]. To reduce the low energy of the XRF spectrum absorbers as well as transmission-type mirrors [21] have been used.

For the use of monochromatic XRF excitation the beam line layout is more complex, as focusing elements and a monochromator are needed. Usually S/B ratio is higher than in the case of continuous radiation and also the excitation of a specific element is easier. To monochromatize the beam a double crystal monochromator or a synthetic multilayer monochromator are used. Double crystal monochromators are based on germanium, quartz or InSb crystals for the low energy range and almost exclusively on silicon for hard X-rays. They are made of a pair of crystals comprising mechanical systems to assure the constant exit beam height, which is very important during the fluorescence (long) scan. To reduce crystal deformation caused by the heat, which is the case for high brightness synchrotron sources, different cooling devices and/or special geometries were employed ([22], [23], [24]). Synthetic multilayers are made of two different materials (W/C, W/Si, Mo/Si) of which thin layers are deposited under vacuum conditions. The photon flux obtained by the use of a multilayer monochromator is higher by up to two orders of magnitude than the one obtained by a crystal monochromator. This rule applies also to the spectral background.
Most of the XRF experiments are carried out in the air however it would be much more efficient if a special sample chamber was placed in the experimental hutch. This is due to the fact that radiation scattered by air would be suppressed and the attenuation of fluorescent X-rays would be avoided. The sample is placed in the focal plane and mounted on a sample stage to be translated across the beam by stepping or piezoelectric motors. The translation axes are in the x (horizontal) and y (vertical) directions. This is in contrast to an electron or ion beam device, where the beam is translated, not the sample. The sample stage can also be rotated for the purpose of (fluorescence) tomography or diffraction experiments.

3.3 Detection and processing of the X-ray fluorescence signal

To detect the fluorescence signal energy dispersive detectors are used. They can be placed at different angles with respect to the beam (depending on the beam line layout) but ideally at 90^o to fully utilize the advantage of linear polarization. This energy-dispersive detectors record at one time the spectra of all elements in the specimen.

This can cause difficulties to measure trace elements due to the strong signal from major elements. Another disadvantage of conventional energy dispersive detectors is the limited count rate capability. The limit in number of counts is restricted by the need of reasonable energy resolution to be maintained. However a way to overcome this problem would be to use an array of detector elements. The data is collected faster than in the case of just one detector.

It is useful to perform online analysis during the acquisition time. It helps to react immediately on any problems that may appear during the scan and thus prevents from recording the wrong data. Thanks to this, beam time is used efficiently. Once the data is collected, basic operations to perform on it is the spectrum evaluation (also called deconvolution) and quantitative calibration. Spectrum evaluation is made by non-linear least-squares fitting of a mathematical model to the spectral data in order to deal with background and resolve peak overlaps. As a result one gets a list of elemental content. The established strategy is based on minimizing the weighted difference χ^2 between the experimental data y_i and a theoretical fitting function y_{fit}:

$$\chi^2 = \frac{1}{n-m} \sum_i \frac{[y_i - y_{fit}(i)]^2}{y_i} \tag{3.2}$$

where y_i is the content of channel i, y_{fit} is the calculated value of fitting function in this channel, n is the number of channels and m is the number of parameters in the fitting function. As the background in XRF spectrum is the result of many processes, its evaluation is not straightforward. However there are some established strategies how to deal with it. It can be estimated *a priori* and thus subtracted from the data before fitting or it can be calculated with the use of suitable function, such as polynomial or their combination (see for example [25]).

Quantitative calibration requires calculation of the elemental concentrations, which can be done by comparison with certified standards, irradiated in the same conditions as investigated sample or by use of other techniques (see section 6.2.6).

Résumé du Chapitre 3 en Français

Ce chapitre propose une brève introduction aux principes d'imagerie élémentaire par fluorescence X utilisant le rayonnement synchrotron. Le système expèrimental qui permet l'analyse sur la ligne de nanoimagerie X ID22NI est décrit ainsi que le système de détection et les éléments de traitement des spectres de fluorescence X.

Chapter 4

X-ray phase contrast imaging

4.1 Principles

When X-rays pass through an object, two scenarios are considered, according to the refractive index n [26]

$$n = 1 - \delta + i\beta \tag{4.1}$$

The x-rays can be attenuated (Fig.4.1), which effect is determined by the imaginary part of the refractive index, β. Image contrast is in this case entirely due to attenuation differences (emphasis is put on the corpuscular nature of photons) and the amplitude of the radiation changes. β is related to the linear attenuation coefficient μ by:

$$\mu = \frac{4\pi\beta}{\lambda} \tag{4.2}$$

The X-rays can also be retarded in the object. This phenomenon is used in phase contrast imaging, where the effects due to the decrement of the real part of the refractive index, δ, are exploited. A difference in the δ value between an object and the background results in a phase shift between the wave transmitted through and outside the object. Due to this phase shift an interference pattern appears upon propagation (Fig.4.2), propagation based phase contrast is one of the possibility. Emphasis is thus put on the wave nature of X-rays. According to the projection approximation the phase shift is described as follows

$$\Delta\Phi(x, y) = -\frac{2\pi}{\lambda} \int \delta(x, y, z) dz \tag{4.3}$$

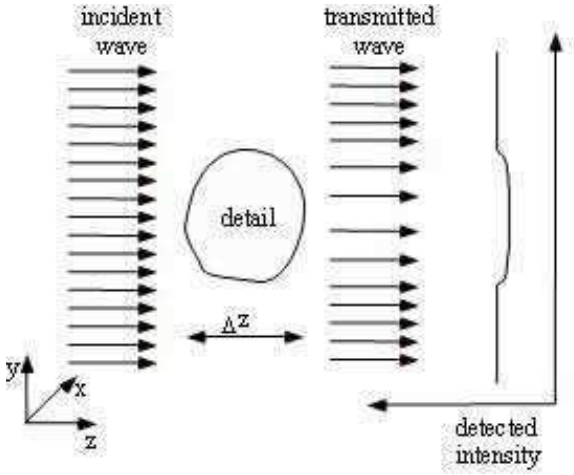

Figure 4.1: Schematic picture of conventional radiology based on absorption effects

For the case of a scatterer composed of a single material of projected thickness $T(x, y)$ along the z direction, the equation 4.3 simplifies to

$$\Delta\Phi(x, y) = -\frac{2\pi}{\lambda}\delta T(x, y) \tag{4.4}$$

If δ is known for this kind of material, the phase shift provides immediately the

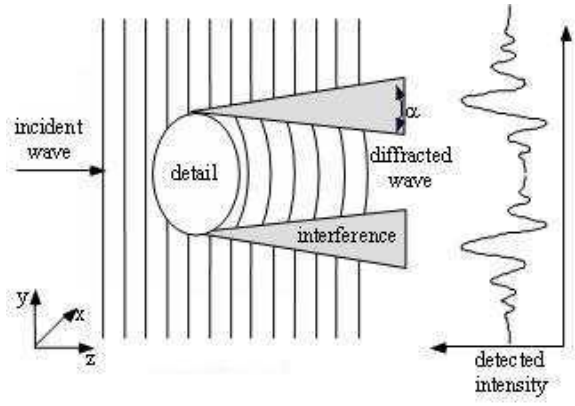

Figure 4.2: Schematic picture of propagation based phase contrast imaging. The range of α is between 10 and 100 μrad.

projected thickness. In principle regarding the biological material (meaning material built of light elements: C, H, O, etc) and far from absorption edges (hard energy

regime) it can be approximated as follows:

$$\delta \approx 1.36 \times 10^{-6} \rho[g/cm^3] \lambda^2[\text{Å}] \tag{4.5}$$

Then the projected phase from 4.4 will be proportional to the density of the object ρ and the wavelenght λ. Later on in order to simplify the equations we will be treating the value of $1.36 \times 10^{-6} \lambda^2 (in\ [\text{Å}]) \frac{2\pi}{\lambda\ (in\ m)}$ as a well known constant α.
Phase contrast imaging is perfectly suitable for non- or weakly absorbing samples, such as soft biological tisues iluminated by hard X-rays. If they are sufficiently thin, only the phase of the waves transmitted through them will change. Thus the intensity of the exit-surface wave-function would not carry any information about the structure of the sample, oppositely to the phase of the exit wave-function. In this work we concentrate on propagation based phase contrast imaging.

4.2 Phase retrieval

One can consider phase contrast images as encrypted images of the phase distribution $\Phi(x, y)$. The problem of phase retrieval is nothing more than the problem of decoding such images to retrieve the phase $\Phi(x, y)$ of the incident radiation, often called as 'inverse problem'. In the following sub-sections some different approaches to the inverse problem are outlined: the Gerchberg-Saxton algorithm [27],the transport-of-intensity equation (TIE) [28], [29] and the transfer function approach [29]. The last one is used in this work for phase contrast imaging of biological samples.

4.2.1 The Gerchberg-Saxton algorithm

The Gerchberg-Saxton algorithm is an iterative algorithm for retrieving the phase of a wave-field assuming the modulus of the wave-field and the modulus of its Fourier transform are known. It can formally be expressed as

$$\psi(x, y) = \lim_{N \to \infty} (P_1 F^{-1} P_2 F)^N |\psi(x, y)|\ \exp[i\Phi_{initial}(x, y)] \tag{4.6}$$

This is the case for two-dimensional wave fields, where P_1 is the projection operator replacing the modulus of the function on which it acts with the known quantitiy $|\psi(x, y)|$,

P_2 acts to replace the modulus of the function on which it acts with the known quantity $|F\psi(x,y)|$ (as shown in Eq. 4.6), N is a number of iterations, $\Phi_{initial}(x,y)$ is the initial guess for the unknown phase. The explanation of an equation 4.6 is as follows:

- initial crude estimate of a known modulus and random or constant phase $|\psi(x,y)|\ \exp[i\Phi_{initial}(x,y)]$ for the desired $\psi(x,y)$ is chosen
- Fourier transform operator F is applied to a chosen estimation
- the result of the Fourier transform is improved by replacing its modulus by the known value $|F\psi(x,y)|$
- the inverse Fourier transform operator F^{-1} is applied
- the operator P_1 replaces the modulus of the previous estimation by the known modulus $|\psi(x,y)|$
- the algorithm is stopped after a number of iterations according to a convergence criterium

This type of algorithm can in principle be extended to the Fresnel diffraction case. It would simply require to replace the Fourier transform by the Fresnel transform. However in practice convergence is poor without a reasonable initial estimate of the phase $\Phi_{initial}$.
Therefore in real cases, linear methods are used for phase retrieval in propagation based phase contrast imaging. An extensive overview and comparison of the linear methods can be found in [30]. In short, a linearization assuming small propagation distances leads to the TIE, assuming a weak or slowly varying object leads to the transfer function approach.

4.2.2 The transport-of-intensity equation (TIE)

The transport of intensity equation describes the flow of intensity along the optical axis as light waves propagate:

$$\frac{\partial I(x,y)}{\partial z} = -\frac{\lambda}{2\pi}\nabla_\perp \cdot (I(x,y)\nabla_\perp \Phi(x,y)) \tag{4.7}$$

where $\nabla_\perp \equiv \partial/\partial x + \partial/\partial y$.
By using few images phase map can be readily retrieved. The retrieval procedure does not require an iterative calculation and it is performed very rapidly with the use of the Fourier transform. In addition, by using many images, one gets better phase contrast across all spatial frequencies and is able to reduce the effects of noise. However, it must be noted that sensitivity depends on the spatial frequency components and difficulties are encountered when phase information is retrieved to be of the same quality for all frequency components. Since the retrieved phase is influenced by conditions in which the focal series were taken, it is important to select the appropriate conditions and parameters used in this process. In the case of pure phase object, the intensity I(x,y) is constant and one measures the Laplacian of the phase. In this case a single distance is sufficient to retrieve the phase, but the process is sensitive to noise and provides a limited spatial resolution.

4.2.3 Transfer function approach

The objects imaged by X-rays can be described following:

$$T(x,y) = e^{-B(x,y)} e^{i\Phi(x,y)} \ , \tag{4.8}$$

where $\Phi(x,y)$ was already described in 4.1 and B(x,y) stands for the absorption part and is given by:

$$B(x,y) = \frac{2\pi}{\lambda} \int \beta(x,y,z) dz \ , \tag{4.9}$$

In a case of biological objects we can neglect the absorption (B(x,y) $\simeq$ 0). We apply the condition of slowly varying phase [31]. The intensity spectrum is described as follows:

$$\widetilde{I}(\mathbf{f}) = \delta_D(\mathbf{f}) + 2\sin(\pi\lambda D|\mathbf{f}|^2)\widetilde{\Phi}(\mathbf{f}) \tag{4.10}$$

where the 2D Dirac function δ_D represents for $\mathbf{f}$=(f_x,f_y)=0 the mean intensity. The sinus term is called the phase contrast factor or phase contrast transfer function (see Fig. 4.3). The solid line in Fig. 4.3 shows that this term is equal to zero for all distances $\lambda D|\mathbf{f}|^2$ = p, p $\in$ Z where the image shows no contrast.
In the case of weak object the intensity spectrum is linearized with respect to $\widetilde{\Phi}$ and $\widetilde{B}$ [32]:

$$\widetilde{I}(\mathbf{f}) = \delta(\mathbf{f}) + 2\sin(\pi\lambda D|\mathbf{f}|^2)\widetilde{\Phi}(\mathbf{f}) - 2\cos(\pi\lambda D|\mathbf{f}|^2)\widetilde{B}(\mathbf{f}) \tag{4.11}$$

The cosinus term appears as multiplicative factor for the amplitude spectrum of the object, therefore it is referred to as the amplitude contrast factor. The dashed line in Fig. 4.3 shows its shape as a function of $\frac{|\mathbf{f}|}{\sqrt{\lambda D}}$. In the case of biological material (slowly

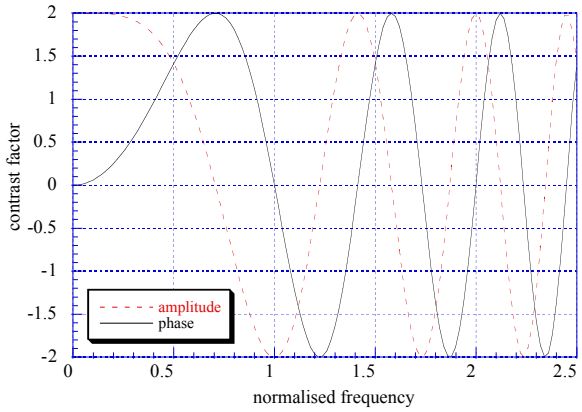

Figure 4.3: The phase and amplitude contrast factors as a function of the normalised spatial frequency $\frac{|\mathbf{f}|}{\sqrt{\lambda D}}$

varying phase and no attenuation contrast) the contribution of the attenuation part is negligible; therefore the calculations used in phase retrieval algorithm [33] are based on 4.10. As an example Fig.4.4 shows the same comparison as in Fig.4.3 but together with the TIE approach. It can be seen that the transfer function approach and TIE

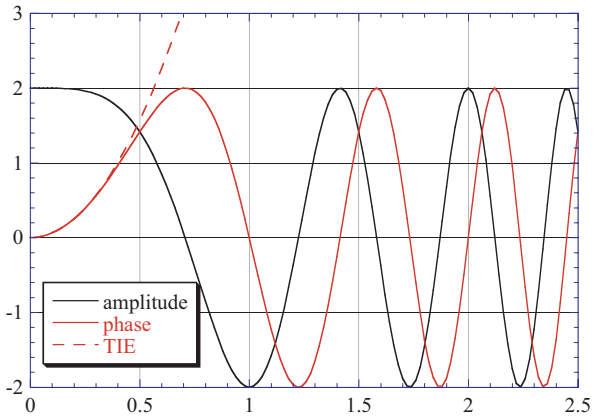

Figure 4.4: The phase and amplitude contrast factors as a function of the normalised spatial frequency $\frac{|\mathbf{f}|}{\sqrt{\lambda D}}$ together with a TIE approach

are identical for low spatial frequencies, but TIE does not include the zero-crossings

and inversions of contrast occuring at at higher spatial frequencies. This explains why the TIE solution "looses" the fine details of the object.
The inverse problem in phase contrast imaging consists of finding the phase and the amplitude of the object from the available information - the measured intensity. We introduce D_m instead of D, which means we consider multiple defocus distances assuming that we record N images at distances D_m, m= 1,..., N. The use of multiple distances solves the "blindness" to some spatial frequencies (zero-crossings) and allows to recover the phase information with equal quality in a much larger frequency range. For the biological samples the contribution from the absorption part is neglected. Then the inverse problem consists of finding only the phase. Keeping in mind equation 4.10 and assuming different distances, the formula for the phase calculation is obtained by minimizing the difference between the observed and calculated intensity distributions in a least square sense:

$$\widetilde{\Phi}(\mathbf{f}) = \frac{1}{N} \sum W_m(\mathbf{f}) \widetilde{I}_m^{exp}(\mathbf{f}) \tag{4.12}$$

where W_m is the filter function [34]

$$W_m = \frac{\sin(\pi \lambda D_m |\mathbf{f}|^2)}{\frac{1}{N} \sum 2 \sin^2(\pi \lambda D_m |\mathbf{f}|^2} \tag{4.13}$$

The filter functions weight each experimental image $\widetilde{I}_m^{exp}(\mathbf{f})$ correctly according to the phase contrast factor.

Résumé du Chapitre 4 en Français

Ce chapitre apporte une introduction sur l'imagerie X par contraste de phase. Les principes de la techniques sont rappelés ainsi que les équations à la base des algorithmes que j'ai utilisée au cours de ce travail de thèse et qui permettent la reconstruction de phase d'un échantillon à partir de radiographies X de celui-ci collectées à différentes distances hors du plan de focalisation.

Chapter 5

X-ray imaging of the biological material

This chapter will blaze a trail to a fully quantitative combination of two X-ray imaging techniques: X-ray fluorescence and phase contrast imaging. Once combined they yield absolute metal projected concentrations or mass fractions at the sub-cellular level. But before that, all the measures have to be taken into account and validated properly in order to achieve the final goal. To support the validation process some other techniques (such as Atomic Force Microscopy) are introduced. The possibilities of the different techniques are explored on a number of biological samples from bacteria to human cells.
Brief introduction to the idea of combining two techniques, based on standard, non biological samples is given as well as the introduction to the experimental setup.

5.1 Combination of X-ray fluorescence and phase contrast techniques

The detailed description of the ID22 beamline is given in Appendix A [71]. For the purpose of this scientific project two techniques were used: X-ray fluorescence imaging and magnified phase contrast imaging although at ID22 other techniques can be used

as well.
The two techniques are not performed simultaneously, but the setup is compatible and it is sufficient to move the sample in or out of the focal plane to switch between two models. While scanning a sample in the fluorescence mode, nothing more than fluorescence spectra will be registered. While performing phase contrast imaging nothing more than just phase contrast data will be stored. This approach has of course advantages and disadvantages. Since the data is not collected simultaneously, it requires alignment. Alignment is performed with the use of cross correlation techniques available in the ImageJ software. On the other hand recording phase contrast images before and after the fluorescence scan allows to monitor changes taking place during the fluorescence scan (irradiation). Besides the magnified phase contrast imaging provides bigger field of view than in the case of fluorescence scanning; it is also acquired much faster. Thus the phase imaging can be used to create an overview image and the slow fluorescence imaging is directly applied to a relevant sub-region. X-ray fluorescence analysis is performed at the nano-imaging station ID22NI (see also Fig.6.1), using the intrinsic monochromaticity of the undulators of about $\delta\lambda/\lambda \simeq 0.01$. The experimental station is located at a distance of 63 m from the undulator source and at 37 m from the high power slits used as secondary source in the horizontal direction (25 μm slit opening). The synchrotron radiation is focused by an X-ray optical device consisting of two elliptically shaped mirrors acting in two orthogonal planes using the so-called Kirkpatrick-Baez geometry [35]. The mirrors are coated with a graded multi-layer. No other monochromator is used in the setup, resulting in a very high and unique X-ray flux (up to 10^{12} photons/s) at energies between 17 and 29 keV. The samples are positioned in the focal plane of the KB system and translated by piezo-stages in the directions perpendicular to the beam. The X-ray fluorescence spectra are collected by a silicon drift energy dispersive detector positioned in the horizontal plane at 75° of the incoming X-ray beam (normal incidence).
Phase contrast analysis is performed as well at the nano-imaging station ID22NI. For the purpose of combined analysis phase contrast imaging was always made before the fluorescence scan, sometimes also after - in order to verify the structural changes of an object, if any. The sample is moved out of the focus (Fig.5.1) and iluminated by the divergent beam. Magnified Fresnel patterns are collected at several distances by a Frelon CCD based detector. At each distance, an image of the object is recorded. These are so called raw images (Fig.5.2), they are not corrected for the background

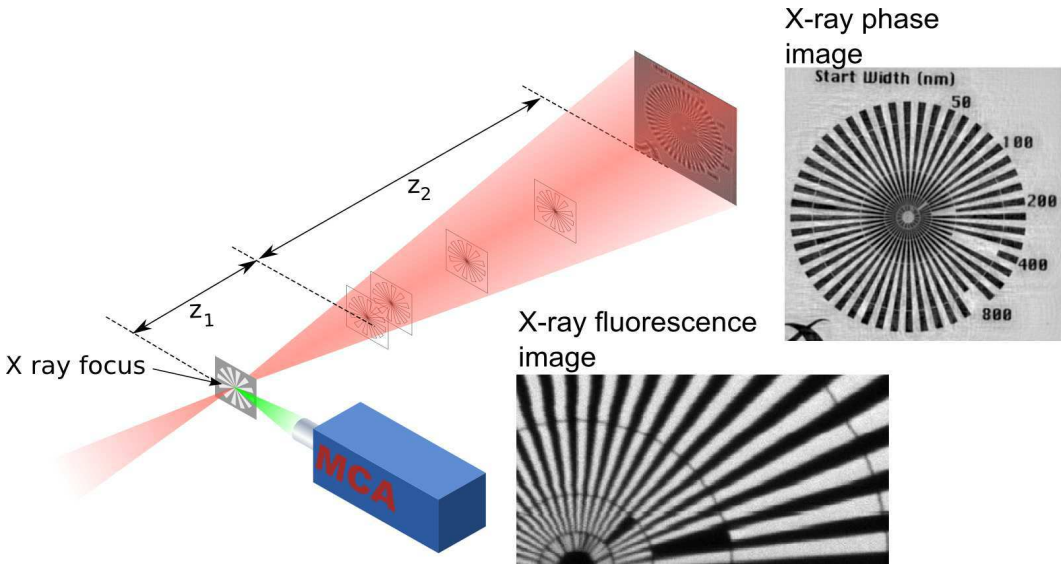

Figure 5.1: Schematic view of the combined techniques. With the sample in the focus, the X-ray fluorescence spectra are collected and used to build elemental maps. But the sample can also be moved out of the focus and put at several distances downstream of the focus in the divergent beam. At each distance a magnified Fresnel diffraction pattern is collected. They will be used all together in the phase retrieval procedure. Using the phase retrieval algorithm, a quantitative phase contrast map of the sample is recovered.

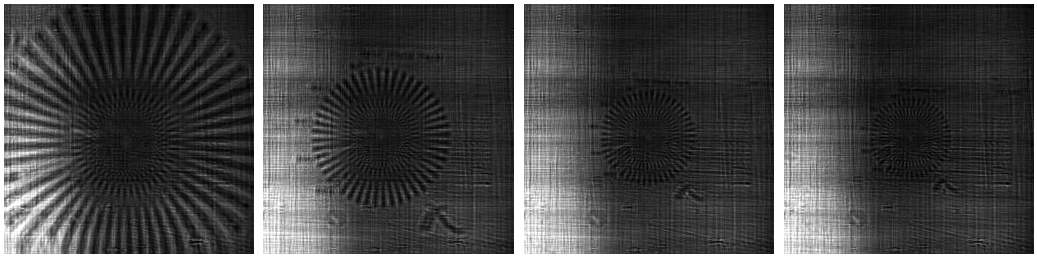

Figure 5.2: Raw images of a Siemens star test pattern (Xradia Inc.) at 4 different distances (29mm, 30mm, 34mm, 44mm). Every image has a different magnification and is not corrected for optical distortions. The raw images are used to recover a phase map (see Fig. 5.1).

distortions and are with different magnification values. They will be used after all in a phase retrieval procedure in order to build the phase map. As schematically shown on the Fig. 5.1 the phase map provides always a bigger field of view than the fluorescence map.
Phase retrieval procedure theoretically described in 4.2.3 and adapted for the ID22NI purpose uses the equivalence between spherical wave illumination and plane wave illumination. As mentioned already the raw images recorded at each distance, have different magnification values (M), depending on the distances z_1 and z_2 (see Fig. 5.1)

$$M = \frac{z_1 + z_2}{z_1} \tag{5.1}$$

for which equivalent defocus distances are introduced:

$$D = \frac{z_1 z_2}{z_1 + z_2} \tag{5.2}$$

In the case of our experiments always four distances are chosen and thus the sum from equation 4.12 runs up to $m = 4$.
The flat-field procedure to correct for background and corrections for optical distortions are then applied. Finally a phase map as the one shown on Fig. 5.1 is obtained using Eq.4.12. This procedure is sufficient - no need for iterative methods, as (biological) samples typically fulfill the assumptions.

5.2 Bacteria Escherichia coli

Escherichia coli (E. coli) are gram-negative bacteria that can survive in an environment with or without air (facultative anaerobes) and, depending on the environment, may or may not produce thin hair-like structures (flagella or pili) that allow the bacteria to move and to attach to human cells. They are small organisms of typical size 0.5 x 2 μm with relatively simple internal structural organisation. These bacteria commonly live in the intestines of people and animals worldwide. There are many strains (over 700 serotypes) of E. coli. Most of the E. coli are normal inhabitants of the small intestine and colon and do not cause disease in the intestines (non-pathogenic). Nevertheless, these non-pathogenic E. coli can cause disease if they spread outside of the intestines, for example, into the urinary tract (where they cause bladder or kidney infections), or into the blood stream (sepsis). Other E. coli strains (enterovirulent E. coli strains or EEC) cause "poisoning" or diarrhea even though they usually remain within the intestine by producing toxins or intestinal inflammation.
E. coli were first isolated by T. Escherich in 1885 and were named after him. The over 700 serotypes are identified by small antigenic changes in their surface "O" antigens (lipopolysaccharides or molecules on the bacterial surface of gram-negative bacteria), for example E. coli 0157 or E. coli 055. These serotypes are identified by immunological tests. E. coli strains are further distinguished by "H" protein antigens (different types of flagella that make the bacteria motile). Consequently, a particular E. coli strain can be identified as H, followed by a number, and this identifier is added to the "O" name; for example, E. coli 0157:H7. Although this name designation seems complicated, researchers and clinicians use these antigenic identifiers to track specific E. coli strains that cause outbreaks of disease. E. coli is the most widely studied prokaryotic model organism and an important species in the fields of biotechnology and microbiology. It is also one of the first organisms to have its genome sequenced [36]. In the present work, E. Coli can mimic typical intracellular organelle such as mitochondria and allow to test the capabilities of our X-ray phase nanoimaging approach.
In further part of this section results obtained by different imaging techniques will be discussed.

5.2.1 X-ray fluorescence of E. coli

The bacteria E. coli was used for imaging in presence or absence of 300 μM of Fe in order to investigate the metal homeostasis. The samples were prepared by the group of scientists from the Institut of Structural Biology in Grenoble.
The bacteria after incubation in 300 μM solution of Fe were rinsed, applied as a sparse monolayer to a 500-nm-thick silicon nitride substrate (Silson, Blisworth, U.K.), and air dried. The size of the substrate was 3 mm x 3 mm.
Bacteria E. coli were imaged with 2 different energies, at the first time with an energy of 17.5 keV and during another set of experiments with an energy of 17 keV. The choice of energies was dependent from the configuration of the beamline but this did not influence the final result of X-ray imaging.
Before mounting samples at the sample holder in the experimental hutch, bacteria strains were investigated carefully under the optical microscope (Fig. 5.3, 5.4) in order to identify it and register position of bacteria of interests. Also for the experiment purpose it was interesting to select single bacterium (if possible). All these checks are required before starting the X-ray experiment. In order to avoid the radiation damages fluorescence scan is performed after acquiring phase contrast data.
Sample containing 300μM of Fe was scanned with a step size of 50 nm and a dwell time of 400 ms while the control one was acquired with a dwell time of 300 ms. Fluorescence spectra from the sum of all the pixels (see example on Fig. 5.5) were collected via a silicon drift energy dispersive detector and fitted with the PyMCA program (see section 6.2.6). Some results of batch fitting are presented on the Fig. 5.6. As one would expect the iron content in incubated sample is 100 times higher than in the control one. The distribution in the incubated sample seems inhomogeneous with areas with much higher iron content. However in order to show any systematic tendency, a larger number of bacteria would have to be investigated.

5.2.2 Phase contrast of E. coli

In order to perform phase contrast imaging the sample was moved out of the focus and put at four distances downstream of the focus, where magnified Fresnel diffraction patterns are collected by a CCD based detector. For every experiment (not only the

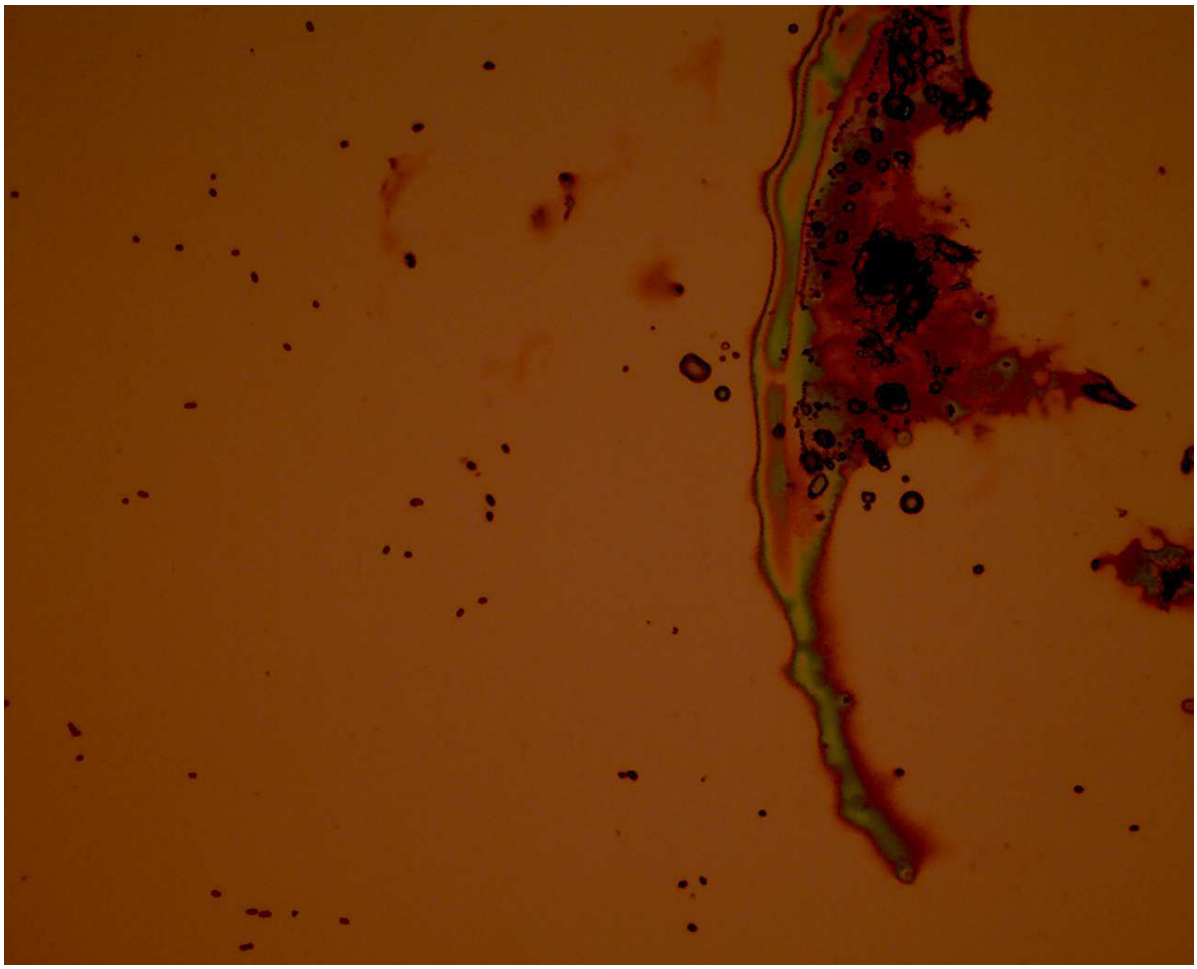

Figure 5.3: View from optical microscope on the bacteria E. coli sample. Visible bunch of bacteria as well as single ones.

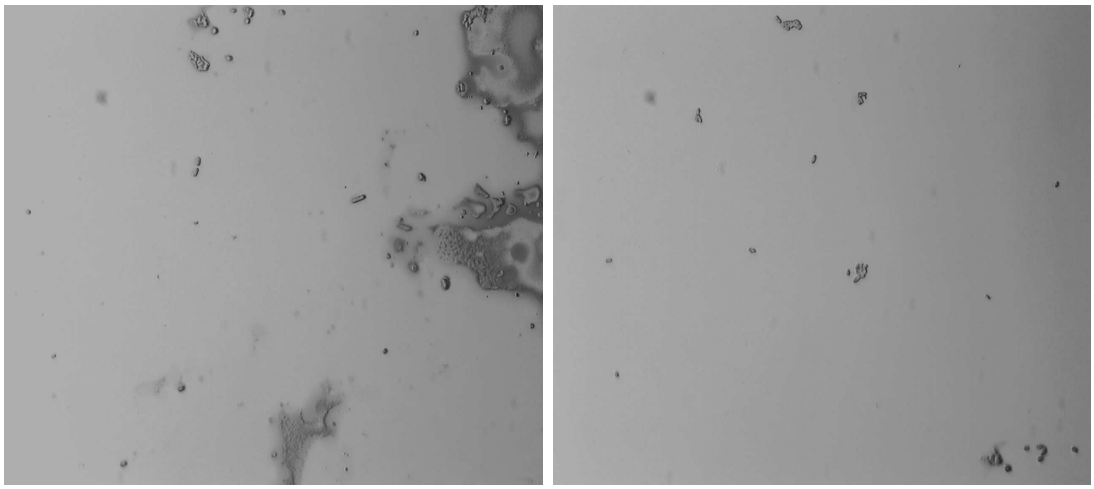

Figure 5.4: View from optical microscope on the bacteria E. coli sample with different magnifications. Visible bunch of bacteria as well as single ones.

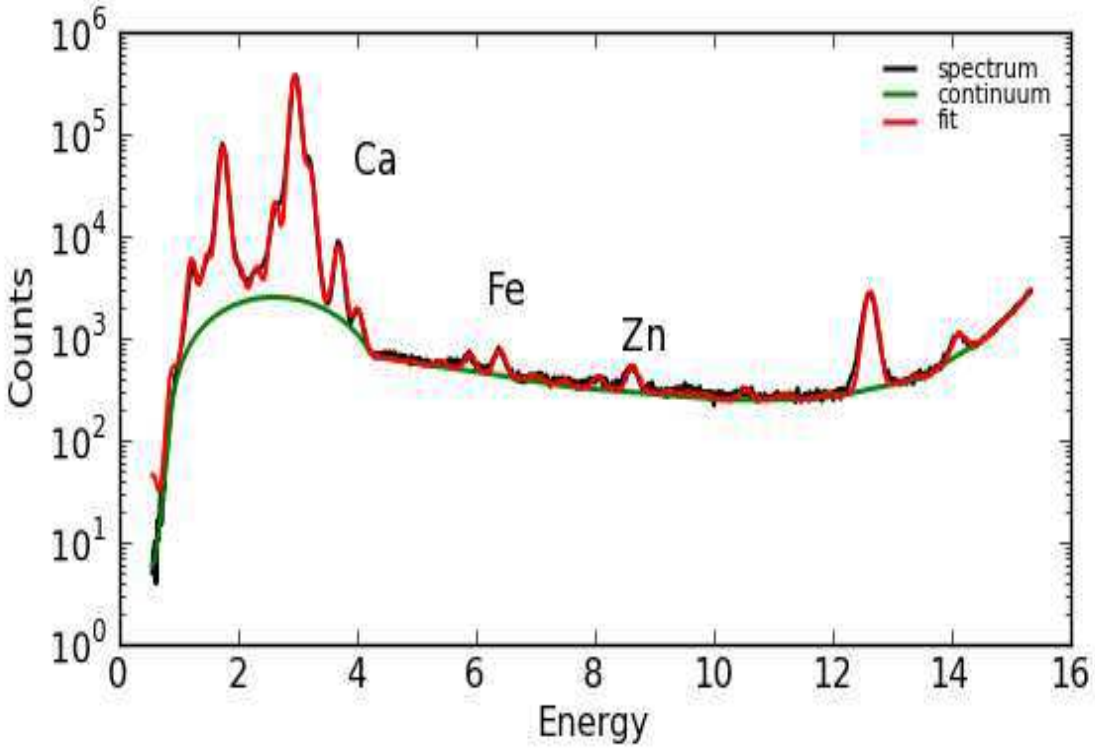

Figure 5.5: X-ray fluorescence spectrum sum of the bacteria control sample with some of the elements. Energy scale is in keV.

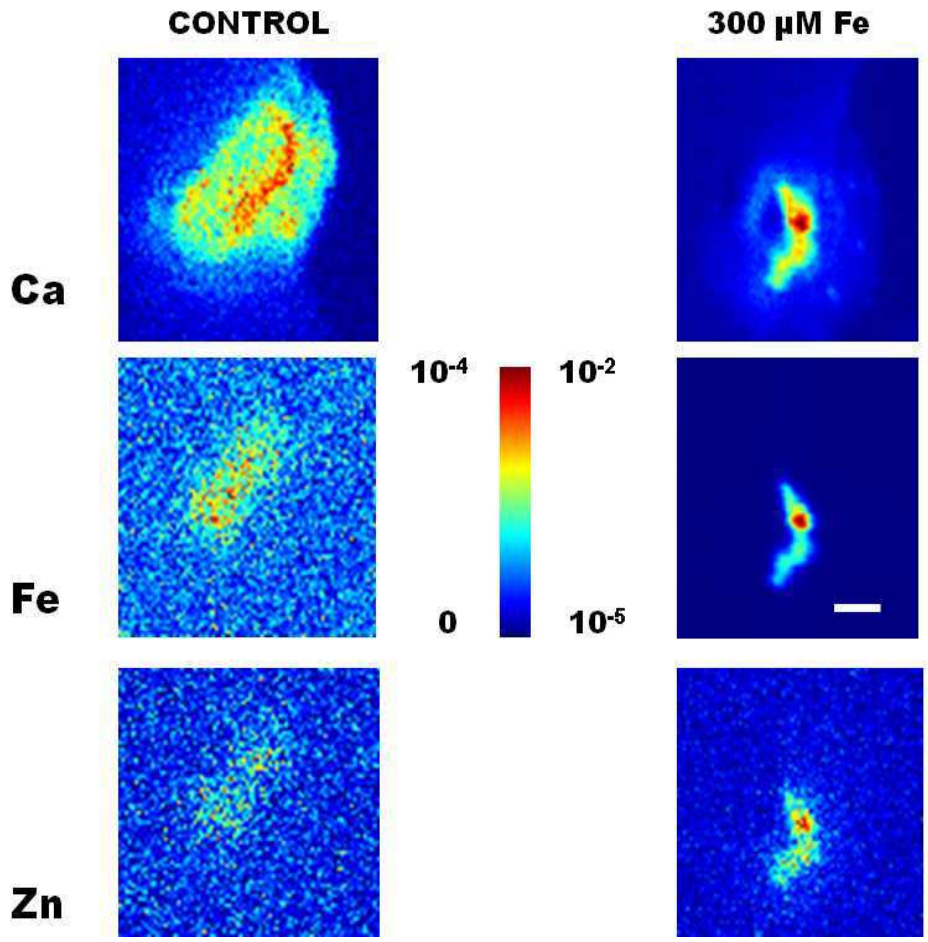

Figure 5.6: X-ray fluorescence maps (Ca, Fe, Zn from up) of bacteria E. coli samples: control (left column) and incubated with 300μM of Fe. Scanning size was 80x81 pixels, scale bar 1 μm. Color scale bar indicates minimum and maximum content (assuming ρ=1g/cm^3 and thickness T= 500nm which were used in PyMCA routine) of Fe in control and in incubated sample. The colors are scaled to the maximum of each map.

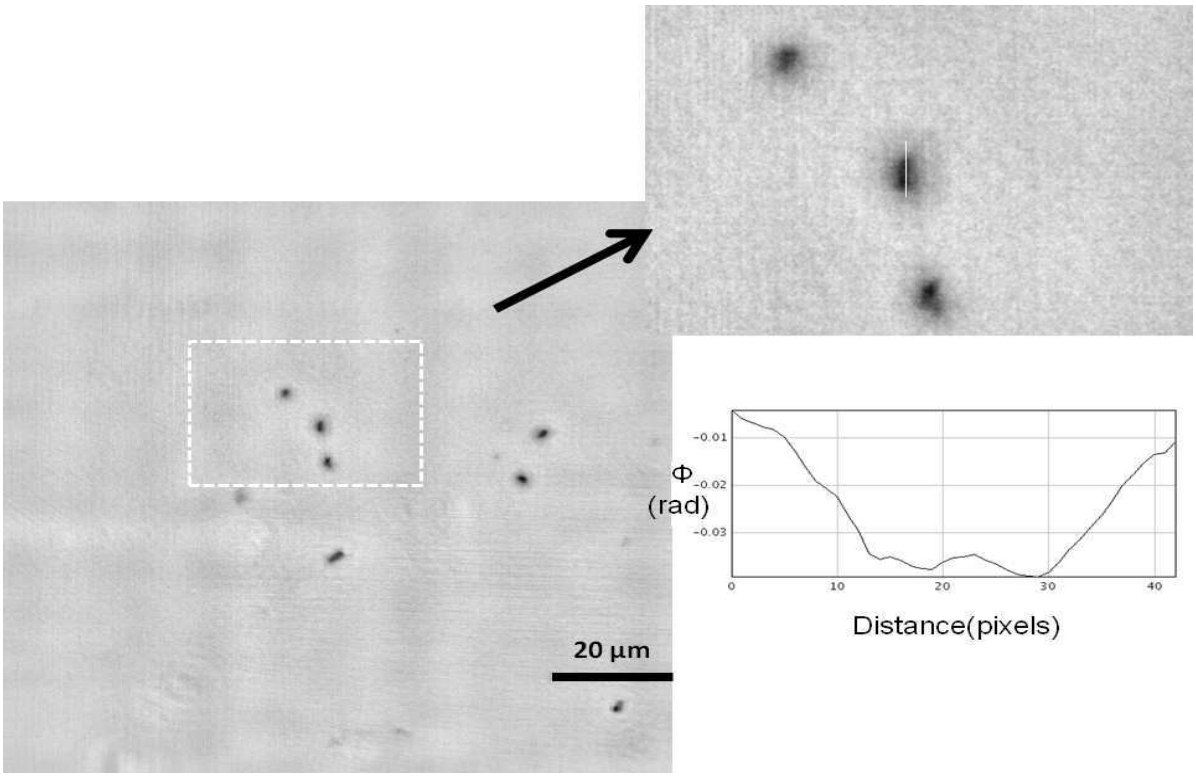

Figure 5.7: Phase image of bacteria E.coli incubated with iron (left) and a zoom on the selected area (right) with a profile (bottom) along the white line. The calculation of a thickness based on a profile gives a result of about 500nm.

one with bacteria strains) first phase contrast data was collected and after fluorescence scanning was performed. A retrieved phase map of an area with several bacteria incubated with iron (but not the same one as shown on Fig. 5.6) is shown in Fig. 5.7.
As it is described in 4.1 and 6.2.3 the projected phase of an investigated object can be translated into the thickness of the object. The difference between maximum (considered as background) and minimum (the deepest part of the bacterium in certain area) value of the projected phase (regarding the profile from Fig. 5.7) divided by the bacterium density, 1.16g/cm^3 [37] and constant α (see 4.1) gives a value of about 500nm. This result is consistent with the result obtained by Atomic Force Microscopy (see 5.2.3). For the ID22NI nano-imaging station, where experiments were performed, bacteria E.coli represents an interesting object. Due to its significantly small size it can act as an object for studying the beamline limitations. Already in the previous section

it was pointed what kind of step sizes had to be chosen in order to show the bacteria structure. The phase contrast imaging was performed with a large field of view and a pixel size of 75 nm, calculated from the first distance magnification (see 5.1) wrt. the pixel size of the detector (0.96 μm). Even if one could claim there are some structural details of bacterium visible on XRF image, none of them are visible on phase contrast image (Fig.5.7).

5.2.3 Atomic Force Microscopy of E. coli

The atomic force microscope (AFM) system has evolved into a useful tool for direct measurements of micro-structural parameters and unraveling the intermolecular forces at nanoscale level with atomic-resolution characterization. Typically, these micro-cantilever (Fig. 5.8) systems are operated in three open-loop modes; non-contact mode, contact mode, and tapping mode. In order to probe electric, magnetic, and/or atomic forces of a selected sample, the non-contact mode is utilized by moving the cantilever slightly away from the sample surface and oscillating the cantilever at or near its natural resonance frequency. Alternatively, the contact mode acquires sample attributes by monitoring interaction forces while the cantilever tip remains in contact with the target sample. The tapping mode of operation combines qualities of both the contact and non-contact modes by gleaning sample data and oscillating the cantilever tip at or near its natural resonance frequency while allowing the cantilever tip to impact the target sample for a minimal amount of time. The AFM experiments were performed at the Surface Science Laboratory of the ESRF. The measurements were taken with the tapping mode. The same sample (but not the same bacteria) as the one imaged with X-rays was used. It was a bit of a challenge to perform AFM this sample due to the fact that bacteria are very small and that the membrane on which they are deposited is very thin; it could be easily damaged by the tip. Besides the damaging, membrane could also resonate and this fact had to be taken into account.
First the area of interest was selected by viewing the bacteria sample under the optical microscope and then the same area had to be found once the sample was mounted in the AFM machine. The view from AFM microscope is presented on the Fig. 5.9. The group of three bacteria was selected and imaged by the AFM (Fig. 5.10). The scanning size was 2.5 μm with the scan rate 0.7 Hz and 256 lines. To explore the structure of

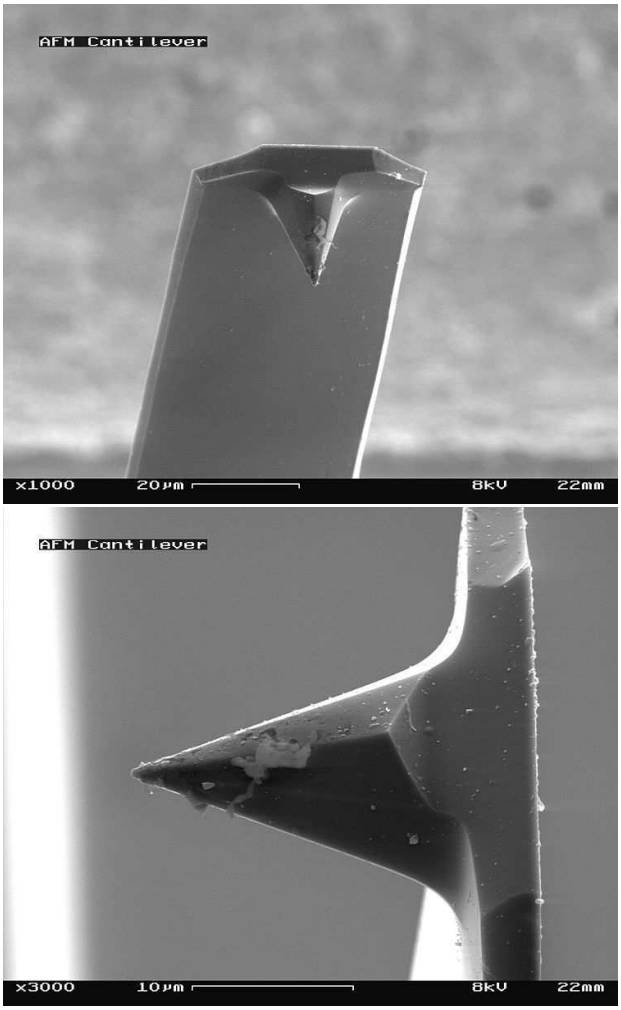

Figure 5.8: Electron micrograph of a used AFM cantilever. Image width around 100 μm (upper) and 30 μm (bottom)

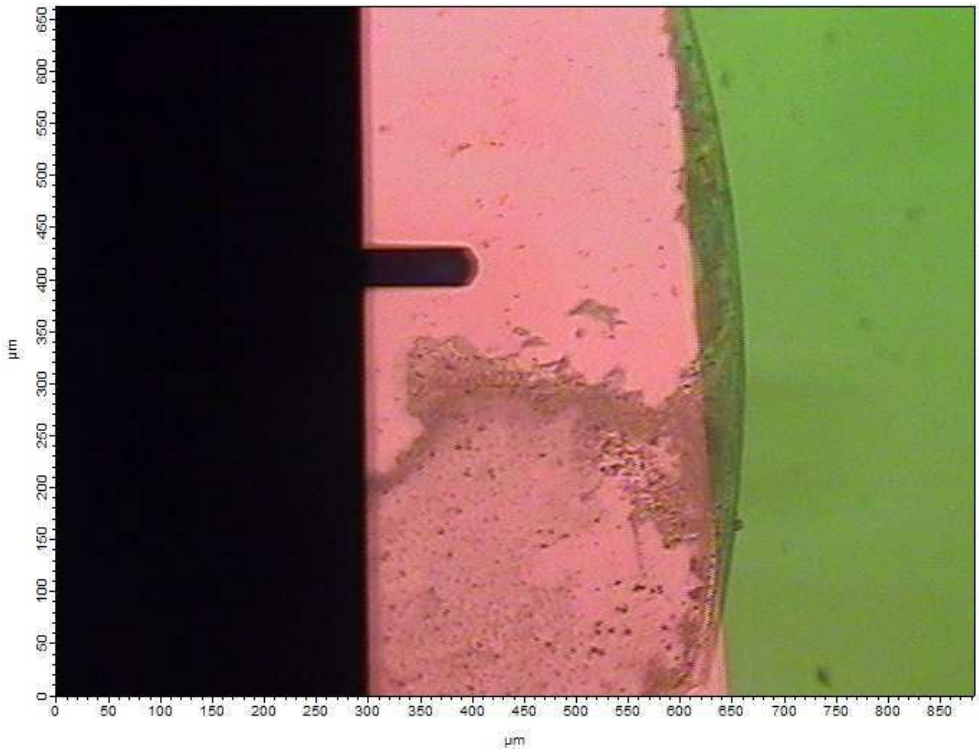

Figure 5.9: View from AFM microscope on the bacteria sample deposited on the silicon nitride membrane (pink color). The frame is visible as well (green color) and the AFM cantilever.

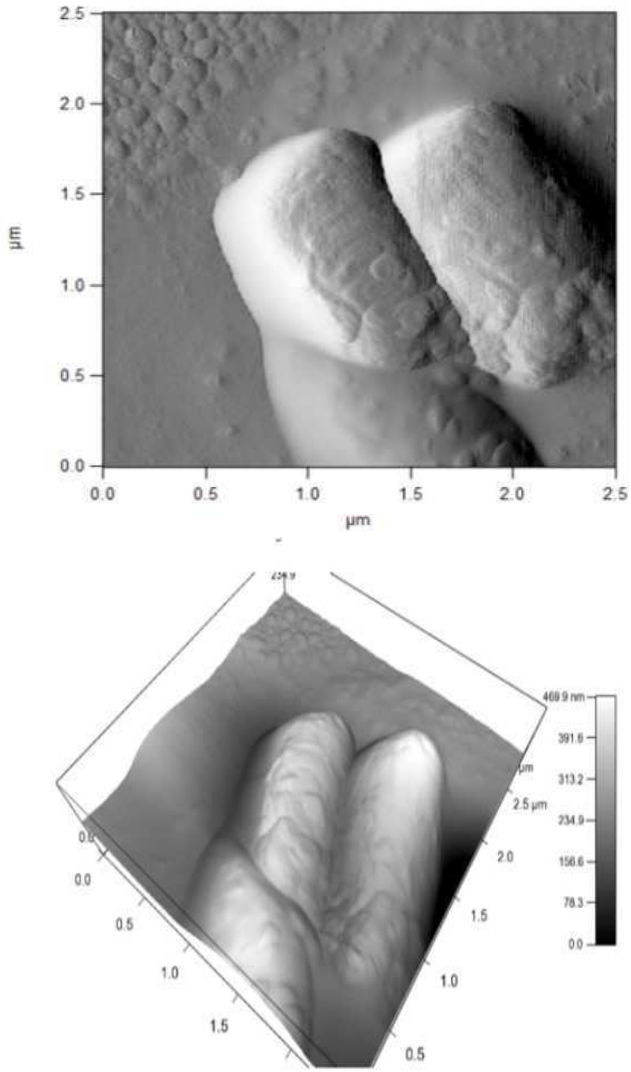

Figure 5.10: AFM picture of a group of three E.coli bacteria (upper) and the same view in 3D (bottom).

the bacteria a cross section profile was made (Fig. 5.11). The measured thickness of

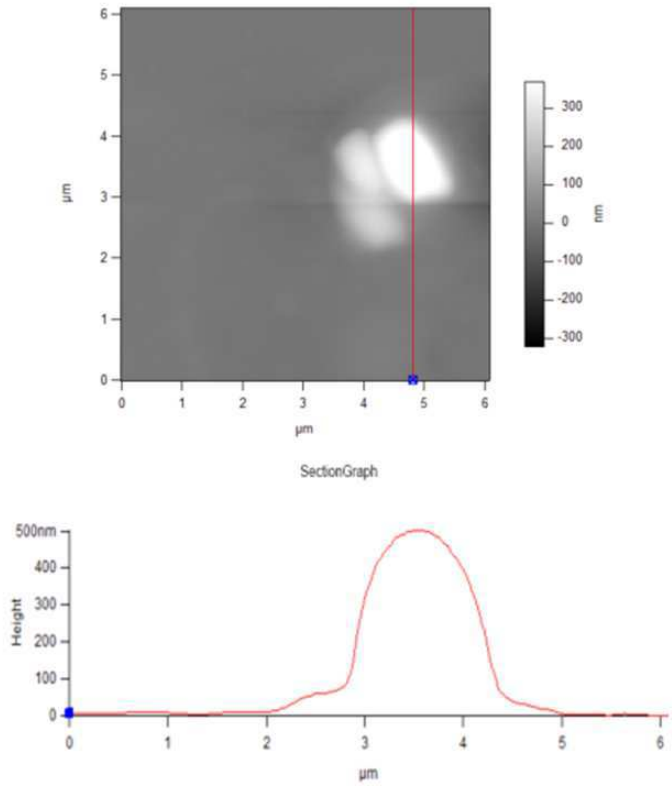

Figure 5.11: AFM view on bacteria E. coli with selected section (upper) and the profile through it (bottom)

a bacterium is about 500nm, similar to the value estimated through a phase imaging. Not to forget is the fact that these were not the same bacteria.

5.3 Human embryonic kidney cell line

Human Embryonic Kidney 293 cells (HEK293 or 293 cells) are a cell line that is very easy to grow and transfect, and have been widely used in molecular cellular biology research. They are also used to produce recombinant proteins and viruses for research and gene therapy. They are easily manipulated in order to produce new cell lines that over-express particular proteins in a stable way (compare to the mother cell line).

Similarly to bacteria strains cells HEK293 were grown on the silicon nitride (Si_3N_4) membrane of 500nm thickness. The cells were cryofixed at -160°C by plunging it into liquid nitrogen chilled isopentane and samples were further lyophilised under vacuum at low temperature (-65°C). Due to sample preparation some cells were also deposited on the frame, much thicker than the membrane. The same experiments (phase contrast imaging, X-ray fluorescence and AFM) were performed. Prior analysis, cells were investigated under an optical microscope and few cells were arbitrary selected (Fig. 5.12, Fig. 5.13).

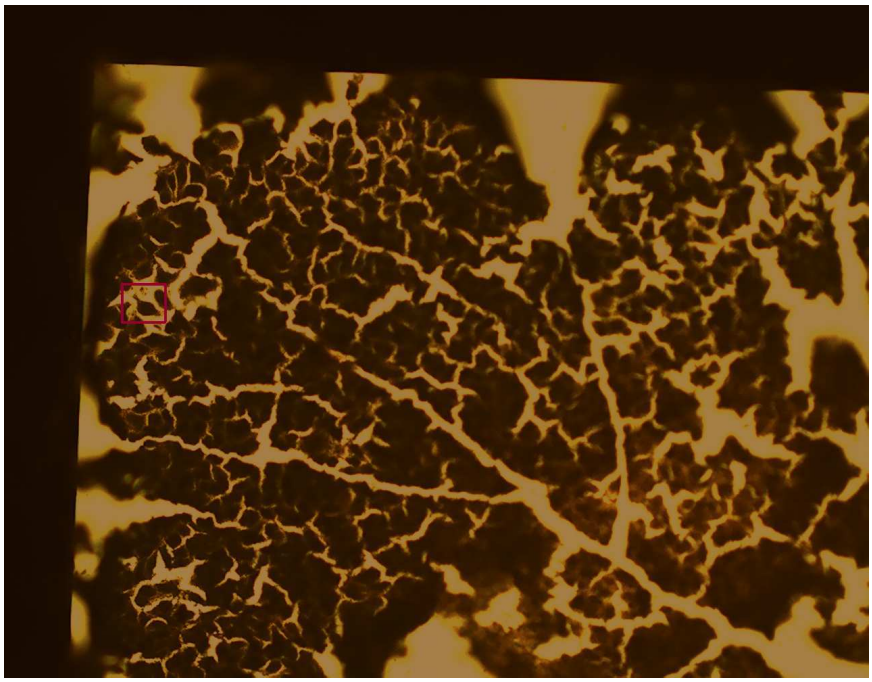

Figure 5.12: Optical view (and thus not directly comparable with X-ray images Fig. 5.15, Fig. 5.16) on the selected (red square) HEK293 cells.

5.3.1 X-ray fluorescence of HEK293 cells

The same experimental setup as for the bacteria E. coli was used for the imaging of the HEK293 cells. The sample was placed in the X-ray focus and scanned with a step size of 100nm and dwell time of 300ms. The fluorescence spectra were fitted (Fig. 5.14) with the PyMCA program. Some results of batch fitting are presented on the Fig.

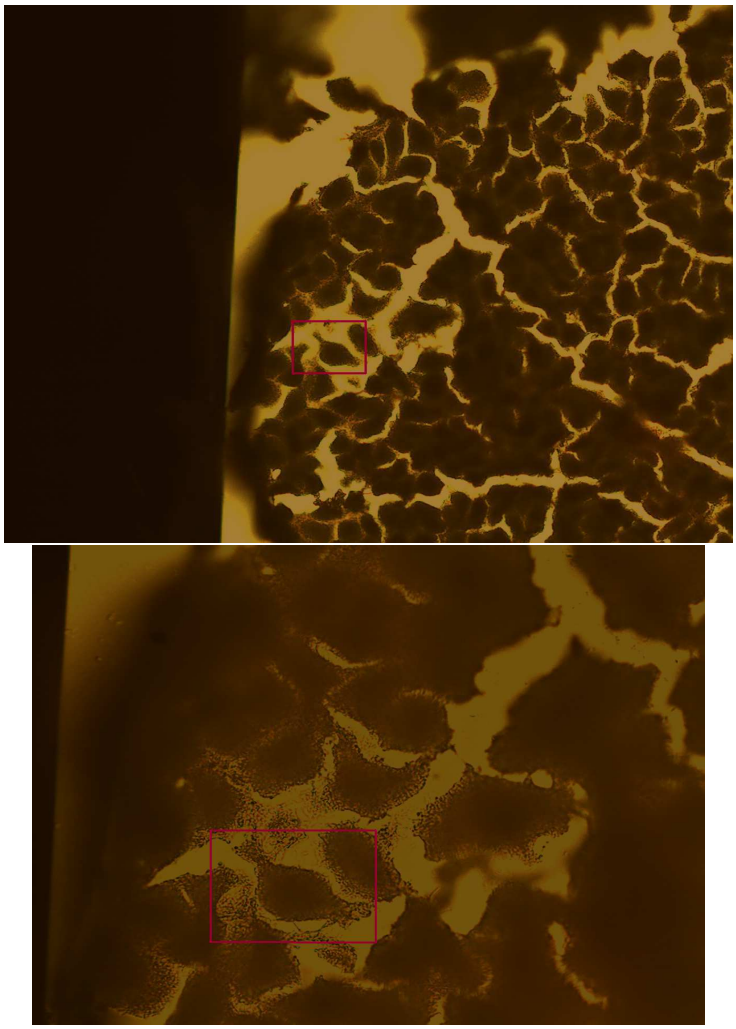

Figure 5.13: Optical view (and thus not directly comparable with X-ray images Fig. 5.15, Fig. 5.16) on the selected (red square) HEK293 cells. Bigger field of view (upper) and zoom (bottom).

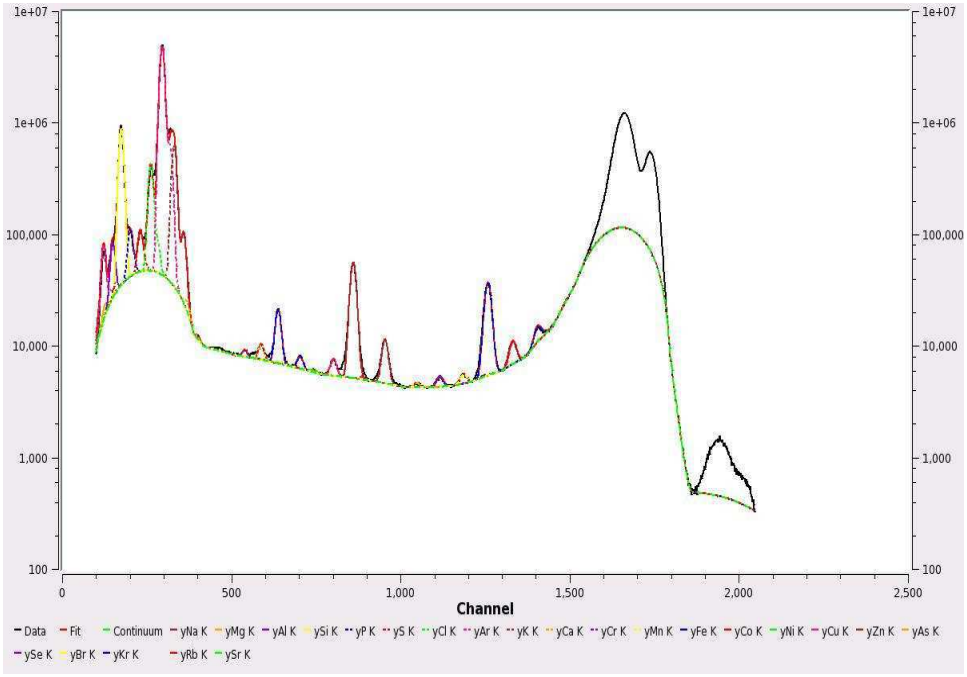

Figure 5.14: The fluorescence spectrum of the HEK293 cells with selected peaks.

5.15.

5.3.2 X-ray phase contrast of HEK293 cells

To acquire phase contrast data, sample is moved out of the focus. The data is collected at four distances (29 mm, 30 mm, 34 mm, 44 mm) corresponding to a pixelsize of 50 nm. The need of multiple distances is related to the phase retrieval procedure [33]. After applying phase retrieval algorithm to the collected data a phase map is generated (Fig. 5.16). Similarly to what has been done in 5.2.2 the thickness of a selected area (see Fig.5.16) can be calculated as well. This calculation requires applying an average density of a cell, 1.218 g/cm^3 [54], so it introduces some uncertainty. This problem is solved in the next Chapter where absolute quantification is made. However for the purpose of immediat and general comparison with an AFM result (see next section), this calculation is sufficient and it gives a result of about 3.1μm.

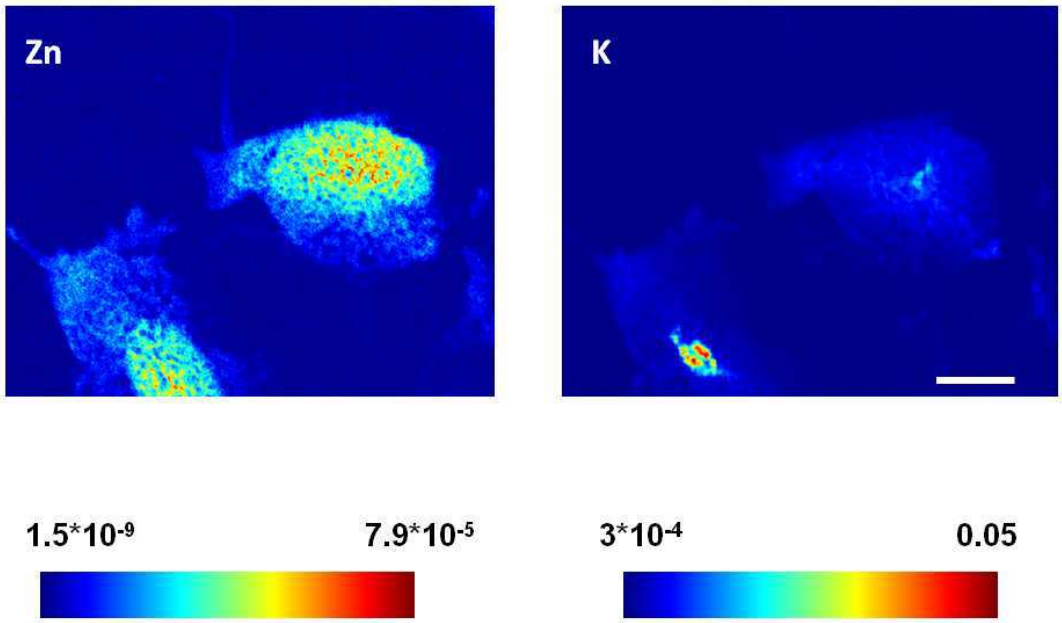

Figure 5.15: X-ray Zn (left) and K (right) fluorescence maps of HEK293 cell. Scale bar 6 μm. Color scale bar indicates minimum and maximum content (assuming ρ= 1g/cm^3 and thickness T= 2 μm in PyMCA) of Zn (left) and K (right) in the cell. The colors are scaled to the maximum of each map.

5.3.3 Atomic Force Microscopy of HEK293 cells

The same steps were repeated as for the bacteria AFM experiment. The main difference is that cells HEK293 were imaged on the frame (due to a risk of breaking membrane, it was a first time when we used AFM for our samples) while the bacteria were imaged on the membrane (as the result from previously imaged HEK cells on the frame was satisfactory, we have decided to try imaging on a membrane). Therefore cells imaged by AFM are different than the ones imaged by X-rays. Cells were firstly investigated under the optical microscope and once the area was chosen (Fig. 5.17) the cells were deposited in the AFM machine. Imaging was performed with the tapping mode. The

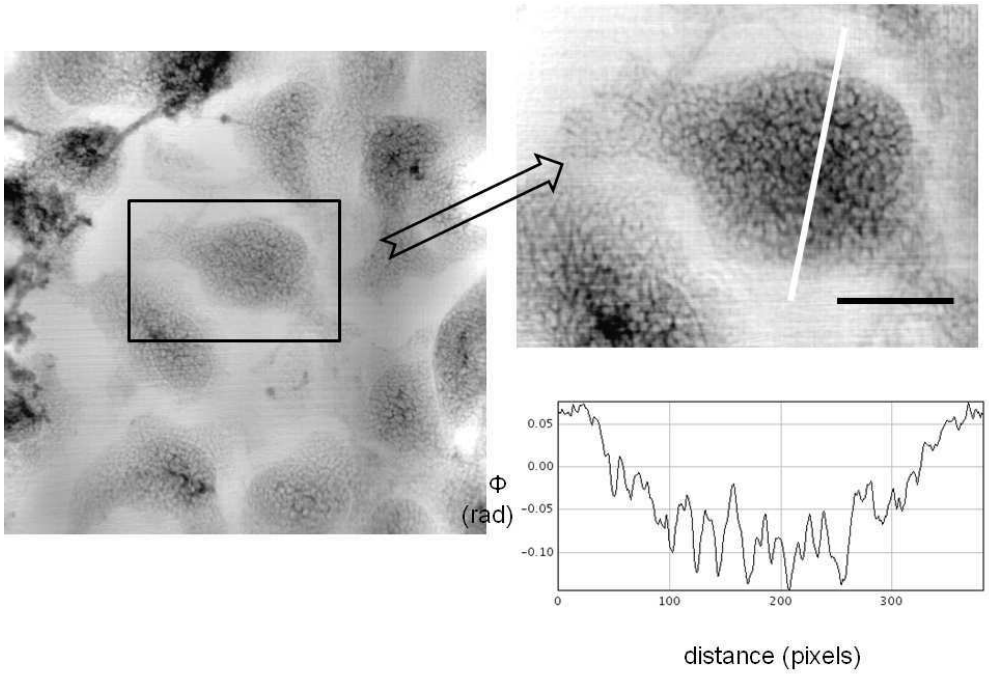

Figure 5.16: X-ray phase map of HEK293 cells together with a profile along the white line. Scale bar 6 μm. The black rectangle is shown in more detail on the right. It corresponds to the area scanned in fluorescence mode.

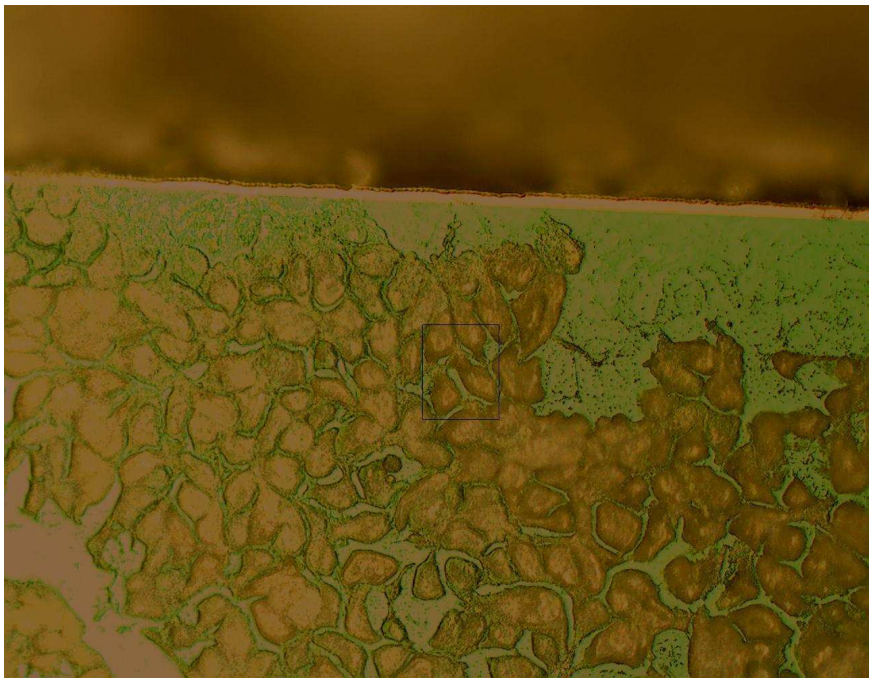

Figure 5.17: Optical view (not comparable directly with Fig.5.18) on selected for the AFM imaging cell HEK293 (black square).

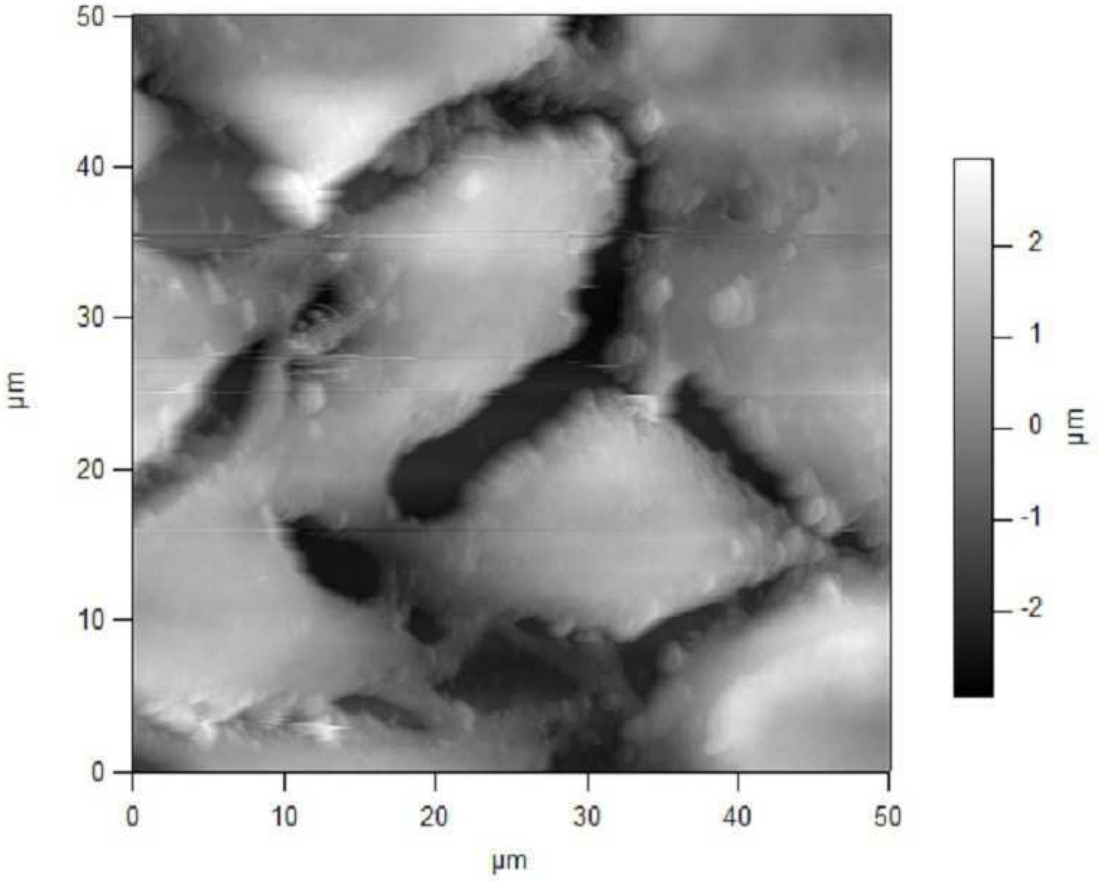

Figure 5.18: The AFM image of the selected HEK293 cell. The cells are deposited on the 200 μm thick silicon nitride frame.

scanning size was 50 μm with scan rate 0.3 Hz and 1024 lines. Result is presented on the Fig. 5.18. As can be seen on the color bar, the cell thickness is similar to the one estimated for the phase imaging.

Résumé du Chapitre 5 en Français

Ce chapitre présente les possibilités respectives de l'imagerie X en contraste de phase et de la nanosonde par fluorescence X excitée par le rayonnement synchrotron appliquée à divers objet biologiques. Dans un premier temps nous utilisons un objet test dont les motifs en or peuvent être imagés aussi bien par fluorescence X que par imagerie X en contraste de phase. Ceci permet de bien illustrer la procédure que nous utilisons tout au long de ce travail de thèse afin de combiner sur un même objet les informations issues de ces deux techniques respectivement d'imagerie chimique et structurale. Nous avons choisi d'explorer dans un premier temps des bactéries dont la taille est représentative d'organites retrouvés au sein des cellules puis sur cellules entières HEK -293 très largement utilisées en recherche en biologie cellulaire. Ces cellules épithéliales de rein humain sont très facile à cultiver et à transfecter et représente un système efficace pour la production de protéines recombinantes par exemple. Cette première approche nous a permis de montrer que l'imagerie X de phase et des mesures AFM de ces objets sont en bon accord. Si les informations issues de la fluorescence X et de l'imagerie de phase semblent difficiles à combiner pour les bactéries cela est tout à fait réalisable avec une haute résolution sur des cellules entières.

Chapter 6

Absolute metal quantification

This chapter is based on the article published in the Journal of Structural Biology: **E. Kosior, S. Bohic, H. Suhonen, R. Ortega, G. Devès, A. Carmona, F. Marchi, J.F. Guillet, P.Cloetens. "Combined use of hard X-ray phase contrast imaging and X-ray fluorescence microscopy for sub-cellular metal quantification." 2012, J. Struct. Biol. 177 (2) 239-247**

6.1 Introduction

Metals present as trace elements in biological systems play an important role in the cell metabolism [38], [39]. In any organism most of the intracellular processes are regulated by metals, such as proteins containing metal cofactors which catalyze biochemical reactions. Present in enzymes, they are involved in important biosynthetic pathways including the conversion of electrochemical to chemical energy, the biosynthesis of DNA, and an array of important metabolites [40]. The number of studies on trace elements is growing and nowadays their role in human health both in their natural occurance and via therapeutic drugs is recognized as crucial. Compounds containing metals are used for the diagnoses and treatment of diseases such as Alzheimer, Parkinson, cancer (treatment with cisplatin-based drugs in chemotherapy [41]) and to develop nanocomposites for gene therapy. Quantitative study of the distribution of trace elements at the sub-cellular level provides important information for the study of

the functions and pathways of metalloproteins and therapeutic approaches, especially in connection with the local chemical state of the element. To answer fundamental questions on the role of metal ions in these systems requires combination of different approaches across the multidisciplinary fields of biology, chemistry and physics.
The relevant information about trace elements in biological specimens increases with the sampling resolution. To probe the sub-cellular complexity of metal ion homeostasis mechanisms, one requires sub-micrometer resolution together with a sub-femtogram absolute detection limits due to the decreasing quantity of sample probed. X-ray fluorescence (XRF) analysis with a nanoprobe is the most direct and sensitive method to quantify the distribution of metals and other elements at the sub-cellular level [18], [19]. It provides high sensitivity for transition metals and other relevant trace elements together with the capability of penetrating and mapping whole cells.
Most of the details of cells are undetectable in hard X-ray microscopy due to the weak absorption contrast between structures with similar transparency. However the various organelles show wide variation in refractive index, that is, the tendency of the materials to bend light, providing an opportunity to distinguish them. The technique exploiting the refractive index (its real part) is phase contrast imaging. Methods based on phase contrast provide complementary information about cells by mapping the electron density. Information about the electron density combined with the average density of the sample allows to calculate its thickness, value which can be compared with alternative techniques (Scanning Transmission Ion Microscopy, Atomic Force Microscopy). We use such comparison for validating the method described in this article. In this work we limit our investigations to the 2D regime. Therefore the quantitative values are averaged over the sample thickness. The local concentrations would be accessible by combining the proposed method with 3D tomography techniques. Without going to the full 3D investigation the proposed method allows to avoid misinterpretations of X-ray fluorescence maps, which would result from the inability to distinguish if a change in fluorescence signal is due to a change in concentration or a change in sample thickness. Our method (combining XRF with phase contrast imaging) yields the projected mass fractions at the sub-cellular level after the sample preparation and thus it is sensitive to it. This represents possible future approach - to study at the sub-cellular level the influence of different sample preparation techniques on the cell integrity. Although, not discussed in the present paper, another interesting possibility would be to investigate the radiation damages of the sample and to correct for any possible mass loss due to

irradiation.

6.2 Methods

6.2.1 Sample preparation

Certified particles size standard - polystyrene spheres (Duke Scientific Corp, Palo Alto, CA) and PC12 cells were analysed. Polystyrene spheres were of four different diameters (400 nm, 1μm, 5 μm, 10 μm). The commercial solution was diluted 5 to 10 times, deposited on a silicon nitride (Si_3N_4) membrane, spin coated and air dried at room temperature.
PC12 cells, a clonal catecholaminergic cell line derived from rat pheochromocytoma [42] were cultured in RPMI 1640 medium supplemented with 10% (v/v) heat-inactivated horse serum, 5% (v/v) fetal bovine serum, penicillin (25 μg/mL) and streptomycin (25 μg/mL). Cultures were maintained according to standard protocols at 37°C in a 95% humidified incubator with 5% CO_2 as already described [43]. The cells were cultured directly on gelatin gel coated thin polycarbonate foil (2 μm thick). These targets were subsequently fastly cryofixed in liquid nitrogen, chilled isopentane (-160°C) and further lyophilized. PC12 cells synthesize and store dopamine in neurovesicles. In the presence of nerve growth factor (NGF), these cells develop an extensive network of neuronal-like projections, that is accepted as a model of catecholaminergic neurons and often used as an in vitro model for Parkinson's disease. The cells labelled B,C in this work, were exposed to 300 μM of Mn and cell A was exposed to 300 μM of Mn and brefeldin A, a molecule known to cause the apparent collapse of the Golgi stacks [44].

6.2.2 X-ray fluorescence

X-ray fluorescence is a phenomenon in which the material exposed to X-rays emits radiation, which has an energy characteristic of the atoms present. It allows studying the chemical composition of the sample. X-ray fluorescence analysis was performed at the nano-imaging station ID22NI (Fig.6.1), using the intrinsic monochromaticity of the undulators of about $\delta\lambda/\lambda \simeq 0.01$. The experimental station is located at a distance

of 63 m from the undulator source and at 37 m from the high power slits used as secondary source in the horizontal direction (25 μm slit opening). The synchrotron radiation is focused by an X-ray optical device consisting of two elliptically shaped mirrors acting in two orthogonal planes using the so-called Kirkpatrick-Baez geometry [35]. The mirrors are coated with a graded multi-layer. No other monochromator is used in the setup, resulting in a very high and unique X-ray flux (up to 10^{12} photons/s) at energies between 17 and 29 keV. In this work, the energy of the pink photon beam was set to 17.5 keV for all experiments. The focused beam was characterized by translation of a gold stripe of a nano-fabricated test pattern (Xradia, USA) recording both the transmitted intensity by a diode and the $Au - L_\alpha$ fluorescence emission line by a silicon drift detector (vortex-EX, SII NanoTechnology Inc., USA). The X-ray spot size was measured to be 76 nm horizontally by 84 nm vertically (FWHM). The samples were positioned in the focal plane of the KB system and translated by piezo-stages in the directions perpendicular to the beam. The X-ray fluorescence spectra of several samples were collected by the silicon drift energy dispersive detector positioned in the horizontal plane at 75° of the incoming X-ray beam. Based on the X-ray fluorescence energy spectrum, the areal mass (A_{mass}) of the element can be calculated through a fitting procedure. The samples being scanned were deposited on 3 x 3 mm^2 membranes made of 500 nm thick silicon nitride (Si_3N_4) (Silson, Blisworth, U.K.). A step-size of 150 nm was used and the dwell time varied from 150 to 250 ms.

6.2.3 Phase contrast imaging

When X-rays pass through an object, two scenarios, according to the refractive index n, are considered

$$n = 1 - \delta + i\beta \tag{6.1}$$

The x-rays can be absorbed, which effect is determined by the imaginary part of the refractive index, β. Image contrast is thus entirely due to absorption differences (emphasis is put on the corpuscular nature of photons) and the amplitude of the radiation changes.

The X-rays can also be retarded in the object. This phenomenon is used in phase contrast imaging, where the effects due to the decrement of the real part of the refractive index, δ, are exploited. A difference in the δ value between an object and the

background results in a phase shift between the wave transmitted through and outside the object. Due to this phase shift an interference pattern appears upon propagation. Emphasis is thus put on the wave nature of x-rays. The phase shift induced by the object can be described as

$$\phi(x,y) = -(2\pi/\lambda)\int \delta(x,y,z)dz \tag{6.2}$$

where z is the propagation direction and λ the wavelength.
Far from the absorption edges and considering the fact that the elemental content is dominated by the cellular architecture, comprised of light elements (C, N, H, O) in biological systems, the real part of the refractive index is approximately proportional to the density of the object, ρ.

$$\delta \approx 1.36 \times 10^{-6}\rho[g/cm^3]\lambda^2[\text{Å}] \tag{6.3}$$

thus the equation 6.2 can be simplified

$$\phi = \alpha\langle\rho\rangle T \tag{6.4}$$

where α is a known constant, $\langle\rho\rangle$ is the mean density and T is the thickness of the object, $\langle\rho\rangle T$ represents also the areal mass density of the cellular ultrastructure, denoted hereafter the projected mass.
Combining the information from the X-ray fluorescence map (the areal elemental mass) with the projected mass measured by the phase contrast one can calculate the projected elemental mass fraction:

$$C_i = A^i_{mass}/\langle\rho\rangle T \tag{6.5}$$

where C_i is a projected mass fraction of the element i averaged over the sample thickness.
The same experimental setup as described in 6.2.2 was used for the magnified phase contrast imaging but the sample was put downstream of the focus in the divergent beam (see Fig.6.1). Projection microscopy, which uses partial coherence of the incident beam is a simple way of phase contrast imaging through propagation [45], [46]. Samples were put at different distances (29 mm, 30 mm, 34 mm, 44 mm) downstream of the X-ray focus resulting in magnified Fresnel patterns collected by a highly sensitive charge-coupled device (CCD) camera. The need of multiple distances is related to the phase retrieval procedure [33]. The pixel size varied depending on the distance focus-sample, being set to 53 nm for the first distance (while the pixel size of the detector was 0.96 μm).

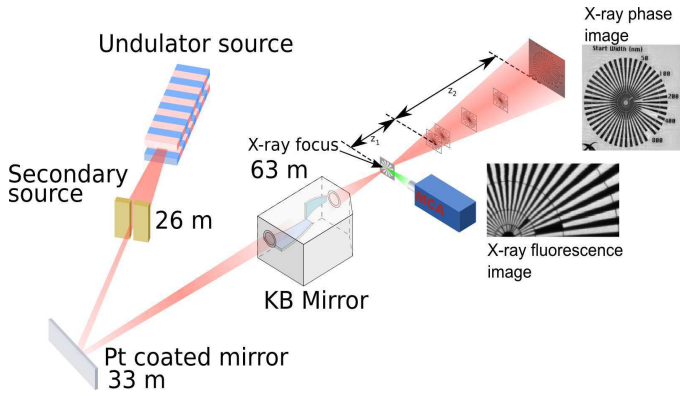

Figure 6.1: Scheme of the experimental setup of the nano-imaging station ID22NI

6.2.4 Atomic Force Microscopy (AFM) measurement

Atomic Force Microscopy allows imaging the surface morphology at nanoscale resolution and measuring the force at nano-Newton scale. AFM can investigate thin and thick film coatings, synthetic and biological membranes, metals, polymers, semiconductors and study locally the electric, magnetic or mechanical properties of the sample [47]. Thanks to its versatility, AFM became a tool of choice in biophysics [48]. Our measurements were performed in Tapping mode under ambient conditions on an Asylum MFP-3D AFM instrument equipped with acoustic box. In this MFP-3D AFM the planar scan relies on an (X,Y) scanner in closed loop while an independent piezoelectric element drives the Z displacement of the probe according to the open feedback loop control. A standard Tapping probe was used with a measured resonant frequency of 325 kHz and a cantilever stiffness of about 45 N/m (average value provided by the manufacturer data sheet). The AFM topographic images were recorded with a numerical resolution of 256 x 256 pixels. The tapping mode allows high-resolution topographic imaging of surfaces that are easily damaged or not hold tightly to their substrate. The Tapping mode is implemented in ambient air by exciting the cantilever assembly near the cantilevers resonant frequency using a dedicated piezoelectric crystal. Thanks to this mechanical excitation, the cantilever oscillates with amplitude of typically few tens of nanometers; this amplitude is modulated when the tip comes into contact with the surface. The AFM measurement was performed on polystyrene spheres of 5 μm diameter at the Surface Science Laboratory of the ESRF.

6.2.5 Scanning Transmission Ion Microscopy (STIM)

Scanning Transmission Ion Microscopy is based on measurement of the energy loss of accelerated ions after passing through the specimen. This slowing down of the charged particles occurs during inelastic collisions with electronic shells and is proportional to the stopping power of the sample and describes its atomic density. The experiment was performed at AIFIRA ion beam facility on nanobeam line [49]. Charged particles delivered by a 4 MV Cockroft-Walton electrostatic accelerator are focused onto the sample surface by an electromagnetic lens down to a beam spot size of 200 nm. The beam is scanned over the surface in order to measure local ion energy loss using a passivated implanted planar silicon (PIPS) detector placed on the beam axis very close behind the sample. This geometry results in increased detection efficiency, which enables drastic lowering of the beam current down to a few hundreds of particles per second. Therefore, the sample does not suffer any mass loss during ion interaction and one can access the projected mass of the sample [50].

6.2.6 Data analysis

X-ray fluorescence

For X-ray fluorescence analysis we used PyMCA, a free available software, which was developed at the European Synchrotron Radiation Facility [51]. The program allows interactive as well as batch processing of large data sets and is well suited for X-ray fluorescence imaging. Quantification of the elemental areal masses is based on a fitting procedure of the recorded fluorescence spectra. The algorithms employed are described in detail elsewhere [51].

Calibration of the fluorescence data

The Standard Reference Material (SRM) of bovine liver was used to calibrate the fluorescence spectra. This material is intended primarily for use as a control material and in evaluating analytical methods for the determination of major, minor and trace elements in animal tissue and other biological matrices.

Element	Standard value ($\mu g/g$)	Experimental value ($\mu g/g$)	Difference (%)
Potassium	9940 ± 20	7200 ± 9	-27.6
Copper	160 ± 8	169 ± 0.2	5.6
Iron	184 ± 15	166 ± 0.3	-9.8
Zinc	127 ± 16	128 ± 0.2	0.8

Table 6.1: Certified Values of Constituent Elements of the NIST SRM 1577B bovine liver together with the experimental values obtained after the optimization process together with their statistical uncertainties and the percentage of difference

The certified values for the constituent elements and the experimental values are given in Tab.6.1. Certified values are based on results obtained by definitive methods of known accuracy, or alternatively, from results obtained by two or more independent analytical methods. The grand mean was computed using the weighting scheme of Paule and Mandel [52].
The bovine liver sample was scanned through the focal plane and the spectrum of emitted fluorescence was recorded. The elemental content is calculated assuming the fundamental parameters (flux, detector characteristics) to be known except for the distance between the focus and the detector. This distance is not precisely known but it's evaluated by comparison of the calculated and known elemental content in the bovine liver sample.
Three elements were chosen as representative (Fe, Cu, Zn) and three distances close to the physical one. Using PyMCA the content of the chosen elements were obtained and used in the formula:

$$Y(x) = \sum_i (c_i^{st} - c_i^{exp}(x))^2, \;\; i = \mathrm{Fe}, \mathrm{Cu}, \mathrm{Zn} \tag{6.6}$$

where x is the distance between the focus and the detector, c_i^{st} is a content of the element i from the standard values, $c_i^{exp}(x)$ is a content of the element i measured in the experiment. The cost function $Y(x)$ was fitted with a second order polynomial and the value of x giving the minimum was taken to be true focus to detector distance.

Phase imaging

To analyze phase contrast data we used free, available ImageJ software and the phase retrieval code developed at the ESRF and implemented under GNU Octave ([34], [53]). The results obtained by using the phase retrieval algorithm allow to calculate the thickness of a certain area (as described in 6.2.3). This value can be compared with the alternative methods (AFM, STIM).

6.3 Results

6.3.1 Reference samples

Certified polystyrene spheres of well known diameter were used for validation of the phase retrieval algorithm. Samples were put at four distances as explained in 6.2.3. The phase retrieval algorithm provides relative phase maps (Fig.6.2). We draw profiles across the spheres to get information on the projected phase that can be used to calculate the thickness of the sample (as described in 6.2.3). By introducing the density of the certified polystyrene spheres that is 1.05 g/cm^3 we obtained the results shown in Tab.6.2. It provides the nominal values of the spheres diameter (certified values), the experimental values and the relative differences. It can be observed that the experimental values are systematically underestimated and that the relative difference is bigger for the smaller spheres. The sample that consists of 5 μm polystyrene spheres was also imaged by AFM and STIM, as they represent alternative methods for the thickness measurement. The results are presented in Fig.6.3 with associated profiles

diameters	nominal (μm)	experimental (μm)	difference (%)
0.4 μm	0.4 $\pm$ 0.004	0.357 $\pm$ 0.021	-10.75
1 μm	0.994 $\pm$ 0.021	0.95 $\pm$ 0.06	-4.43
5 μm	4.987 $\pm$ 0.04	4.91 $\pm$ 0.42	-1.54
10 μm	10.03 $\pm$ 0.05	9.77 $\pm$ 1.07	-2.59

Table 6.2: The nominal and experimental values obtained on the polystyrene spheres together with their statistical uncertainties and the percentage of difference

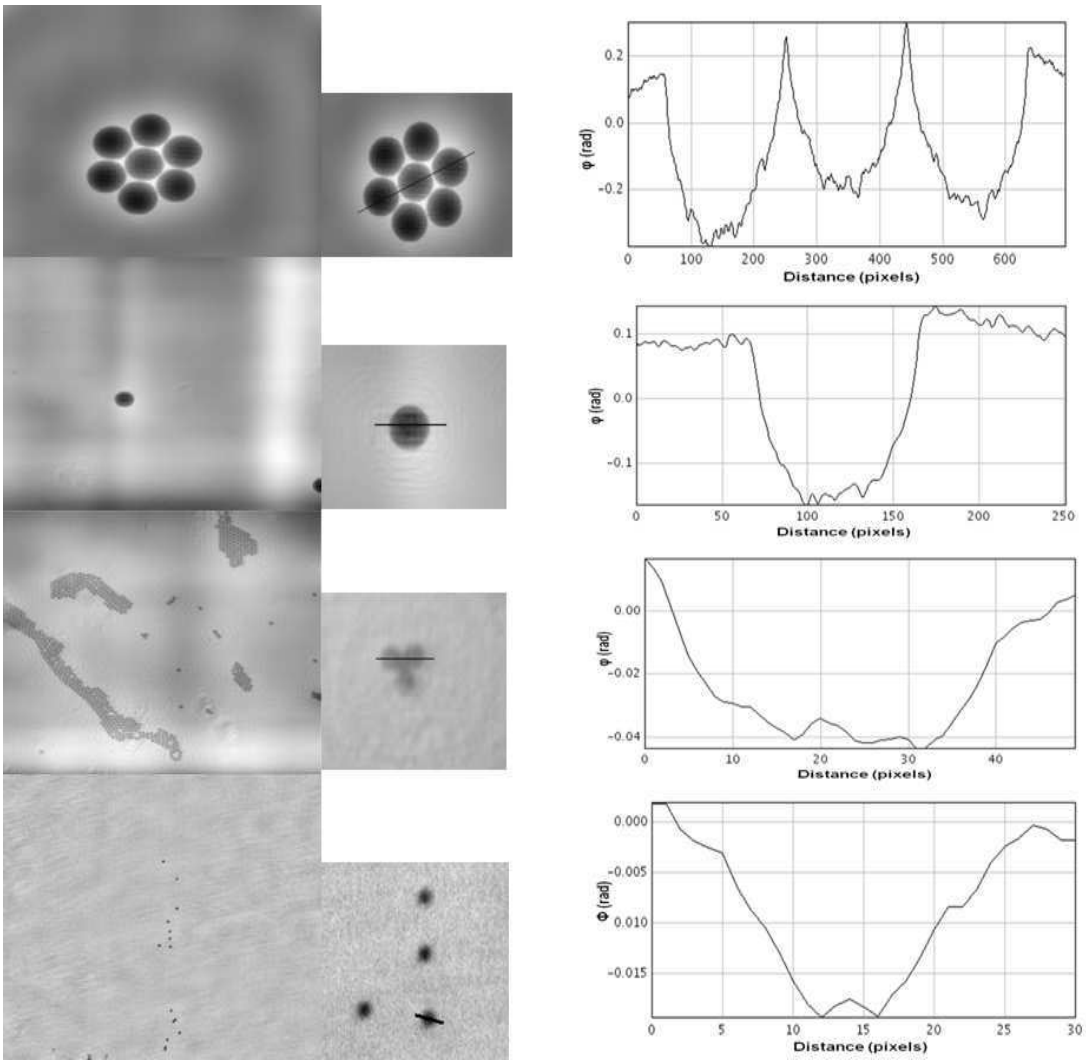

Figure 6.2: Relative phase maps generated after applying phase retrieval procedure to the certified polystyrene spheres of following diameters: 10.03 ± 0.05 μm, 4.987 ± 0.040 μm, 0.994 ± 0.021 μm, 400 ± 4 nm, together with selected profiles.

through one sphere. The same figure shows also a comparison between the different experimental results (phase, AFM, STIM) and the theoretical profile. STIM quantification of projected mass was performed using Paparamborde software [50]. Projected mass calculation is made by considering the slowing down of incoming particles through the bead and associated stopping power variation along the ion path. The ion path is schematically divided into elementary sub-layers with constant energy loss where stop-

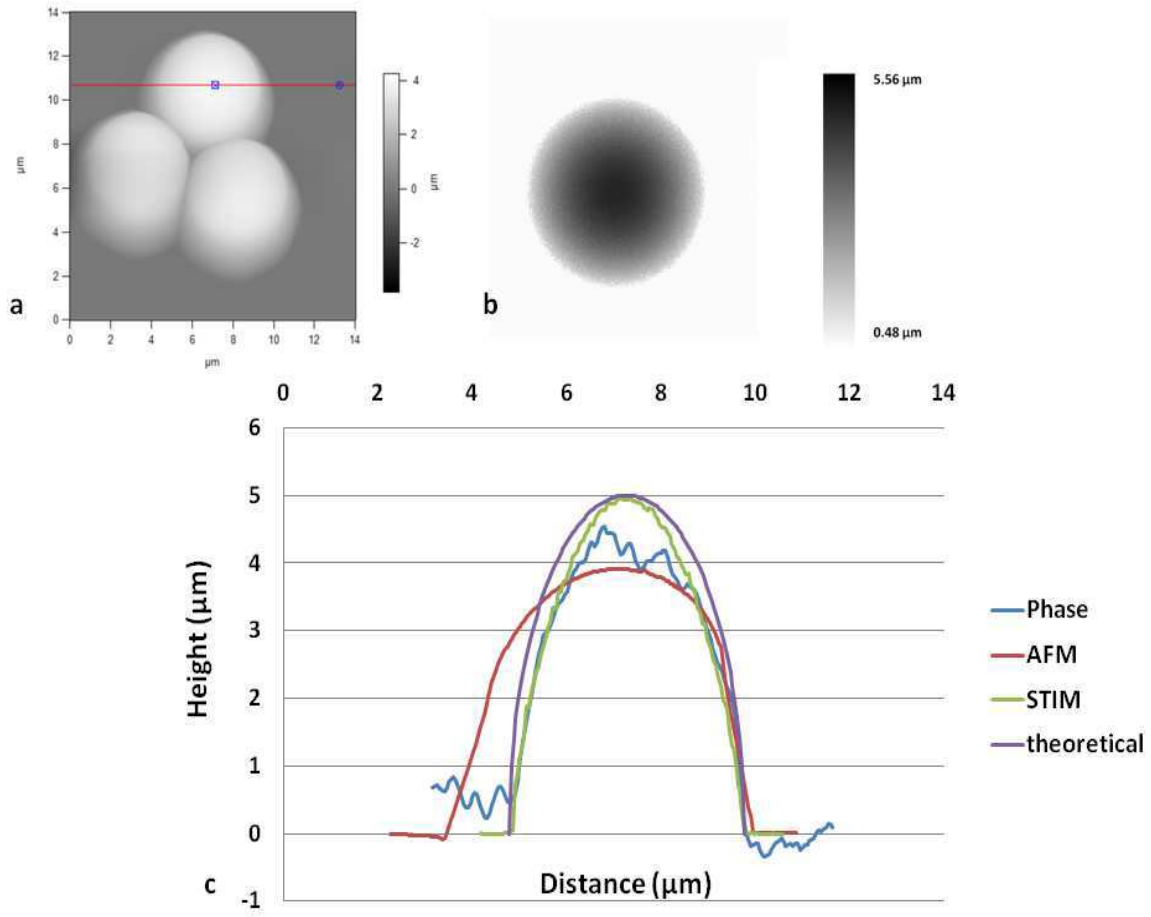

Figure 6.3: Comparison between different imaging techniques of the 5 μm spheres. a. the AFM image of the 5μm spheres, b. STIM image of the 5 μm sphere, c. comparison between the experimental profiles (phase, AFM and STIM) and the theoretical prediction.

ping power and corresponding mass can be calculated. Total projected mass is then calculated giving weight to every sub-layer according to the total transmitted energy spectra. In the case of the polystyrene sphere calculation, the Si_3N_4 contribution to the total energy loss was measured directly on transmitted map and used as a fixed parameter for sphere projected mass calculation. Accuracy in STIM mass measurement is driven by the nature of sample and background and remains here under 16% for the less favourable case (5 μm sphere on Si_3N_4 layer).

6.3.2 Element mapping in PC12 cells

PC12 cells were imaged by synchrotron X-ray fluorescence and X-ray phase contrast imaging. After scanning the sample (as described in 6.2.2) and fitting the emitted spectra, the intracellular distribution of the accessible chemical elements can be determined at a spatial resolution corresponding to the beam size (100 nm). By applying the phase retrieval algorithm, the relative phase maps were generated. The potassium (K) and zinc (Zn) X-ray fluorescence map and phase contrast images after phase retrieval reconstruction acquired on typical NGF-differentiated PC12 cells are presented in Fig.6.4. Fig. 6.5 shows images of the same PC12 cell obtained using the STIM method and both X-ray fluorescence and X-ray phase contrast imaging. For every cell we calculated the minimal and maximal areal mass of the selected elements; potassium which is known to have a rather uniform distribution within the cell and zinc. The results are collected in Table 6.3. Using data from the reconstructed phase maps, similarly to what has been done for the reference samples, we can calculate the thickness of the PC12 cells analysed. The profiles along selected lines (shown in Fig. 6.4, 6.5) were used for calculation. Applying an average density of the dry cells of 1.218 g/cm^3 [54],[55] we calculate the maximum thickness of the cell A (along the selected profile) to be 2.87 μm. For the cell B we selected 2 profiles, one going through the cell (profile 2) and one going through a thin neuritic process between 2 cells (profile 3). The thickness of these areas are respectively: 6.17 μm and 1.28 μm. For the Zn fluorescence map of the cell B we selected also region of significant content of Zn, visible on the Fig. 6.4 and the corresponding region of high projected mass. We used this region to calculate the local areal mass of Zn ($51.16 \cdot 10^{-9}$ g/cm^2) and the thickness of this part (7.59 μm). These numbers will be used to calculate the absolute projected concentration

Cells	K		Zn	
	min (g/cm^2)	max (g/cm^2)	min (g/cm^2)	max (g/cm^2)
cell A	15.0×10^{-9}	1.9×10^{-6}	0	16.4×10^{-9}
cell B	0	7.3×10^{-6}	0	67.1×10^{-9}
cell C	6.5×10^{-8}	2.8×10^{-5}	0	85.0×10^{-9}

Table 6.3: Values of areal mass of K and Zn in PC12 cells.

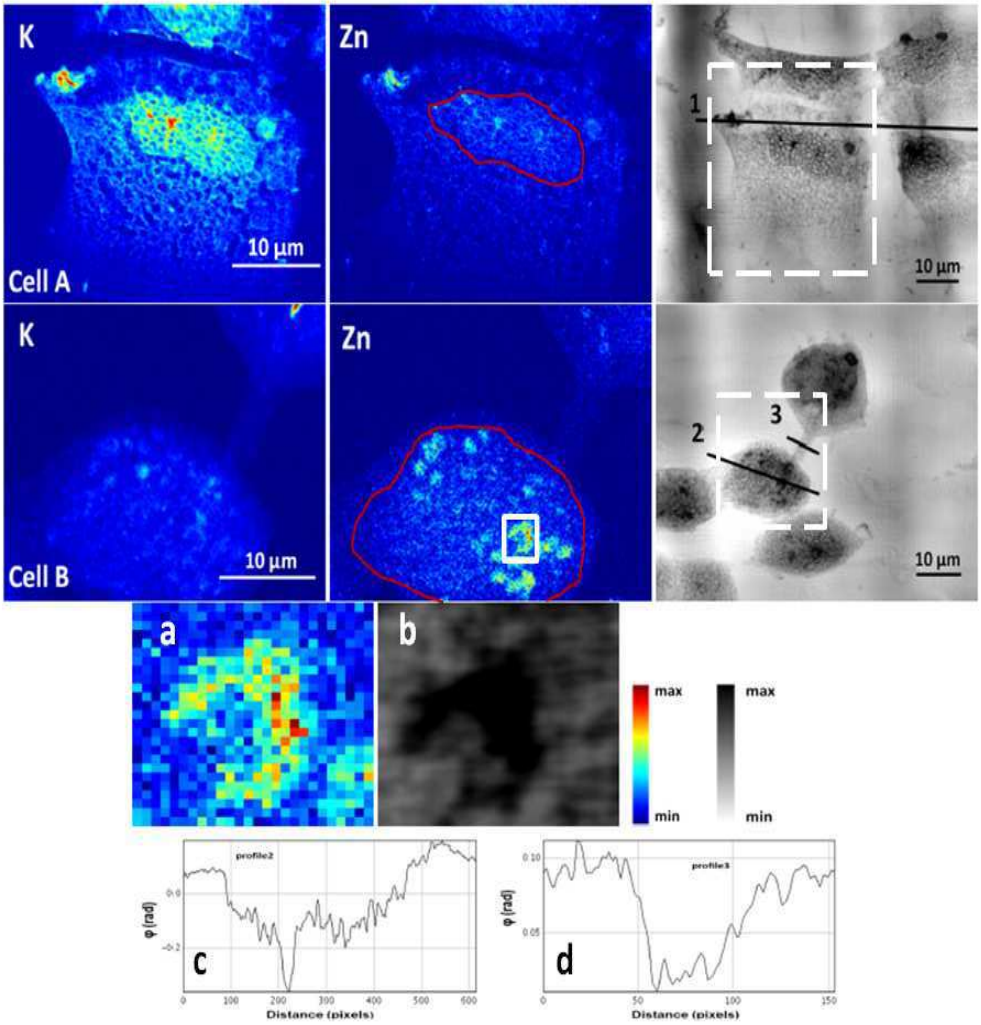

Figure 6.4: X-ray fluorescence (color) and phase contrast (black-white) maps of PC12 cells A and B. Dashed, white squares on phase contrast maps indicate the corresponding region on fluorescence map. The cell nuclei are highlighted in red. White square on Zn fluorescence map of the cell B was selected due to significant content of Zn (fluorescence map - a) and thickness (phase map -b); c. Profile 2, through the cell B; d. Profile 3, through the neuritic process. The colors depicting elemental content in each map are scaled to the maximum value for that map. The scanning size of the cell A was 307 x 308 pixels with dwell time 250 ms while for the cell B 194 x 176 pixels with dwell time of 150 ms

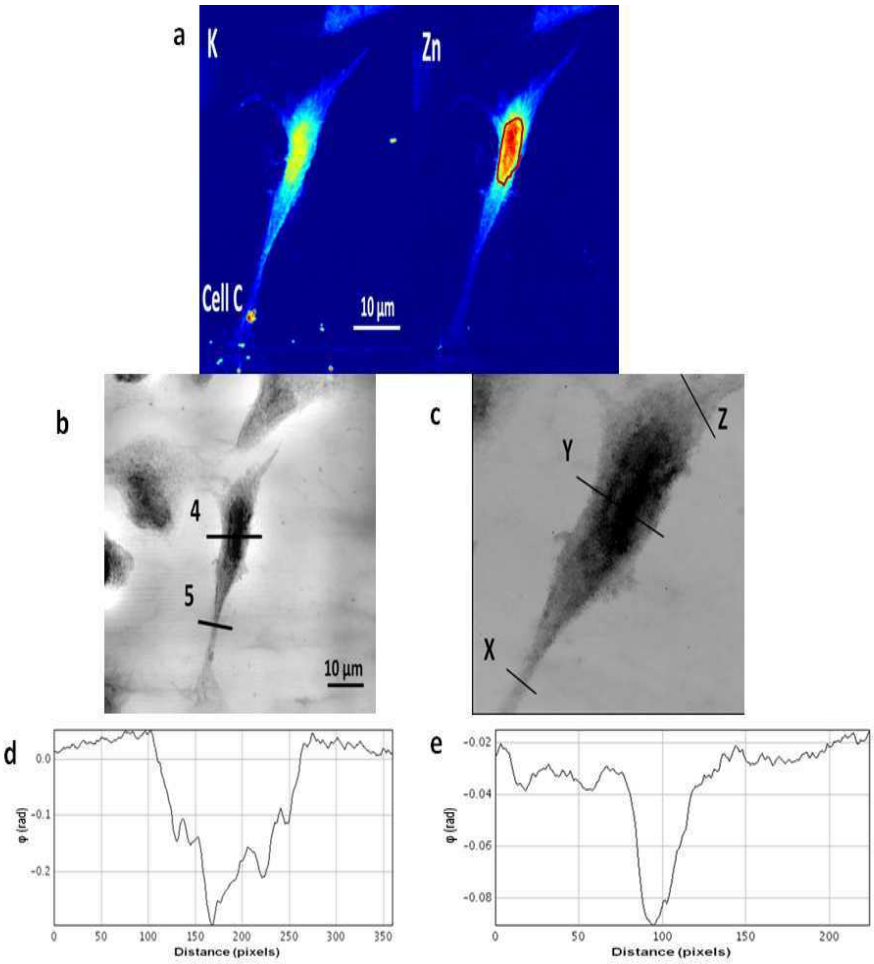

Figure 6.5: X-ray fluorescence (a), phase contrast (b) and STIM (c) map of the cell C. The cell nucleus is highlighted in red. On the phase map there are 2 areas selected for the thickness calculation; d. Profile 4 through the cell C, e. Profile 5 through the lower part of the cell. On the STIM map there are 3 selected areas X, Y, Z, which were chosen to calculate the areal mass. The colors depicting elemental content in each map are scaled to the maximum value for that map. The scanning size was 225 x 411 pixels and dwell time 200 ms.

of Zn in this region of the cell. Also for the cell C we selected 2 profiles, one going through the cell (profile 4) and one going through the lower part of the cell (profile 5). The thickness of these areas are respectively: 4.77 μm and 0.82 μm.
On the STIM map of the cell C we selected 3 areas that were used for areal mass

calculation. The area X was selected in one of the thinnest parts of the cell (similarly like profile 5 on the corresponding phase map) and it gave the result of 88 μg/cm^2 while the result obtained by using the phase map gives 100 μg/cm^2. The area Y goes through the nucleus of the cell (similarly like profile 4 on the corresponding phase map) and it yields 524 μg/cm^2. The similar area selected on the phase map gives a result of 581 μg/cm^2. As a curiosity we also calculate the areal mass in area Z, which goes through the cytoplasm, the result is 114 μg/cm^2 (with 150 μg/cm^2 calculated from the phase map).

After combining the information from X-ray fluorescence maps and phase contrast maps it is possible to calculate the absolute projected concentration for elements Zn and K in the cells (as described in the section 6.2.3). For these calculations and for easier comparison we used the maximal value of the areal mass and the thickness of the cell (along the selected profiles), although full quantitative maps can be derived combining both types of images (see Fig.6.6). The results are presented in Table 6.4. For the region of the cell B (significant content of Zn) mentioned above we calculate

	K (%)	Zn ($\mu g/g$)
cell A	0.54	46.9
cell B	0.97	89.3
cell C	4.82	146.3

Table 6.4: Projected concentration of K and Zn in PC12 cells obtained by dividing the maximal value of areal mass by the thickness of certain area.

the absolute projected concentration of Zn at the level of 55.3 $\mu g/g$.

In the Fig.6.6 we present the quantitative map of the projected mass fraction of Zn in cell B. By using the X-ray fluorescence map of Zn and the phase contrast map of the cell B (Fig.6.4) it is possible to access the projected concentration by dividing both maps pixel by pixel. Before the division we used cross correlation techniques to align the images and we applied small distortion corrections. It should be noted that it is not necessary to calculate the thickness of the sample in order to determine the projected concentrations of a given element as this information is accessible by dividing X-ray fluorescence and phase contrast images pixel by pixel (see equations 6.4, 6.5). By doing the above calculations and comparing the results obtained by our method in terms of sample thickness and areal mass with an alternative method such as STIM, we validate

our method.

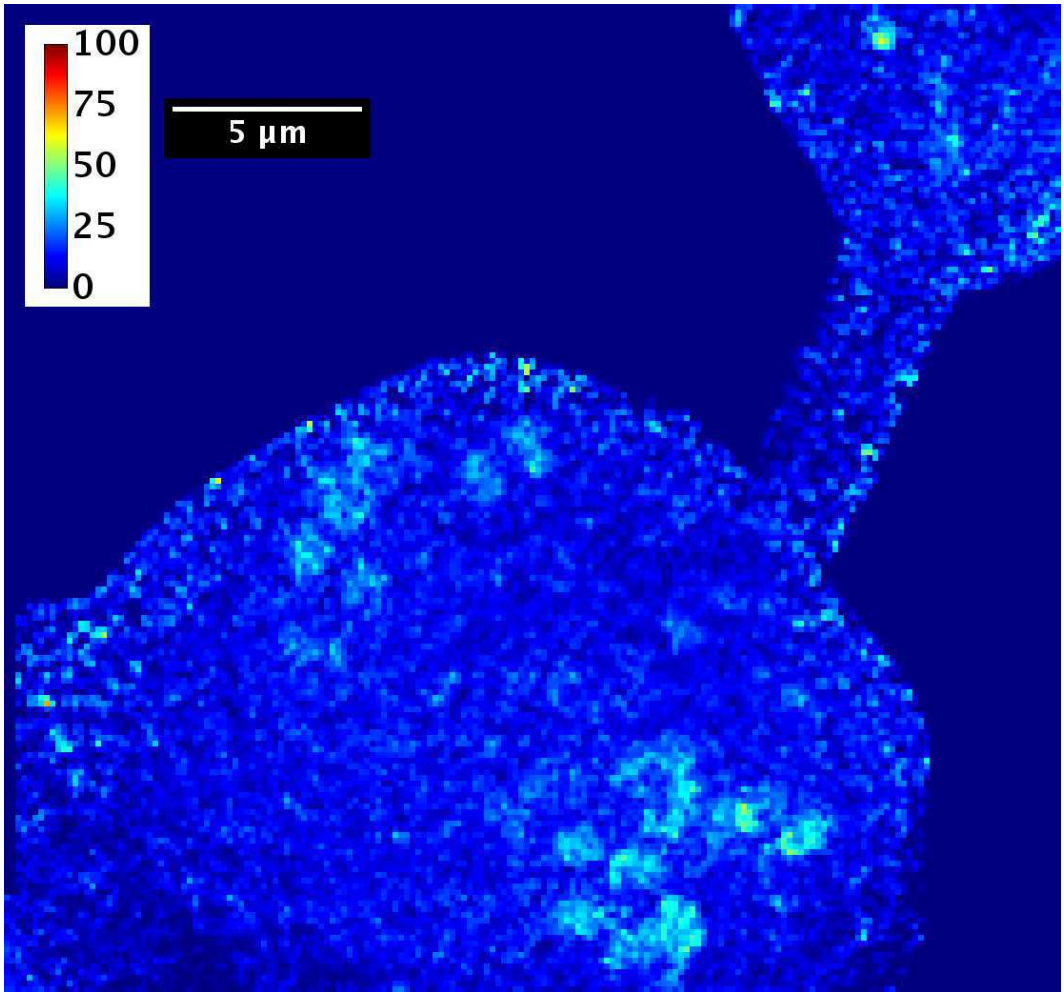

Figure 6.6: Fully quantitative map showing the projected mass fraction of Zn in the cell B. The calibration bar is in *ppm*. The map was created by combining the X-ray fluorescence map of Zn and the phase map of the cell B by dividing both images pixel by pixel.

6.4 Discussion

An important application of X-ray fluorescence microscopy is the determination of the distribution of the chemical elements at the sub-cellular level. Indeed, XRF analysis is a multi-element analytical technique that allows the simultaneous quantification of almost all elements in an unknown sample. The case of cells or thin sections of tissue is ideal in the way that corrections for absorption and enhancement effects are not necessary resulting in linearity between fluorescence intensity and the projected mass of a given element. However, the mapping of true element concentration at the sub-cellular level is a difficult task. Locally, the composition and the density or the thickness of different sub-cellular compartments can vary. Indeed, cell organelles are a mixture of structures with different size, weight and shape. The region of the cell nucleus is a few microns thick while some parts of the cytoplasm can be only 100 nm thick. It has been reported using combined STIM and AFM method that within a same cell specific densities vary between 1.06 to 1.86 [50]. This should be taken into account for true elemental quantification at sub-cellular level. To address this problem, X-ray fluorescence sub-cellular mapping and propagation-based X-ray phase contrast imaging for mass normalization were combined, for the first time, to provide high-resolution, truly quantitative, elemental distribution maps in cells. Phase-contrast imaging with a partially coherent beam produces Fresnel interference fringes, which makes it possible to image samples with small variations in mass density. These variations would be undetectable in absorption contrast.

Alternatively scanning differential phase contrast imaging has been performed by measuring the deviation of the beam by the sample with a position sensitive detector [45]. The authors have demonstrated a very good sensitivity of this approach using scanning transmission X-ray microscopy on 5 microns polystyrene spheres. Although, they did not use it yet for mass normalization for X-ray fluorescence quantitative analysis, the results obtained were done at low energy (2.5 keV) that limits the range of elements accessible. Recently the studies on Zernike Phase Contrast have shown the possibility of obtaining the projected phase in scanning mode [56] also X-ray fluorescence was combined with non-synchrotron technique, AFM in order to access absolute metal concentration [57]. Compton to Rayleigh scattering analysis has been used to obtain more accurate quantification in 2D [58] or 3D [59] measurements. There is limitation to this approach, so far the matrix mean atomic number is estimated from calculated

Compton/Rayleigh intensity ratios as a function of the average atomic number in various samples which not necessarily match the sample matrix studied. In addition the thickness needs to be determined from thickness calibration curves on the basis of the total Compton scatter intensity. On the overall these average values based on Compton signal seem not suited to provide absolute quantification at the sub-cellular level. The projection X-ray microscopy method used in our paper is optimized for relatively high energies (17 keV-29 keV) that match well with efficient excitation of the X-ray fluorescence. As a full-field CCD based approach our method is more dose efficient, provides a larger field of view and is much faster than scanning methods to obtain the phase information. For comparison, the phase images are acquired with a few seconds of exposure time and contain 4 million pixels (1 μs/pixel), whereas the fluorescence scanning data requires about 6 hours of exposure time for 100000 pixels (250 ms /pixel). However the phase data is not recorded simultaneously with the XRF data as it is in [56]. Therefore to normalize the fluorescence data the alignment of the two different data sets is required. The higher energy of excitation for X-ray fluorescence allows not only a better sample penetration but allows also to reach almost all element with $Z > 13$ with the advantage to work with K emission lines for higher fluorescence yield and better energy resolution.

Ion beam techniques have shown clear assets to obtain true elemental quantification by combining particle induced X-ray emission (PIXE) with Rutherford backscattering and/or STIM. The sensitivity and spatial resolution are much poorer than synchrotron-based XRF microscopy. Recently, efforts have been done towards the quantification of trace elements on cell cultures [43]. STIM allows to map with sub-micrometer resolution the variation in mass densities within single cells with calculated thicknesses in good agreement with AFM measurements [50]. In this work, first a comparison between reference techniques (AFM, STIM) was made on polymer microspheres to mimic, in size and composition, a typical biological specimen such as a cell. The X-ray phase imaging after the application of a phase retrieval reconstruction algorithm provides a map of the projection of the mass density of the sample that was converted to thickness knowing the polystyrene density. The calculated thickness profile for 5 microns spheres was found to be slightly underestimated using X-ray phase imaging. This can be explained by the shape of the background of the profile extracted from the X-ray phase signal and that is not corrected for. The varying background is the direct consequence of the sensitivity of differential phase contrast methods for low fre-

quency noise. This problem can be solved by improving the quality and stability of the beamline optics, resulting in a better correction for inhomogeneities of the incoming X-ray beam. The STIM data matches more closely the theoretical profile of the sphere. Here, microspheres were deposited on 500 nm thick silicon nitride membranes. The 2 layers, i.e the sphere and the silicon nitride membrane were separated using STIM calculation modified in accordance. There is not much discrepancy between STIM - phase - and theoretical profile as shown in Fig 6.3. The AFM topographic image provides two complementary measurements through the profile: a 4 μm in height and 5.1 μm for lateral dimension (measured at the half height of the microsphere, i.e 2 μm where the tip-object convolution effect can be neglected). These differences in height and lateral dimensions could be due to the absence of non-linearity correction of the piezoelectric element in Z direction while the planar scanner is corrected thanks to the closed feedback loop. Indeed, the AFM instrument is dedicated to accurate height measurements at sub-micronic scale where the non-linearity behavior can be neglected. For this reason, in our measurements, the lateral one is the more reliable. Based on this assumption, the lateral dimension matches with the diameter specification of the sphere data sheet.

The thickness measurements using X-ray phase images were in good agreement (within 5% except for the smallest spheres) when compared to the certified values for the sphere. We attribute the increased relative error for the smallest spheres to a spatial resolution effect: in the phase retrieval step we didn't take into account the finite point spread function of the detector. The quantitative measurements on single 400 nm spheres are encouraging for subcellular applications. Indeed, this typically matches the size of some organelles (lysosome, mitochondria) or some thin cellular processes (neurites, filopodia). This is well exemplified when PC12 cells were analyzed. These cells were differentiated into neuronal-like cells which, expands neuritic processes. The X-ray phase reconstructed images provide useful structural details giving evidence for subcellular compartments of various densities and a cell nucleus that can be well delineated. Further work will be needed for better identification of the structural details obtained in the phase images by coupling to fluorescence microscopy and organelle staining. We observed inside some PC12 cells denser regions, micrometric in size. The X-ray fluorescence signal of zinc was found much higher in these regions. While the zinc distribution can be first misinterpreted, the association of X-ray phase images (for mass normalization) to X-ray fluorescence quantification results in a projected zinc concen-

tration that remains rather similar to the one in other parts of the cell (see Fig. 6.6). The potassium signal is found homogeneous as expected [43]. This indicates that the cell integrity was preserved during the sample preparation. The areal mass obtained on PC12 cells through STIM and X-ray phase measurements are in good agreement both for a thick part of the cells like the nucleus and for thinner parts like neurites. These direct comparisons on the same cellular regions support the use of X-ray phase imaging for mass normalization in X-ray fluorescence quantification. The same cells were imaged by STIM, then by X-ray phase imaging followed by X-ray fluorescence measurements. Despite short acquisition times (150-250 ms) and low attenuation at high X-ray energies, the high X-ray photon flux delivered by the nanoprobe results in non-negligible radiation damage. It is suggested that some mass loss occurs and our approach could be used to better characterize these effects. X-ray fluorescence microscopy is a unique tool for the quantification of trace elements at the sub-cellular level and it can be applied to a wide variety of biological studies. On the overall this work is encouraging the use of X-ray phase imaging to improve the elemental quantification in 2D and 3D X-ray fluorescence imaging.

6.5 Acknowledgements

We would like to thank the European Synchrotron Radiation Facility for providing the beamtime. This work was supported in part by the ANR Program PIRIBIO (ANR-09-PIRI-0029-01).

Résumé du Chapitre 6 en Français

Le chapitre 6 présente le travail que nous avons conduit pour valider la méthode d'imagerie X par contraste de phase pour déterminer la masse surfacique de cellules

isolées à l'échelle sub-cellulaire. Il est ainsi possible de corréler cette information avec la masse surfacique des éléments chimiques déterminés à cette même échelle par fluorescence X pour aboutir á une quantification absolue en tout point de la cellule. Cet aspect quantitatif absolu à l'échelle sub-cellulaire était jusqu'alors impossible; les aspects quantitatifs se basant sur un élément comme standard interne ou encore sur un standard externe dont la matrice et les concentrations certifiées par d'autres méthodes d'analyses sont similaires à l'échantillon étudié. Cependant à l'échelle sub-cellulaire les variations en densité et en composition chimique au sein de la cellule par exemple peuvent être fortes. La méthode proposée permet de prendre en compte ces hétérogénéités pour calculer la fraction massique absolue en éléments. Nous avons tout d'abord évalué l'imagerie X de phase en utilisant comme objets test des sphères de polystyrène micrométriques et sub-micrométriques dont les résultats ont été comparés aux dimensions certifiées et aux mesures obtenues par AFM et par microscopie ionique en transmission et à balayage (STIM). Nous avons ensuite étudié des cellules PC12, modèle cellulaire qui a déjà fait l'objet d'études au laboratoire en collaboration avec le Dr. R. Ortega (CENBG, CNRS, Gradignan). Les mesures STIM ont été réalisées toujours dans le cadre de cette collaboration, et ce sur la plateforme de faisceaux d'ions de la région Aquitaine (AIFIRA, CENBG, Gradignan). Les mesures en contraste de phase ont été comparées à celles obtenues en STIM sur les mêmes cellules. L'ensemble des résultats montrent que la masse surfacique des cellules déterminée par imagerie X par contraste de phase est en très bon accord avec celle mesurée par la méthode de référence STIM que se soit pour des zones cellulaires épaisses (noyau cellulaire) ou très fines (zones du cytoplasme, prolongements neuritiques). Enfin, nous avons combiné cette information sur la masse surfacique de la cellule à celle de masse surfacique des éléments chimiques obtenue par fluorescence X à une échelle de 100 nm. A titre d'exemple, la répartition quantitative absolue notamment du zinc au sein de cellules PC12 à ainsi pu être obtenue pour la première fois.

Chapter 7

Evaluation of radiation damage

This chapter is partially based on the article:
E. Kosior, P.Cloetens, G. Devès, R. Ortega, S. Bohic. "Study of radiation effects on the cell structure and evaluation of the dose delivered by X-ray and α-particles microscopy." 2012, Appl. Phys. Lett. *in press*

7.1 Introduction

Radiation originating from various sources causes ionizations in the molecules of living cells (so called ionizing radiation). These ionizations consist in the removal of electrons from the atoms, forming ions or charged atoms. The ions formed then can go on to react with other atoms in the cell, causing damage. At low doses, such as received every day from background radiation, the cells repair the damage rapidly. At higher doses (above 1 Sv), the cells might not be able to repair the damage, and thus may either be changed permanently or die. Most cells that die are of little consequence, the body can just replace them. But those ones changed permanently may go on to produce abnormal cells when they divide. In the right circumstances, these cells may become cancerous.
In general, particles or photons with energies above about 10 eV are considered ionizing, no matter what their intensities. There are three main kinds of ionizing radiation (Fig. 7.1):

- alpha particles (α), which consist of He nuclei
- beta particles (β), which are essentially electrons
- X-rays and gamma (γ) rays, which are energetic photons

Free neutrons (n) are able to cause many nuclear reactions in a variety of substances no matter their energy, because in many substances they give rise to high-energy nuclear reactions, and these (or their products) liberate enough energy to cause ionization. For this reason, free neutrons are normally considered effectively ionizing radiation, at any energy. High-energy β particles may produce bremsstrahlung (Fig. 7.1) as they

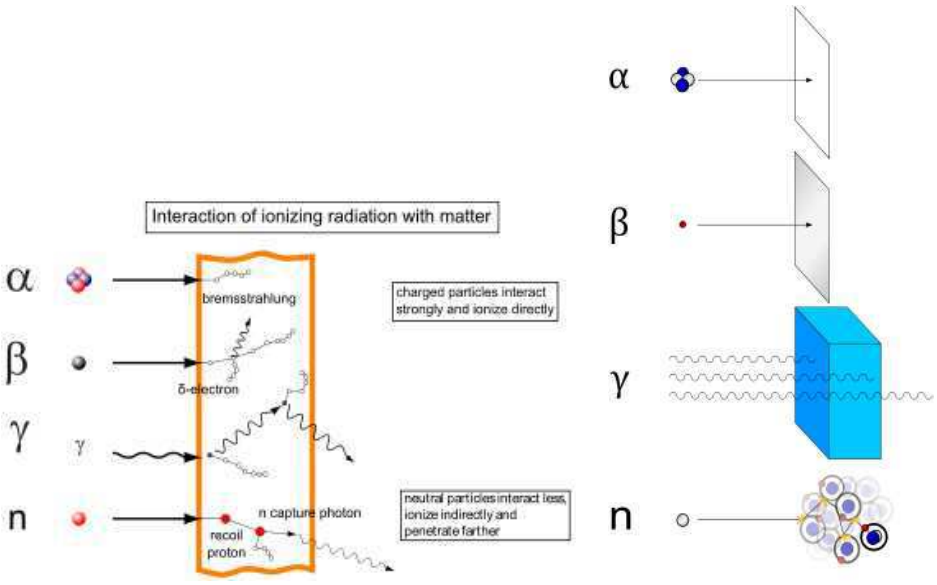

Figure 7.1: Left picture shows different types of radiation. Gamma rays are represented by wavy lines, charged particles and neutrons by straight lines. The little circles show where ionization processes occur. Right picture shows the possibility of penetration by mentioned radiation. Alpha particles are the least penetrating, simple paper sheet is sufficient to stop this radiation. Beta radiation requires an aluminium plate to be stopped while for the gamma radiation a dense material is needed. Neutron radiation consists of free neutrons that are blocked using light elements, like hydrogen, which slow them down and/or capture them. Source: Wikipedia

pass through matter, or secondary electrons (δ-electrons); both can ionize in turn.

Bremsstrahlung are emitted X-rays associated with the energy loss while decelerating. Its intensity increases with the increase in energy of the electrons and the atomic number of the absorbing medium.
Gamma rays do not ionize all along their path (like α and β particles), but interact by: the photoelectric effect, the Compton effect (shown as an example on the Fig. 7.1), and pair production. In the same figure, the neutron collides with a proton of the target material, and then becomes a fast recoil proton that ionizes in turn. At the end of its path, the neutron is captured by a nucleus in an (n,γ)-reaction that leads to the emission of a neutron capture photon. Such photons have enough energy to ionize.
Radiation that has enough energy to move atoms around in a molecule or cause them to vibrate, but not enough to remove electrons, is referred to as non-ionizing radiation. Examples of this kind of radiation are sound waves, visible light, and microwaves.

7.1.1 Units

There are different units related to ionizing radiation. Some of the radiation effects are measured in units of exposure:

- C/kg (Coulomb per kilogram) is the SI unit of ionizing radiation exposure and relates to a radiation required to create 1 C of charge per unit mass
- The Roentgen (R) is and old unit, not used anymore. 1 Roentgen = 2.58×10^{-4} C/kg

In the case of damages caused to matter (especially biological one) more meaningful is the absorbed dose, which is the amount of energy deposited per unit mass:

- The gray (Gy) is the SI unit of absorbed dose, measured in J/kg
- The rad (radioactivity absorbed dose) is the traditional unit, 100 rad = 1 Gy

However the same absorbed dose of different kinds of radiation causes not the same damages (for example 1 Gy of α particles radiation causes more damages than 1 Gy of X-ray radiation). To deal with these differences the equivalent dose was defined. It is

photons (γ, X)	1
electrons	1
neutrons	5 to 20
protons	5
solar particles, heavy ions	20

Table 7.1: Radiation weighting factor

gonads	0.08
bone marrow, breast, colon, stomach, lungs	0.12
bladder, liver oesophagus, thyroid	0.04
brain, skin, bony surfaces	0.01
other	0.12

Table 7.2: Weighting factors for organs and tissues (from ICRP Publication 103)

calculated by multiplying the absorbed dose by the weighting factor which depends on the radiation kind (see table 7.1), the means of exposure (internal or external) and the specific sensitivity of the organs or tissues (see table 7.2). The weighting factor is also called the Q (quality) factor or RBE (relative biological effectiveness of the radiation). The units of equivalent dose are sievert (Sv) - SI unit and rem (Roentgen equivalent man), 1 Sv = 100 rem. By definition, the effective dose, expressed in Sv, can only be used to assess the risk of the appearance of stochastic effects in man, and cannot be used either for acute effects nor for the effects on the fauna or flora. Because these units are relatively large, typically effective doses are expressed in mrem or μSv.
Table 7.3 presents a few examples of effective dose one receives during some medical checks and from different sources.

7.1.2 Radiation effects in X-ray fluorescence microscopy

The deleterious effect of radiation damage is a limiting factor in sub-cellular chemical analysis by synchrotron-based X-ray fluorescence (SR-XRF). XRF nanoprobe is the most direct and sensitive method to image and quantify the distribution of metals and other elements at the sub-cellular level [18], [19]. However the method is slow: scanning an entire cell may take a few hours as it requires a step size in the range of 100 nm

airplane ride (39000 ft)	5 μSv/h
cosmic radiation (sea level)	0.26 mSv/year
radionuclides in the body (i.e. potassium)	0.39 mSv/year
chest X-ray	80 μSv
dental X-ray	0.1 mSv
cervical spine X-ray	0.22 mSv
lumbar spinal X-rays	1.3 mSv
CT (head and body)	11 mSv

Table 7.3: Doses from various sources

and a dwell time of about 100 milliseconds. During this time the structure of the cell may change permanently.

The SR-XRF technique is similar to non-synchrotron techniques such as scanning electron microscopy coupled with energy dispersive X-ray analysis (SEM-EDXA) or particle-induced X-ray emission (PIXE). However the advantage of SR-XRF resides in its sensitivity (0.1-10 μg/g) related to a high incoming photon flux, the beam tunability and weak scattering [60]. As the physics of photon interaction with matter is simple and well understood, ab initio quantification is rather straightforward. Started from the *water window* spectral region and extended to the hard X-ray energy range, full-field and scanning X-ray microscopy aim to provide quantitative high resolution images. With several advantages such as label-free sample preparation and large penetration depth [61], X-ray microscopy is very complementary to electron and visible light microscopy. Although X-rays are less destructive than electrons or charged particles, radiation damage in multi-exposure experiments such as X-ray tomography creates limits [62], [63], [64]. Hard X-rays, with energy above 6keV, are known to cause less damage than soft X-rays due to much reduced absorption by the biological matrix and less ionizing capabilities. Nevertheless it has been observed that hydrated cells suffer from mass loss and shrinkage while investigated at doses required for high resolution imaging [65]. On the other hand this effect is greatly reduced by using cryogenic sample preservation methods [66], [67] but although mass loss effects do not occur the chemical state was observed to be changed [68]. X-ray microscopy experiments at 113 K and 50 nm spatial resolution have shown no observable mass loss with radiation doses up to 10^{10} Gy [69], [70]. Monitoring radiation damage effects during microscopy experiments is crucial to ensure the integrity and quantitativeness of the results. We propose

a method capable of studying structural damage and estimating mass loss occurring in cells during XRF nanoprobe analysis. This will allow appropriate corrections to determine truly quantitative elemental maps and to monitor radiation damage at the sub-cellular scale.

7.2 X-ray imaging of PC12 cells

For the radiation study purpose PC12 cells (see Chapter 6) were used. Two samples were selected. Both of them were incubated with 300 μM of iron but one was in addition treated with innocuous adenovirus of Synuclein which facilitates α-synuclein aggregation. In this section first evaluations will be presented, made on sample only exposed to iron. In the following section a more detailed study on the adenovirus treated sample set will be presented.
Firstly phase contrast data was collected, followed by a fluorescence scan and then again phase contrast data. For the cells presented on the Fig. 7.2 the step size was chosen to be 150 nm and dwell time 100 ms. Based on the phase contrast pictures (Fig. 7.2) it is possible to evaluate the difference in area between the original cell and the irradiated one. For this purpose one cell was chosen (first left). By comparing the

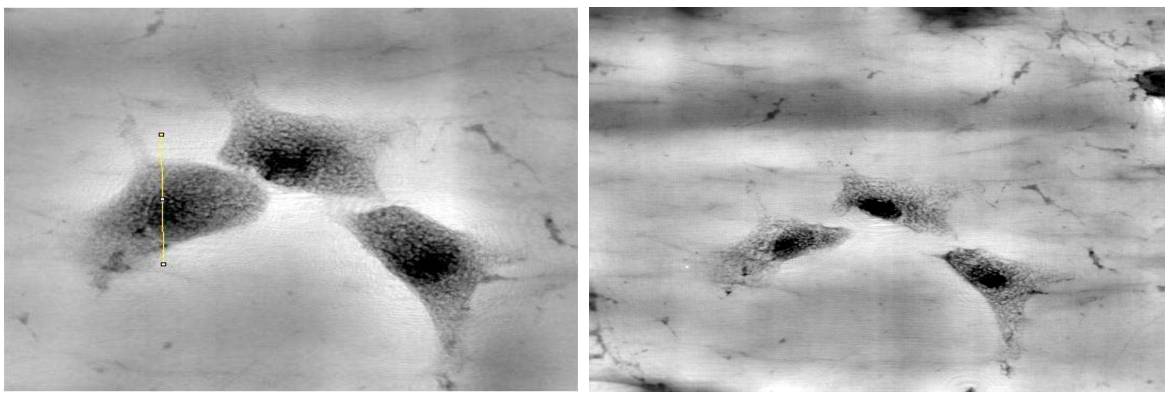

Figure 7.2: Left picture shows the phase contrast image of the PC12 cells, right one shows the same cells but after acquiring the fluorescence scan. For the calculation the first left cell from both images was chosen and the selected profile.

cell size, a difference of about 20% was found, this is due to the fact that cells simply

shrinked while the fluorescence scan was performed. As a reference, fluorescence maps of several elements are presented on the Fig.7.3. To access information on the cell

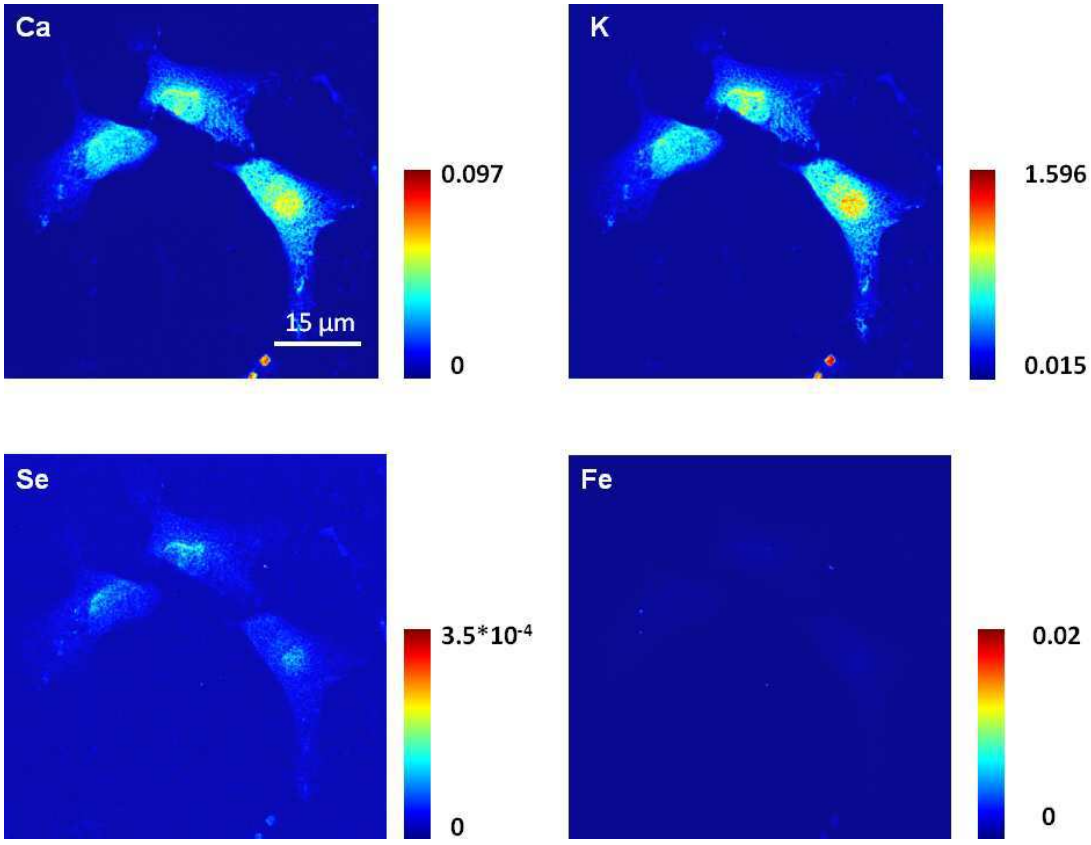

Figure 7.3: X-ray fluorescence maps of several elements (Ca, K, Se, Fe). Color scale bar indicates minimum and maximum content of certain element in the sample. The colors are scaled to the maximum of each map. Scanning size was 480x481 pixels.

depth one can make a profile through the cell (as it is visible on the Fig. 7.2 and a surface plot (Fig. 7.4). The grey value of the y axis refers to the projected phase, which can be translated into the thickness (as explained in the Chapter 6). The minimum value of the phase for the non-irradiated cell is about -0.231 while for the irradiated one it is -0.201. The maximum value is 0.059 and 0.037 respectively. The numbers of a difference minimum-maximum refer to a thickness of 4.0 μm for the non-irradiated cell and 3.2 μm for the irradiated one, which makes 20% of a difference. From this comparison we learn that due to irradiation the cell not only shrinks but also evaporates (decrease of the projected mass).

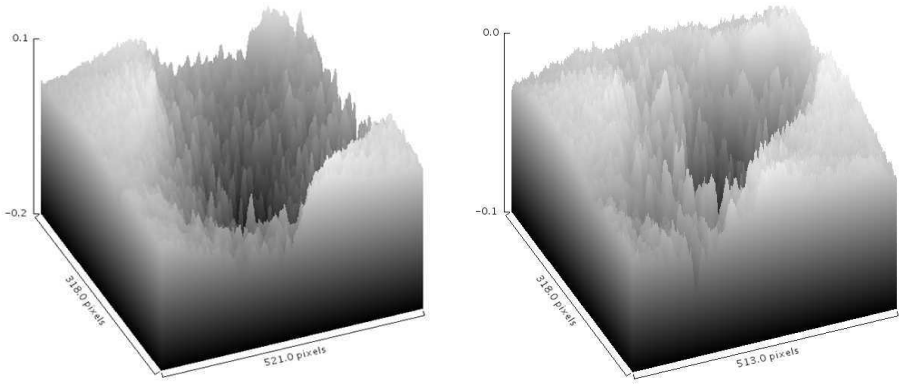

Figure 7.4: Left picture shows the surface plot of the selected cell before irradiation, right one shows the surface plot after acquiring the fluorescence scan.

7.3 Evaluation of a dose

7.3.1 Mass loss

The radiation effects were studied on PC12 cells. Cells that overexpress alpha-synuclein were incubated with 300 μM of iron. Details of the sample preparation are described in Chapter 6. The cells were cultured directly onto polycarbonate foil stretched over a polymer support. This target was placed in air and at room temperature on the sample stage of the nano-imaging endstation ID22NI at ESRF (see the description of the beamline in [71]). The energy of the beam was set to 17 keV. The specimen was imaged three times in order to record changes caused by the irradiation. Firstly phase contrast data was collected, followed by a XRF scan and then again phase contrast data. As the phase contrast data is acquired much faster and with a much lower dose, comparison of the phase contrast images after and before the XRF acquisition reveals the structural changes due to irradiation. Details of the experimental techniques are described in Chapter 6. In addition to the SR-XRF scanning and phase contrast imaging, STIM measurements were performed at the Applications Interdisciplinaires des Faisceaux d'Ions en Région Aquitaine (AIFIRA) platform [50]. STIM is a low-dose experiment which can be used for sub-cellular structural studies [43], complementary to X-ray phase contrast imaging. STIM was carried out using a 2 MeV alpha particles beam of about 250 nm diameter.

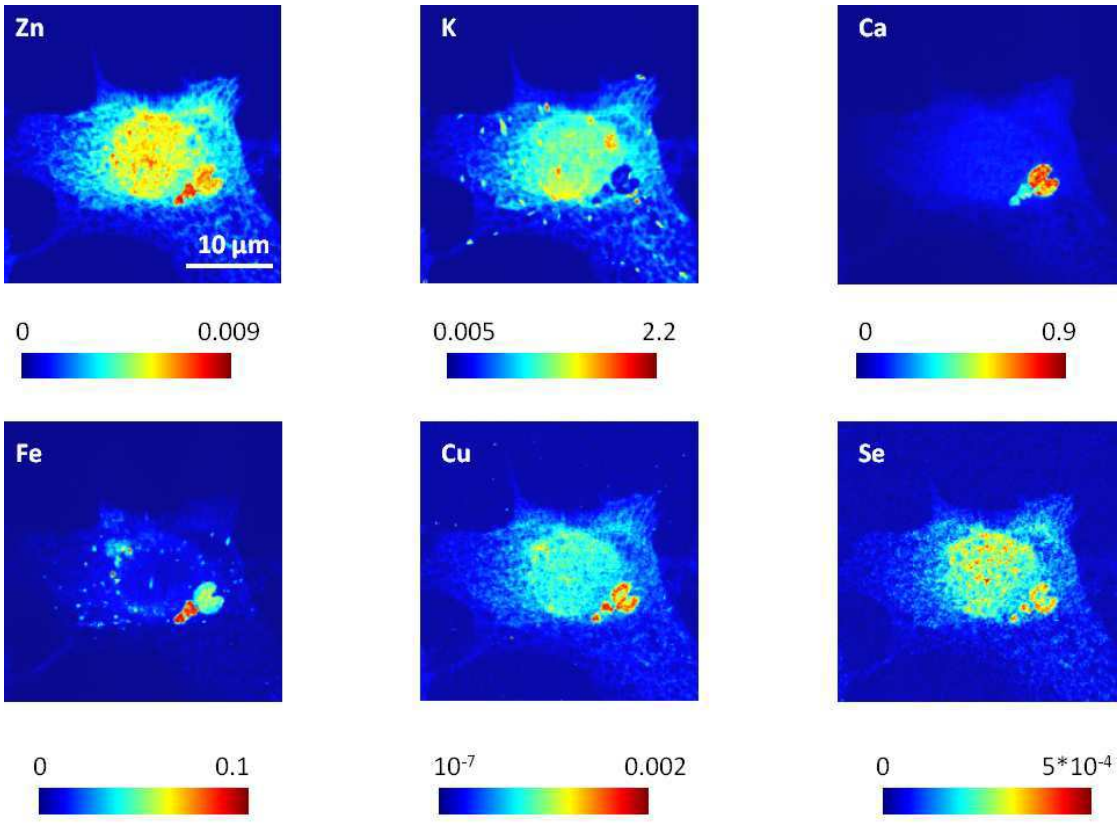

Figure 7.5: X-ray fluorescence maps of several elements from a single PC12 cell. Color scale bar indicates minimum and maximum areal mass of a given element in the sample (in μg/cm^2). The colors are scaled to the maximum of each map. Scanning size was 200x201 pixels.

Figure 7.5 presents the results of the fluorescence scan of one PC12 cell: the elemental distribution (areal mass) of six relevant elements are shown. The step size was chosen to be 150 nm and the dwell time 100 ms. Based on the phase contrast images (Fig. 7.6), it is possible to evaluate the cellular shrinkage or mass loss due to XRF analysis. From the images as well as from the profile plot it is easily visible that the area of the cell is smaller after the XRF scan. The size of an irradiated cell along the white line is about 100 pixels smaller than before the XRF scan; this makes a difference of about 5 μm (see the pixel sizes in Tab. 7.4). This shrinkage seems to be smaller in the horizontal direction (so along the fast scanning axis) compared to the vertical one. The difference in the overall area of the cell is 29%. The differences in the cell structure

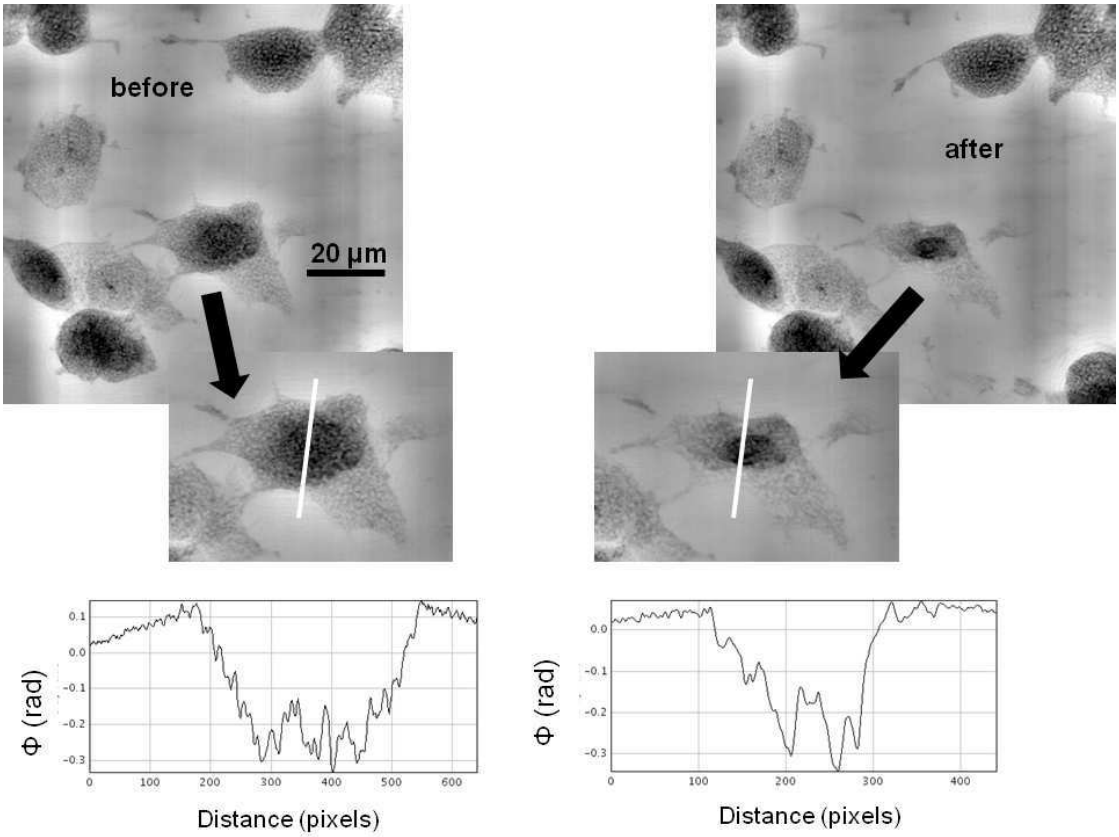

Figure 7.6: Phase contrast images of the PC12 cell presented in Fig.7.5. Left images correspond to data taken before fluorescence scan while the right ones were acquired after fluorescence scan. White line along the cell indicates an area taken for a measurement of structure differences shown on profile plots.

are also visible on the surface plots (Fig. 7.7). We have recently demonstrated that the projected phase (Φ) can be translated into the areal mass density (g/cm^2), which can be used to normalize the XRF elemental map (μg/cm^2) to obtain true elemental quantification at sub-cellular scale (Chapter 6),[72]. The results obtained for the cell (along the white line, see Fig.7.6) before and after the XRF scan are as follows: 950 μg/cm^2 and 750 μg/cm^2, which makes a difference of 21%. We obtained similar results of about 20% decrease of the projected mass (in a certain area) and of the area for different cells (see 7.2) which were imaged in the same conditions. The fact that also the projected mass decreases shows that the cell mass does not collapse but evaporates. From comparing just the cell dimensions one would suspect the cell shrinking but the difference in the projected mass gives a clear answer to the problem: the structure of the cell changes but this process comes together with a mass loss. By integrating the areal mass density over the total area of the cell, it is possible to estimate the total mass loss. It reaches up to 54%. The dimensional difference between the first phase contrast image (i.e. the intact cell) and the XRF image is 14%, whereas this difference increases to 26% between the XRF image and the second phase contrast image (i.e. the irradiated cell). This means that the fluorescence image is still more similar to the intact cell than to the irradiated cell. It could indicate that the damage propagates not as rapidly as data are acquired. This supports the opinion that data obtained through SR-XRF are reliable to determine sub-cellular elemental concentrations, even at the very high flux density (10^8 ph/s/nm^2) used in this study. The proposed dose efficient phase contrast method does not damage the cell and allows to go a step further in XRF quantitative analysis. The determination of the initial projected mass works as a reference to correct for mass loss observed during analysis. Figure 7.8 compares a STIM image and the corresponding part of the phase contrast image of the cell previously scanned in the fluorescence mode. In order to better distinguish the cell and background structural differences, the contrast was enhanced. Therefore some areas are saturated and can not be compared between the two images. On both images squares burnt out during the XRF scan are visible. Both techniques are sensitive enough to evaluate the changes in the polycarbonate foil quantitatively. From the phase map we can calculate a maximum difference of 29 μg/cm^2 at the border of the irradiated and non-irradiated areas. The same difference can also be calculated from the STIM image, it gives about 7 μg/cm^2.

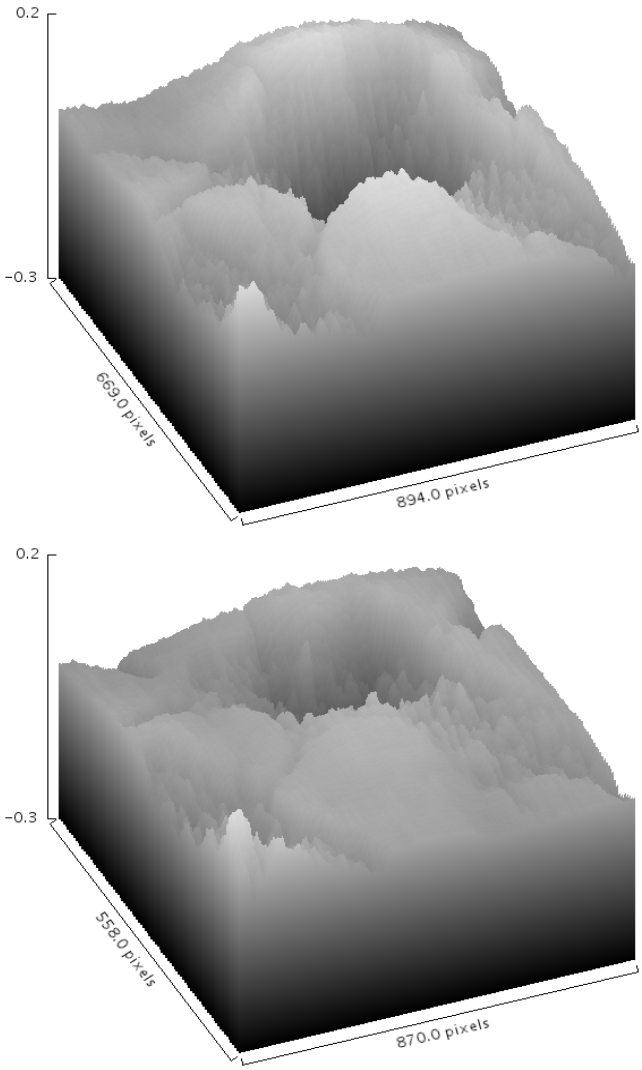

Figure 7.7: Surface plot of the non-irradiated cell (up) and irradiated one (bottom).

7.3.2 Dose

Following the equation

$$D = \frac{\mu}{\rho} \cdot \frac{flux \cdot t_{pixel}}{s_{pixel}} \cdot E[J] \tag{7.1}$$

it is possible to evaluate the dose D delivered during the XRF scan. In the equation μ/ρ [cm^2/g] is the absorption coefficient divided by the density, t_{pixel} is the dwell time per pixel, s_{pixel} is the surface of one pixel and E is the energy of the beam (in J).

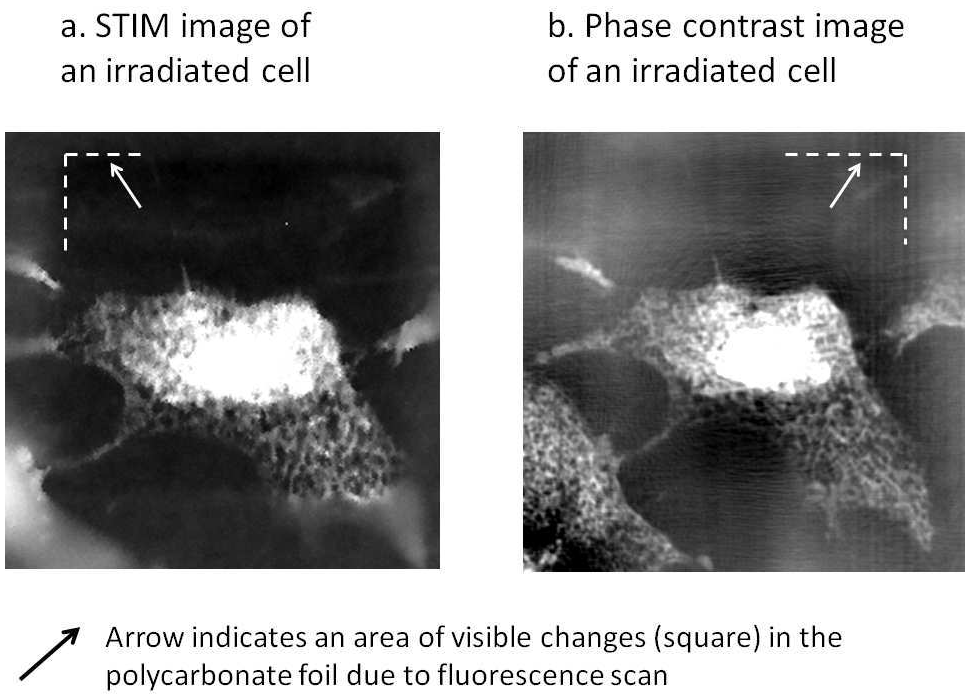

Figure 7.8: Indirect comparison between STIM (a) and phase contrast image (b) of the irradiated cell. Dashed white line indicates the square burnt out during the fluorescence scan. For better comparison the contrast was enhanced and does not represent the full range of the images. Scales of the images are slightly different, the width of the phase image is 47 μm.

For the evaluation of the dose delivered during the phase contrast imaging one has to consider the characteristics of the detector as well as the configuration of the experimental setup such as distance focus-detector and focus-sample. Also the dose delivered to the cell during STIM measurement can be evaluated. The numbers are presented in the Tab. 7.4. STIM has been demonstrated to be a non-damaging method advised for accurate measurement of the initial sample areal mass density [73]. On the contrary, the irradiation required for PIXE micro-analysis of a freeze-dried single cell is more intense and the acquisition of an elemental map can take several hours. This prolonged irradiation alters the sample integrity. The resulting organic mass loss remains the major limitation in the normalization of X-ray fluorescence yields for accurate quantitative micro-analysis at the sub-cellular level. This limitation is overcome by combining

	Dose (Gy)	Time	Pixel size (nm)
fluorescence	9×10^8	several hours	150
phase contrast	3×10^3	few minutes	50
STIM	8×10^2	about 0.5 h	250

Table 7.4: Dose delivered to the cell during different experiments and time of acquiring data

on the one hand PIXE and particle backscattering spectrometry measured simultaneously; and on the other hand STIM to enable absolute quantitative imaging. A 20% to 30% loss of the organic mass for freeze-dried biological samples has been reported under PIXE irradiation but at much lower resolution of 2μm [50], [74] while our results indicate similar mass loss but at spatial resolution 13 times higher (0.15 μm). This is inline with known less destructive characteristics of X-ray photons when compared to electron or ion beams. Indeed, when micro-PIXE and micro-SR-XRF are compared, PIXE is found to cause more damage. Blackening of the sample scanned area is often observed at high current [75]. In [76] authors reported that a dose below 10^7 Gy should be used to avoid damage to dehydrated biological samples using electron or soft X-ray microscopy while at such dose a 50 % mass loss in a polymethyl methacrylate was reported [77]. Our results show significant mass loss at a dose of 9×10^8 Gy. This may be explained by a mass loss that can be sample dependent (chemical composition and physical state). Also, the rate of water molecule that can be trapped at the sample surface can be different between an irradiation in air as done for SR-XRF and PIXE or soft X-ray microscopy analysis that are performed under vacuum. The surface volatilization of light elements (H, C, N, O) of the matrix and also of sulphur has been demonstrated [78] and is in agreement with our above observations. Hydrogen loss is the main contribution to this effect as shown by PIXE studies [78] or more recently by a study on the radiation damage in X-ray crystallography at cryogenic temperature [79]. Our XRF analysis records the content of the heavier elements. Thus this also explains why the fluorescence map is more similar to the intact cell than to the irradiated one.

7.4 Conclusions

We presented here full-field phase contrast imaging as a fast and low dose technique to evaluate the radiation effects of sub-cellular X-ray fluorescence analysis. Based on the calculation of the cell projected mass before and after XRF analysis - the answer on how radiation affects a cell is unequivocal: the structure of the cell is changing isotropically and mass loss clearly occurs. As the acquisition time for XRF experiments is longer than the one for phase contrast or STIM experiments, also the dose delivered during the measurement is higher (Tab.7.4). This is the price one has to pay in order to obtain the elemental maps of the sample and to probe the atomic composition in sub-100 nm cellular areas. Still we demonstrated that the XRF image is very close to phase contrast image prior analysis. The proposed method is to our knowledge the unique X-ray method demonstrated to be able to monitor mass loss after SR-XRF mapping. It allows correction for true quantitative elemental concentration maps at sub-cellular scale while keeping extremely low detection limit in the range of thousand of zinc atoms. The results were obtained on cryofixed and freeze-dried cells of PC12 cell lines, but the method can be applied to other cell lines as well. The effects of the intense irradiation for SR-XRF analysis may be greatly reduced by using cryogenic sample preservation during the fluorescence acquisition. This encourages the development of a SR-XRF cryo-scanning nanoprobe that will allow 2D and 3D analysis of frozen hydrated cells [80]. The proposed method is thus invaluable for 3D elemental imaging for which the acquisition time will be an order of magnitude longer than for 2D scans with concomitant increase in radiation damage to be accounted for. Another possibility to reduce radiation damage would be shortening of the exposure time. However this needs to be compensated by an increased detection efficiency in order to preserve the low detection limits and high signal to noise ratio. Finally more efficient acquisition schemes and data analysis [81] are another way to deal with radiation effects.

7.5 Acknowledgements

We thank the European Synchrotron Radiation Facility for providing the beamtime. This work was supported in part by the ANR Program PIRIBIO (ANR-09-PIRI-0029-

01).

Résumé du Chapitre 7 en Français

Dans ce chapitre, nous commençons par un bref rappel sur l'origine des dommages induits dans les structures biologiques par les rayonnements ionisants et sur les aspects de doses. La problématique des dommages radiatifs en fluorescence X excitée par rayonnement synchrotron est brièvement abordée; ce problème étant que rarement étudié hormis quelques études réalises en microscopie à rayons X à très bassesénergies ou plus récemment en cristallographie de protéines. Notre travail a porté sur la nanoimagerie à rayons X de hautes énergies (rayons X $>$ 15 keV) pour lequel on ne retrouve pas, à notre connaissance, d'études de l'influence des dommages radiatifs sur des cellules analysées par une nanosonde par fluorescence X excitée par le rayonnement synchrotron. Nous avons utilisé à nouveau le modèle de cellules PC12. Afin d'appréhender les effets sur les cellules de l'analyse par le très haut flux de photons X, celles-ci ont été imagées par contraste de phase avant et après l'analyse par fluorescence X. Les images de phase de cellules obtenue après l'analyse par fluorescence X ont été comparées avec la technique d'imagerie par microscopie ionique en transmission et à balayage (STIM). Nous avons ainsi pu confirmer que les images de fluorescence X de cellules PC12 analysées par un très haut fluxs de photons X issus de la nanosonde synchrotron sont assez similaires aux cellules avant leur analyse. En revanche, une fois l'analyse par la nanosonde X terminée, on note une réduction de la surface de la cellule ainsi qu'une perte de masse surfacique (20%) révélée par l'analyse des images en contraste de phase. Nous avons pu conclure à une rétractation des structures cellulaires accompagnée d'une volatilisation des éléments du fait de l'irradiation lors de l'analyse par fluorescence X. La progression de l'endommagement semble rester plus lente que la vitesse d'analyse. La perte de masse due à la volatilisation d'éléments légers (C, H, O, N) de la matrice cellulaire peut être corrigée par l'imagerie X par contraste de phase rendant plus précise l'analyse

quantitative de la composition chimique cellulaire. La technique d'imagerie X par contraste de phase est très rapide entrainant un dépôt de dose comparable à une analyse STIM et assurant une préservation de l'intégrité des structures des cellules imagées. Cette technique qui dans notre cas s'est limitée à 2 dimensions constitue donc un outil permettant de rendre compte des dommages induits par les hauts flux de rayons X et sera précieuse pour en corriger les effets lors de futures analyses tomographiques de cellules entières lyophilisées ou congelées hydratées.

Chapter 8

Intracellular distribution of nanoparticles

8.1 Introduction

A nanoparticle is a small object that behaves as a whole unit in terms of its transport and properties. Their size can vary between 100 and 2500 nm for fine particles or between 1 and 100 nm for ultrafine particles. Nanoparticle research is currently the most studied branch of science with an increasing use of nanoparticles in various fields. The particles have wide variety of potential applications in biomedical, optical and electronic fields. However increased use of nanoparticles in every day products is associated with possible health risks. Interaction with tissue and cells differs from normal particles. This has to be taken into account as well.
In the case of future biological and medical applications they:

- create fluorescent biological labels for important biological markers and molecules in research and diagnosis of diseases
- deliver drugs and genes for gene therapy
- probe DNA structure
- detect proteins

- are used in genetic and tissue engineering
- are used to enhance the dose-effect of radiation therapy

and more.
Noble metal nanoparticles (NPs) provide a unique nanosized scaffold on which to assemble metal or chemical complexes. They occupy a niche between the atomic and bulk metal scales, displaying unique properties to enable the interface of biological processes with technological advances in the nanoregime [82]. Gold NPs and platinum NPs have also recently emerged as attractive candidates for the delivery of therapeutic payloads [83], [84]. The noble metal cores are chemically inert and nontoxic and the therapeutic payloads, including small drug molecules and/or large biomolecules (e.g., plasmid DNA or proteins for gene and protein therapy and targeting applications), can be attached via thiol linkages [85] yielding stable nanovectors. In the present work we were collaborating with Professor Kysela group (Genome Stability and DNA Repair Group, University of Birmingham) who is actively pursuing development of nanovectors with multiple functionalities for cancer therapy. Inevitably, the proposed multifunctionality comes at the expense of added complexity and the higher risk of adverse biological reactions. With the aim of being able to manipulate DNA damage responses in cells following the therapeutic intervention, the most desirable target is the nucleus. This is because the dose-enhancement of ionizing radiation by high-atomic number materials such as gold and platinum is dependent on the close proximity to the DNA due to short predicted distances travelled by the secondary electrons responsible for the effects [86]. The local inhibition of DNA repair mechanisms close to the site of DNA damage is also likely to have a much more pronounced effect on the cell survival. Targeted nuclear delivery is a challenging problem, but Prof. Kysela has designed and developed a universal model - tripartite synthetic peptide construct, that gives the functionalized nanovectors the ability to:

- translocate to the cell nucleus
- inhibit the DNA damage/repair responses in the targeted cells
- increase the sensitivity of targeted cells to therapeutical radiation

This unique strategy was based on fusion of the CALNN peptide, viral nuclear targeting peptide and single DNA repair inhibitory peptide. In addition, they have demonstrated that targeting functionalized nanoparticles radiosensitize cells by inhibiting DNA double strand break (DSB) repair, resulting in chromosomal aberrations. These nanoconstructs are under patent and no details can be given in this manuscript. In this work they appear as peptide A1 and peptide A3.
X-ray fluorescence allows to study "natural" elemental concentration in biological samples but it started to be a critically important technique in bionanotechnology due to the possibility to study artificial elements deliberately introduced into tissues and single cells, for example through functionalized nanoparticles [87]. In fact, X-ray fluorescence allows to measure the intracellular distribution of such nanoparticles, which can complement more traditional tools like optical fluorescence microscopy, electron microscopy, scanning electrochemical microscopy or atomic force microscopy. The main advantage of using gold or platinum particles is that they are xenobiotic elements, so that the signal from the nanoparticles cannot be confused with that from "natural" biological material. On the other hand, Au or Pt Lα1 emission line is in close proximity to the Zn K emission lines, so that a spectral deconvolution is required to reach acceptable signal specificity. In this study, we explore the capabilities to use X-ray fluorescence to inform on the distribution and the number of nanoparticles targeting MRC5VA normal human epithelial lung fibroblasts as in vitro model that we already used in a previous work [84].

8.2 X-ray fluorescence analysis

MRC5VA normal human epithelial lung fibroblasts were maintained in Dulbeccos modified Eagles medium supplemented with 10% fetal calf serum (FCS), 3.0 mM l-lutamine, nonessential amino acids and 1% sodium pyruvate without antibiotics. The cells were grown to near confluence (92-98% of cells in G1 phase of the cell cycle as verified by flow cytometry) and then subcultured on sterile $Si_3N_4$4 membranes (500 nm thick, Silson, UK) with a density of 10^5 cells/target in a complete medium as described above. Cells were incubated with non-targeting nanoparticles (i.e without peptides) and specifically cell-targeting lanthanide- coated AuNPs and PtNPs (2.8 nM, 24h) with or without Fugene (3 l). Fugene is a lipid-based reagent that allows transient transfection of cells

and thus results in an easier intracellular delivery of nanoparticles whether specifically cell targeted or not. Following incubation the targets were rinsed three times with phosphate buffer solution (PBS), then fixed for 30 min at room temperature in 2% paraformaldehyde buffer solution (pH 7.2), rinsed 2 times with PBS and quickly rinsed in a ultrapure water solution to remove remaining salts. Further, the samples were dry overnight under a laminar flow cabinet.

The XRF imaging was performed as described in 5.2.1. The energy of the beam was set to 17 keV. The fluorescence maps of diverse cells are presented on the Fig. 8.1. It is visible that there are almost no nanoparticles inside the cell (a. and d.) as these are control cells (no fugene, no targeting peptide). On the opposite, in the pictures b. and c. the signal from nanoparticles is clearly visible. Cell b. was treated with fugene as well as with peptide-based (A1) Au nanoparticles while cell c. was treated only with peptide-based Au nanoparticles and of a different kind of peptide (A3) than cell b. Although cell c. was not treated with fugene it still gives a signal of Au. The signal from Pt nanoparticles is visible in the cells e. and f. They were both treated with peptide of the same kind (A1) but only cell f. was in addition treated with fugene. When comparing both cells, it can be seen that there were more clusters of nanoparticles inside the cell f. (with fugene) than inside the cell e. (without fugene). The zinc distribution gives the rough boundary of the cell with a higher content in the cell nucleus thus enables to delineate it. Therefore, from the cells imaged (N=5), we see that in the presence of the artificial opening of the membrane (fugene treatment) and whether peptide-based Nps are used or not; we have a large distribution of NPs inside the cell. The NPs are not only located at cell nucleus location. In physiological condition (without fugene) we see that the NPs distribution is very discrete with NPs localised at both cytosolic and nuclear sites.

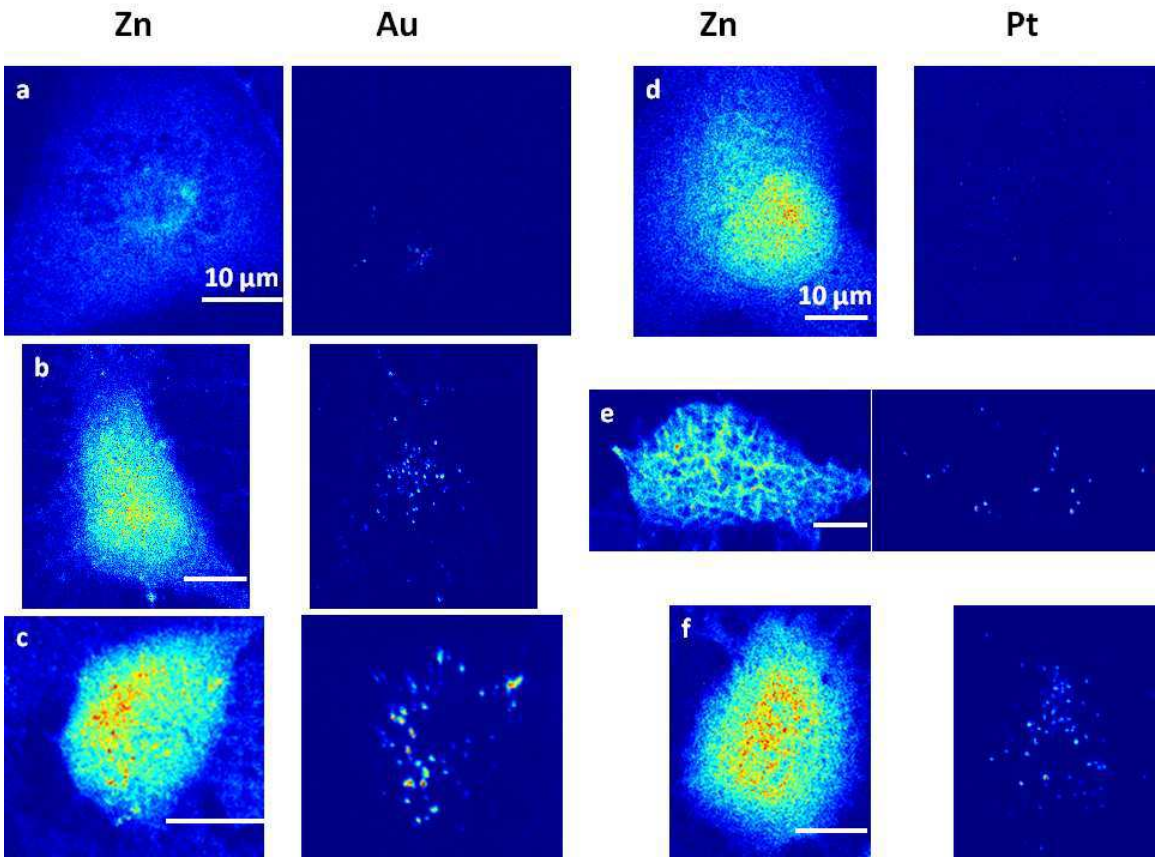

Figure 8.1: Zn, Au and Pt X-ray fluorescence maps of diverse MRC5VA normal human epithelial lung fibroblasts: a. without fugene and without targeting peptide; b. with fugene and with targeting peptide A1; c. without fugene and with targeting peptide A3; d. without fugene and without targeting peptide; e. without fugene and with targeting peptide A1; f. with fugene and with targeting peptide A1. The scale bar on every picture represents 10 μm. The colors are scaled to the maximum of each map.

8.3 Nanoparticles estimation

The first observations have been made in the previous section, based just on the X-ray fluorescence maps. It was clearly visible that Au or Pt signal in control samples was much smaller than in the treated samples. In fact to better quantify the nanoparticle/cell infiltration one would like to estimate the number of nanoparticles and their mass inside the scanned objects. The estimation was made using ImageJ software and

its built in package 'Analyze particles'. Firstly correct scales were set in every studied map, from pixel scale into nanometer scale. Then images were converted into grey scale and thresholded (automatic thresholding function in ImageJ [88]). The automated routine 'Analyze Particles' was used and the results displayed on the screen. One of them is an actual image of labeled particles (Fig.8.2c). Every cluster has his

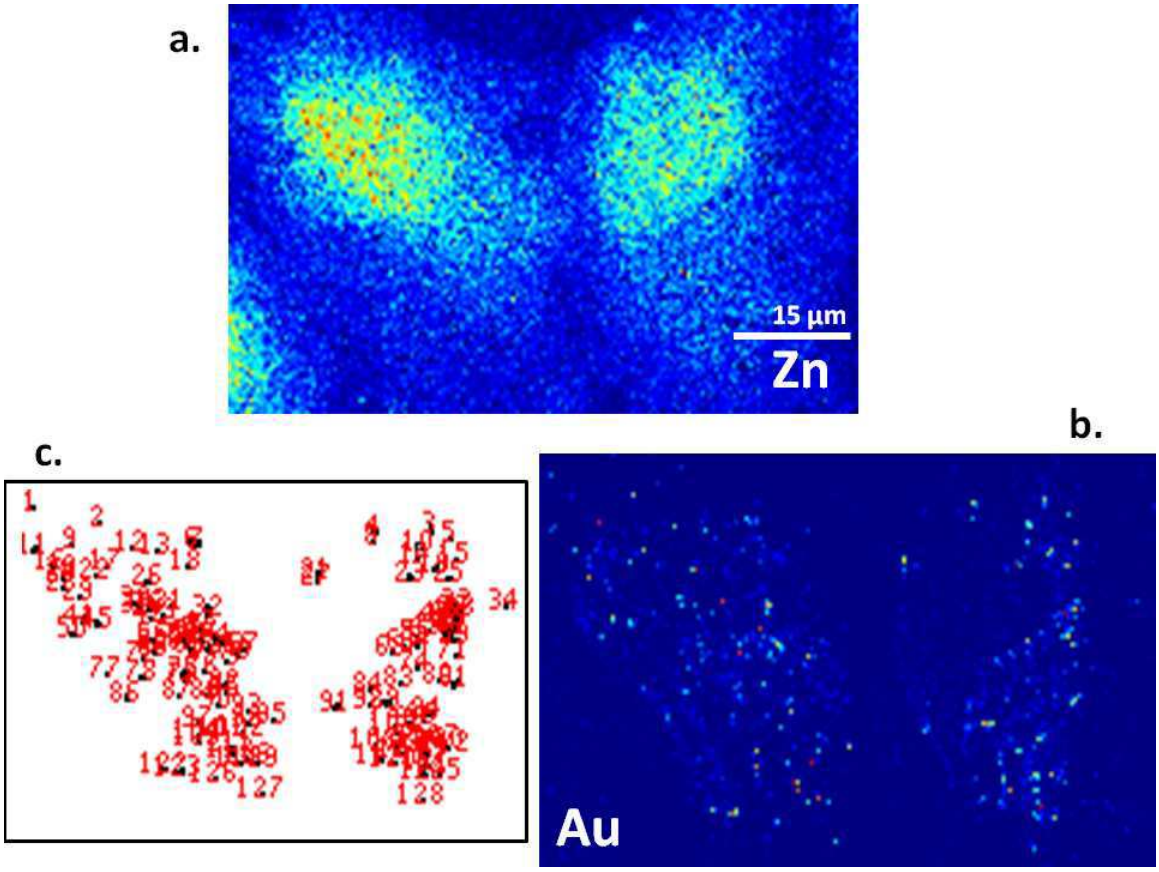

Figure 8.2: The picture shows Zn (a.) and Au (b.) distribution in the cells treated with a targeting peptide (A3) but not with a fugene. The nanoclusters of gold are found and labeled (c.)

area (in nm^2) and weight. The weight of Au or Pt is found based on combination of the binary image (result of the threshold procedure) and the fluorescence map in units of $\mu g/cm^2$; the comparison is within the 'Set measurements' routine where the sum of the areal mass of a given element integrated over the cluster area provides the weight. We can estimate that every calculated hereafter number is biased by 5% (uncertainty

coming from the fit used during batch fitting in PyMCA). In order to calculate the number of nanoparticles a simple model is chosen. As the nanoparticles are of round shape with a known diameter (13nm for Au and 6nm for Pt) and of a structure in which the core metal (Au or Pt) dominates thus they can be considered as spheres of pure metal; the peptide grafted to NPs has no effect on this calculation based on X-ray fluorescence signal. In this case the volume as well as the density are known, so the mass is known as well (m=Vρ). Mass of every found cluster was divided by the mass of single nanoparticle (Au: 2.2×10^{-17}g, Pt: 2.4×10^{-18}g) which gives the number of nanoparticles in a cluster. The list of all the clusters found in the cells from Fig.8.2 are shown on the Fig.8.3. It gives an average value of 109 nanoparticles per cluster, with some few clusters of significantly higher amount of nanoparticles. The above calculations can be performed as well for the cells presented on the Fig. 8.1 in order to get some additional information to the spatial distribution of Au and Pt signal that is representative of the intracellular NPs location. Apart from accessing the number of nanoparticles per cluster additional plot presenting the number of nanoparticles versus the projected area of the cluster was made (Fig.8.4 for Au samples and Fig.8.5 for Pt samples). It shows rather linear dependence for Au sample without fugene (cell c. on the Fig.8.1) as well as with fugene (cell b. on the Fig.8.1). In the sample without fugene the amount of clusters of small area and small number of nanoparticles inside them is significantly higher than the amount of large and "rich in nanoparticles" clusters. For example in total there are only 2.5% of clusters with projected area bigger or equal to $1\mu m^2$ in a sample without fugene and 9.3% in a sample with fugene. When studying Fig.8.5, the first significant observation is that the amount of clusters with Pt nanoparticles is smaller than the amount of clusters with Au nanoparticles, shown on previous picture. The amount of clusters containing Pt together with fugene (cell f. on the Fig.8.1) is 3 times higher than the amount of clusters of nanoparticles without fugene (cell e. on the Fig.8.1). But what should be noticed is that even if the amount of clusters is lower for the 'no fugene' sample, they are containing more nanoparticles than sample with fugene. For example in total there are 45% of clusters containing 1000 and more nanoparticles in a sample without fugene, while only not even 11% for the sample with fugene. To remind they were both treated with the same kind of peptide (A1). The total mass of gold and platinum can be compared as well (Fig. 8.6), without going into details of how many nanoparticles are included in clusters. For this comparison again the cells from previous figures were used (cells b., c., e., f.),

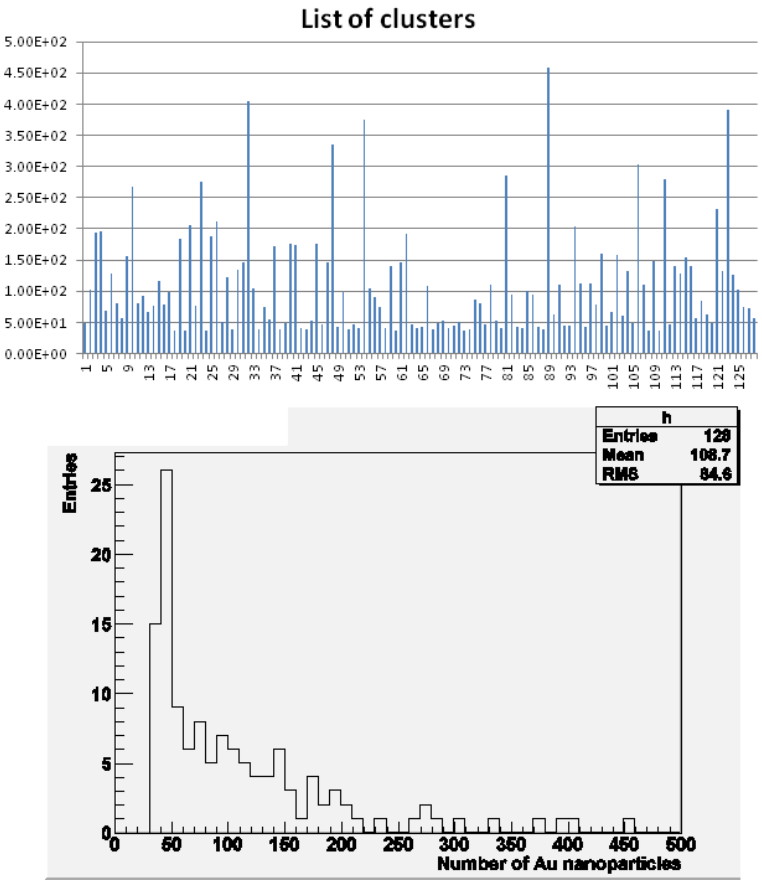

Figure 8.3: Upper picture lists the clusters and their content - the number of nanoparticles. They were calculated from the X-ray fluorescence map on Fig.8.2. Lower picture shows a histogram made from the number of nanoparticles per cluster.

the control cells are excluded due to threshold. We can observe no big difference in total mass of Pt between cell containing fugene (Pt wf) and the one without fugene (Pt wof). On the contrary the difference in total mass of Au between cell containing fugene (Au wf) and the one without fugene (Au wof) is significant. Also the total mass of acumulated gold in a cell treated with fugene is higher than the total mass of accumulated platinum in any case. To remind the mass of one nanoparticle including gold is bigger than the mass of one nanoparticle including platinum. Of course the cells are different, they have different sizes, they could have different thicknesses which on fluorescence map would never be visible. The findings presented here provide a first insight into the intracellular distribution of nanoparticles. They are far from estab-

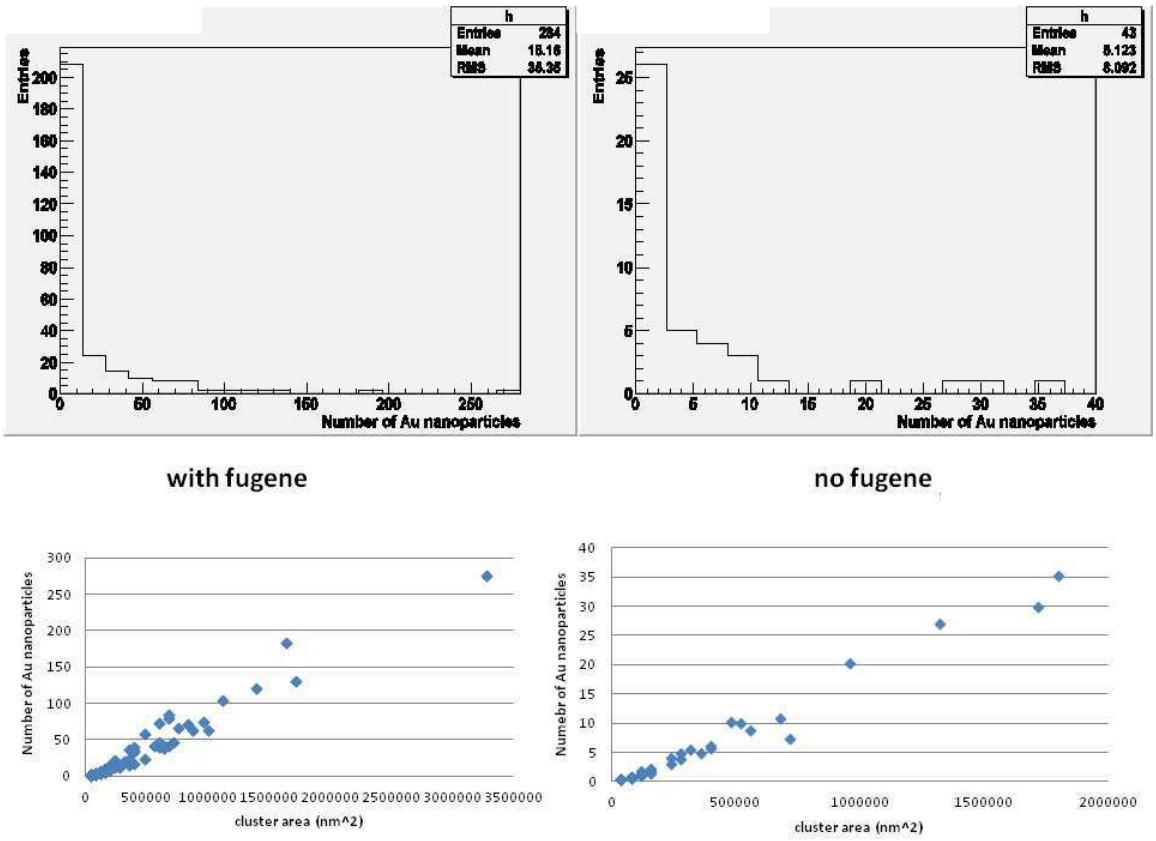

Figure 8.4: Comparison between cell b. with fugene and cell c. without fugene from the Fig.8.1. Upper pictures present histograms made of number of nanoparticles in a cluster, lower pictures present distributions of number of Au nanoparticles per cluster area.

lishing final conclusions as a more significant number of cells should be analysed to be conclusive. Nevertheless synchrotron-based X-ray fluorescence nanoprobe is clearly of help to evaluate NPs with dedicated cellular targeting strategy and is useful to refine these strategies before larger experiment can be drawn. Besides, the fact that cells are different should especially be taken into consideration. Studying the graph from Fig. 8.6 one could claim that especially gold is likely to be highly accumulated in cells treated with fugene. But there is one question not to be left without the answer: how big/thick/heavy is the cell? The answer could be provided using a combination of fluorescence maps with phase maps of the same cell. Then the graph would show the

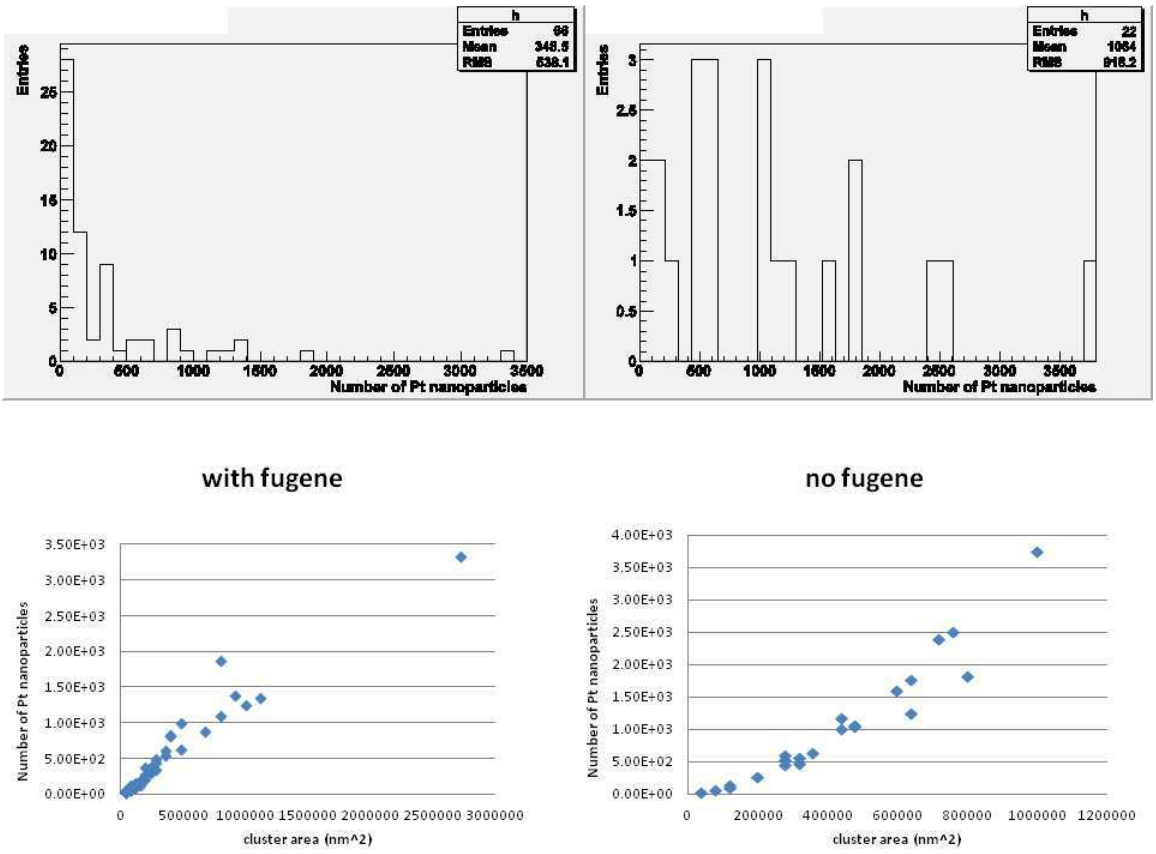

Figure 8.5: Comparison between cell f. with fugene and cell e. without fugene from the Fig.8.1. Upper pictures present histograms made of number of nanoparticles in a cluster, lower pictures present distributions of number of Pt nanoparticles per cluster area.

relative mass of a certain element (the total mass of gold or platinum divided by the mass of a cell). This would bring more accurate results and perhaps also the explanation why the cell b. accumulated the most of gold nanoparticles - much more than the cell c. (without fugene) but also more than cell f. (which was treated with fugene and that accumulated platinum). In this case estimating the mass of a cell by applying some standard average density is worthless. It would just create new uncertainties resulting in a final value far from the truth. Nevertheless these findings provide the tools for an accurate evaluation of the location, the amount and the clustering of different types of NPs inside whole cells. This will be useful for future investigations in this

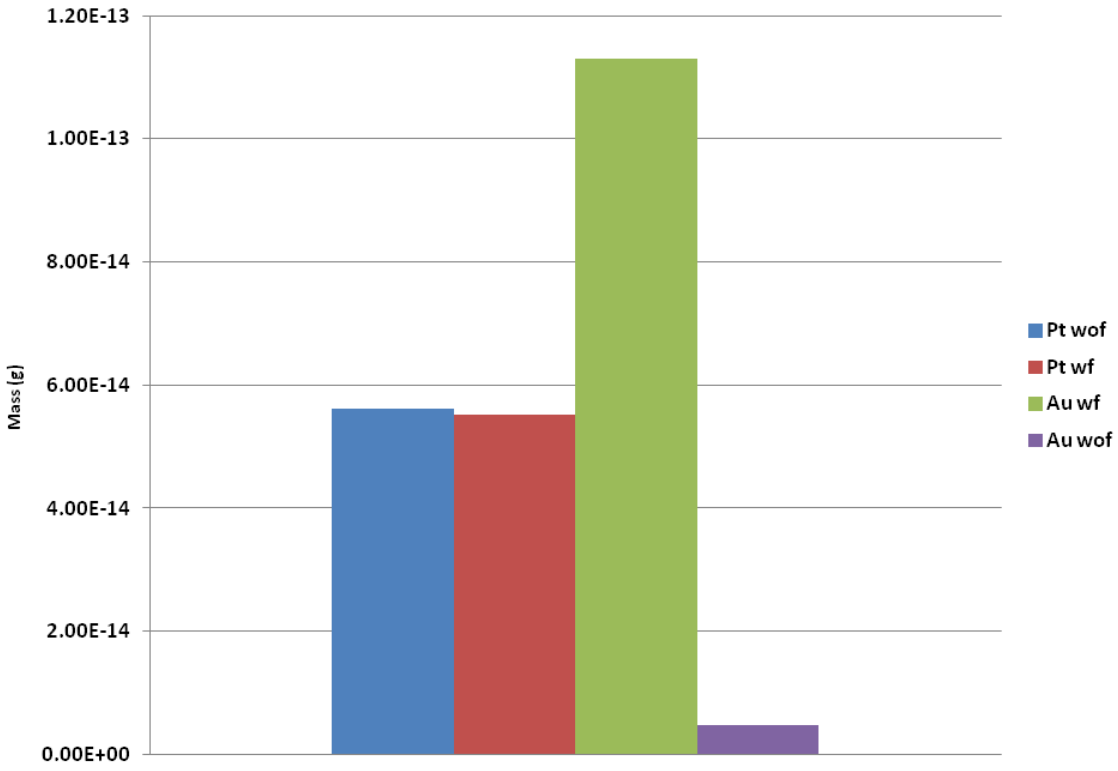

Figure 8.6: Graph shows the total mass of gold and platinum per investigated cell whether with fugene (Au wf, Pt wf) or without fugene (Au wof, Pt wof) from the Fig.8.1.

research area.

Résumé en Français

Ce chapitre est une contribution à un travail collaboratif avec le laboratoire du Dr B. Kysela (Université de Birmingham) qui développe de nouveaux types de nanoparticules couplées à des peptides ayant pour but de cibler le noyau cellulaire des cellules tumorales et aussi d'inhiber une des voies de réparation de l'ADN. Les nanoparticules sont de type métallique (or ou platine). Pour la radiothérapie par rayons X notamment elles permettent une exaltation de la dose d'irradiation mais également la production d'électrons secondaires qui dégradent les molécules environnantes. Pour cibler l'ADN les nanoparticules devront se trouver au sein du noyau cellulaire. Dans un premier temps, cette nouvelle stratégie a été testée sur un modèle cellulaire de fibroblastes pulmonaires embryonnaires immortalisés MRC5VA. Les cellules analysées ont été incubées avec des nanoparticules d'or ou de platine couplées à différent types de peptide (brevet en cours) et ont été ou non exposées à un réactif de transfection (fugene) qui transitoirement permet l'ouverture de pores membranaires et ainsi artificiellement l'entrée des nanoparticules. L'analyse par fluorescence X de la distribution intracellulaire des nanoparticules d'or ou de platine testées montre que lors de l'exposition à l'agent de transfection, nous obtenons une large répartition cytosolique des nanoparticules retrouvées en très grand nombre. Pour les cellules non-exposées on a une distribution de nanoparticules beaucoup plus faible et vraisemblablement localisées plus au niveau du noyau cellulaire. Bien entendu, la cartographie chimique 2D de cellules représente la projection du volume cellulaire et il reste donc difficile de certifier la localisation intranucléaire de ces nanoparticules. Les cartes de fluorescence X ont été exploitées afin d'estimer le nombre de nanoparticules au sein des cellules. Nous avons ainsi pu déduire par l'analyse quantitative des images de fluorescence X des informations sur le nombre de nanoparticules et la distribution en taille des clusters de nanoparticules au sein des cellules MRC5VA analysées. Il est intéressant que le nombre de nanoparticules de platine par exemple soit plus important dans les cellules non-exposées au fugene même si toutefois dans ces dernières le nombre de cluster est 3 fois plus faible que pour les cellules exposées au fugene. Les résultats ne permettent pas de statuer sur le type de nanoparticules qui cibleraient le mieux et en grande quantité le noyau cellulaire. Toutefois nous avons mis à disposition les outils d'analyse nécessaires et des expériences sur un plus grand nombre de cellules, auxquelles l'imagerie X par contraste de phase serait menées en parallèle, permettront surement de préciser plus finement

ces aspects quantitatifs sur le nombre de nanoparticules intracellulaires.

Chapter 9

Summary and perspectives/Resumé en Français

This work presents some recent developments in the field of hard X-ray imaging applied to biomedical research. As the discipline is evolving quickly, new questions appear and the list of needs becomes bigger. Some of them are dealt with in this manuscript.
It has been shown that the ID22NI beamline of the ESRF can serve as a proper experimental setup to investigate diverse aspects of cellular research. Together with its high spatial resolution, high flux and high energy range the experimental setup provides bigger field of view, is less sensitive to radiation damages (while taking phase contrast images) and suits well chemical analysis with emphasis on endegeneous metals (Zn, Fe, Mn) but also with a possibility for for exogoneous one's like these found in nanoparticles (Au, Pt, Ag) study.
Two synchrotron-based imaging techniques, fluorescence and phase contrast imaging were used in this research project. They were correlated with each other on a number of biological cases, from bacteria E.coli to various cells (HEK 293, PC12, MRC5VA, red blood cells).
The possibilities of the two techniques were explored in Chapter 5. Not yet in a fully quantitative way but compared together with a non-synchrotron technique, such as AFM, they proved their accuracy for sub-cellular investigations. The example on bacteria E.coli, which are very small objects, teases the capabilities of the existing nano-imaging end station. Although the phase map of bacterium could not reveal any

internal structures, but still once compared with the AFM image gave a satisfactory result. The explorations made in this chapter allowed preparation of more established and detailed analysis, described in the next chapter where both techniques, X-ray fluorescence and phase contrast imaging, were exploited in order to access absolute metal projected mass fraction in a whole cell. The final image presents for the first time true quantitative information at the sub-cellular level, not biased by the cell thickness. Thus for the first time a fluorescence map serves as a complete quantitative image of a cell without any risk of misinterpretation. Once both maps are divided by each other pixel by pixel (fluorescence map divided by the phase map) they present a complete and final result of the metal (Zn in this work) projected mass fraction in ppm of dry weight. For the purpose of this calculation the analysis was extended to calibration (non-biological) samples. Polystyrene spheres of a known diameter and known density worked very well here and allowed validation of the presented method. Different images (phase map, AFM, STIM) and profiles were compared and statement on the high accuracy of phase contrast imaging for the thickness/structures determination was made. The result on true metal projected mass fraction represents a first step to an absolute sub-cellular analysis and certainly can be improved to even closer reflect on reality. All the measurements were taken on freeze-dried cells. Thus the result is in ppm of dry weight. In fact the measurement would have even deeper meaning if it was made on hydrated cells. For the moment this is not possible with the existing setup of the ID22NI beamline but will be possible in the future with a new beamline devoted to nano science - NINA (Nano-Imaging and Nano-Analysis). The new beamline will be furnished with a cryostage and X-ray imaging will be made on frozen-hydrated samples. Nevertheless the analysis presented in this manuscript is of undeniable importance to both the biomedical community and to the ESRF team engaged in the NINA development. The measurements taken for the purpose of this analysis can be as well made in a tomography mode. In this case the result would provide the full concentration of a certain element in a cell and not only the projected one. Some data has been already collected in the course of this PhD work, but they are not discussed in this manuscript. To answer the problems of cell irradiation both imaging techniques were exploited again. Repeating the phase contrast imaging after the fluorescence scanning allowed to show the changes induced by radiation damage during X-ray fluorescence scan. The changes were not only clearly visible but could be as well quantified. Together with the numerical evaluation of damages, the dose delivered to a cell during the experiment

was calculated as well. To complete the picture, a different non synchrotron-based imaging technique, STIM, was used and compared. It is the first time that phase contrast imaging is used to monitor radiation damage effects during X-ray fluorescence microscopy experiments. This type of monitoring is crucial to ensure the integrity and quantitativeness of the results. It was shown that, due to the irradiation, the cell shrinks and looses a significant part of its mass. The quantitative approach revealed the actual phenomenon, to be distinguished from the collapse of the cell. As well as for the absolute mass fraction determination, the experiments were made on freeze-dried cells which are more resistant to radiation than hydrated ones. Again the analysis on radiation effects can certainly be repeated on the future beamline NINA with the use of a cryostage. Another step, apart from working on frozen-hydrated cells, would be monitoring the structural damages in 3D (during a fluorescence tomography scan). In fact some data on malaria infected red blood cells (collaboration with Prof.Biot, Université de Lille) were recorded and first, preliminary results show that irradiation of the sample has certainly to be taken into account. This is clearly understandable since the tomography scans take much more time than 2D scanning. During this time the sample stays permanently in the X-ray focus and the amount of damage is huge without doubt. This topic will have to be investigated in detail in the future. Significant breakthroughs can be expected through the combination of a cryogenic environment, a better detection efficiency, more accurate reconstruction algorithms and carefull monitoring the damage.

Cells treated with nanoparticles were investigated in order to verify whether peptides used for functionalization influence the nanoparticles cellular internalization and finally targeting the cell nucleus. First findings demonstrated here were far from establishing the final conclusion - for which higher statistics would be needed, but still are of importance for the project started by prof. Kysela. For the purpose of this analysis, a method on recognizing and calculating the gold and platinum nanoparticles was developed and applied to collected data. It has been observed that control cells exposed to nanoparticles without targeting peptides indeed do not accumulate significant amount of gold nor platinum. The situation changes in treated samples where signal from gold or platinum is non negligible. However we cannot yet state which kind of targeting peptide alone works better. An important information is that number of nanoparticles coupled to targeted peptides seems for this particular cell line to have a cellular internalization comparable to cells treated with fugene - a transfection reagent which

transiently opens pores in the cell membranes and favors artificially the entrance of nanoparticles. Still the method presented here will be invaluable for further investigations particularly to estimate which nanoparticles from the platinum or the gold is the best strategy. The one which especially awaits its turn is the distribution of nanoparticles in full volume; basically the need of performing similar experiment but in 3D. Although we do not deny the importance of 2D investigations, we do agree that in some cases the results in 2D may be misinterpreted. As we only look on a projection of a cell, it is not trivial to distinguish whether some nanoparticles are really inside the cell cytosol or nucleus or simply stick to its surface. There would be no such a doubt in case of a 3D study.

The investigations presented in this work were based mostly on combined use of hard X-ray fluorescence and phase contrast imaging. Both techniques suit each other well and are further correlated with other, non-synchrotron techniques such as STIM and AFM. This correlative imaging approach [89] fully exploits the quantitativeness of the measurements and provides answers to numerous problems taken up in this work. It can be expected that together with an improvement of spatial resolution, X-ray microscopy will serve even better the tremendously growing demand on cellular studies. Finally, unavailable to be correlated for the moment and standing just step further, techniques such as TEM - will certainly work equally well in synergy with X-ray microscopy in the future.

Résumé de Thèse en Français

Ce travail de thèse présente une combinaison unique d'imagerie X par contraste de phase avec la fluorescence X pour des échantillons biologiques étudiés par nanosonde par fluorescence X excitée par le rayonnement synchrotron. Les récents développements dans ce domaine ouvrent la possibilité d'une imagerie chimique quantitative à l'échelle

sub-cellulaire. Ceci a été rendu possible par l'utilisation d'un outil unique qui est la station de nanoimagerie X ID22NI de l'ESRF qui permet de délivrer un faisceau sub-100 nm avec un très haut flux à haute énergie entrainant une sensibilité très haute, de l'ordre de quelques millier d'atomes pour différents éléments (Fe, Cu, Zn,...).
Le couplage des informations issues de l'imagerie X par contraste de phase (masse surfacique de la cellule) et de la fluorescence X (masse surfacique des éléments chimiques) a pu être obtenu pour la première fois donnant accès à une cartographie des éléments chimiques constituant les cellules et de leurs fractions massiques absolues associées. Dans l'immédiat, il n'a été possible que d'étudier des cellules qui ont été congelées rapidement puis lyophilisées. Cependant, une nouvelle ligne de nanoimagerie, NINA, en construction à l'ESRF, fonctionnera comme un cryomicroscope et permettra l'analyse 2D/3D d'échantillons biologiques ou non congelés hydratés. L'extension de l'imagerie chimique 2D présentée dans ce travail à une imagerie 3D représente une importante avancée pour bon nombre de problématiques scientifiques en biologie. Une des limitations de ce type d'analyse est celle des dommages radio-induits à la suite de l'irradiation de l'échantillon par un haut flux de rayonnement ionisant. Il existe que peu ou pas d'étude sur les effets de la nanoanalyse par fluorescence X sur les cellules lyophilisées. Nous avons combiné l'imagerie de phase à l'imagerie par fluorescence X ce qui nous permis de conclure à une rétractation des structures cellulaires accompagne d'une volatilisation des éléments du fait de l'irradiation lors de l'analyse par fluorescence X. Ces aspects ont été confortés par des analyses utilisant une technique complémentaire non-synchrotron de microscopie ionique en transmission et à balayage (STIM). Plus important encore, nous apportons ainsi un outil rapide et non-destructif pour la cellule (imagerie X de phase) qui permet de corriger la perte de masse due à la volatilisation d'éléments légers (C, H, O, N) de la matrice cellulaire. Cette démarche permet de fiabiliser l'analyse quantitative de la composition chimique cellulaire. Cette approche sera précieuse pour corriger ces effets de perte de masse lors de futures analyses tomographiques de cellules entières congelées hydratées. Nous avons également contribué à l'étude de distribution intracellulaire de nouvelles nanoparticules d'or ou de platine fonctionnalisées. Nous avons pu exploiter les données issues de la fluorescence X pour estimer le nombre de nanoparticules et la taille des clusters internalisés au sein des cellules. Toutefois, des expériences sur un plus grand nombre de cellules avec l'imagerie X par contraste de phase menée en parallèle permettraient sûrement de préciser plus finement ces aspects quantitatifs sur le nombre de nanoparticules intra-

cellulaires.
Dans l'ensemble ce travail ouvre la possibilité d'une imagerie chimique quantitative absolue sub-cellulaire en 2D ou 3D avec la perspective d'imagerie corrélative avec de nombreuses techniques complémentaires notamment la microscopie électronique à transmission pour l'ultrastructure, la microscopie de fluorescence pour la localisation de proteines d'intérêts et d'autres techniques d'analyses chimiques telles le nano-SIMS ou le nano-PIXE.

Appendix A

J. Synchrotron Rad. (2012). 19, 10-18

Status of the hard X-ray microprobe beamline ID22 of the European Synchrotron Radiation Facility

Gema Martinez Criado, Rémi Tucoulou, Peter Cloetens, Pierre Bleuet, Sylvain Bohic, Jean Cauzid, Isabelle Kieffer, Ewelina Kosior, Sylvain Labouré, Sylvain Petitgirard, Alexander Rack, Juan Angel Sans, Jaime Segura-Ruiz, Heikki Suhonen, Jean Susini, Julie Villanova

Abstract

The ESRF synchrotron beamline ID22, dedicated to hard X-ray micro-analysis and consisting of the combination of X-ray fluorescence, X-ray absorption spectroscopy, diffraction and 2D/3D X-ray imaging techniques, is one of the most versatile instruments in hard X-ray microscopy science. This paper describes the present beamline characteristics, recent technical developments, as well as a few scientific examples from recent years of the beamline operation. The upgrade plans to adapt the beamline to the growing needs of the user community are briefly discussed.

key words

X-ray microprobe, X-ray nanoprobe, X-ray fluorescence, microspectroscopy

A.1 Introduction

Among the 40 beamlines in operation at the European Synchrotron Radiation Facility, ID22 is fully dedicated to hard X-ray microanalysis consisting of the combination of X-ray fluorescence (XRF), X-ray absorption spectroscopy (XAS), X-ray diffraction (XRD) and X-ray imaging (XRI) techniques in the hard multi-keV X-ray regime (Somogyi *et al.*, 2005). The beamline is composed of two experimental stations, which permit studies in several research fields like medicine, biology, earth and planetary sciences, environmental science, archaeometry and materials science. These disciplines seek non-destructive investigation of the spatial distribution, concentration and speciation of trace elements to be correlated to the morphology and crystallographic orientations at the (sub)micrometer levels. Both stations share a common instrumental setup: an X-ray focusing device, a high-precision stage to raster the sample on the beam, a visible light microscope (VLM) to visualize the regions of interest of the samples, as well as some detection schemes and 2D/3D XRI approaches.
After several years refining the analytical methods, hard X-ray focusing devices, positioning stages and detection schemes, two hutches are clearly defined today by their spatial resolution: EH1 devoted to microanalysis and EH2, also known as ID22 Nano-Imaging station (ID22NI), exclusively used for nanoanalysis (see Table I). The stations offer a large variety of well-established approaches:

1. EH1: Scanning-XRF and XRF-tomography, micro-XAS and XANES imaging, X-ray excited optical luminescence, linear dichroism, scanning XRD, absorption/phase contrast tomography, and diffraction-tomography.

2. EH2-ID22NI: Scanning-XRF and XRD, XRF- and XRD-tomography, X-ray projection microscopy, full-field magnified tomography, and coherent scanning X-ray diffraction.

The flexible design, long working distances, and high penetration powers also allow the integration and development of different controlled sample environments in EH1. A few examples include anvil cells, microfurnace, He chamber, cryostreams as well as other environments routinely integrated in the beamline (LINKAM HSF91 stage for heating and freezing applications, He mini-cryostat, etc). An additional development

to be shared between both stations is the confocal XRF mode using a polycapillary half-lens pioneered by the MiTAC group (Vincze *et al.*, 2004). In the next section the major technical upgrades recently performed at ID22 are summarized.

A.2 ID22 Instrumentation

A.2.1 X-Ray Source

Currently the high-β straight section of ID22 is equipped with two insertion devices: an in-vacuum U23 and a revolver U35/U19. Table II summarizes the main parameters for both undulators. The photon flux emitted by both devices is presented in Fig. 1, calculated at 30 m from the source through a 0.5×0.5 mm^2 pinhole (the insertion device U42 is depicted for reference purposes only). The electron beam characteristics included a current of 200 mA, an energy of 6 GeV, and a relative energy spread of 0.001. The vertical (horizontal) emittance, β values and dispersion are 39 pm (3.9 nm), 3 m (37.2 m) and 0 (0.137 m), respectively. The revolver device was chosen to give maximum photon output in a very narrow energy range centered on 17.5 keV that is the principal working energy at ID22NI. It has at least the same performance as a conventional U42 undulator in terms of gap reproducibility and speed. The device is equipped with a tunable undulator (U35) and a dedicated (optimized) low K undulator specific to the need of the beamline (U19). The switching between one undulator to the other takes about 2 minutes including the opening of the gap to 250 mm, the rotation of the girders, and the gap closure with the revolver undulator to 11 mm. It is almost transparent to the user. The availability of two interchangeable magnetic structures (35 and 19 mm period) combined with the U23 in-vacuum undulator allows for better optimization of the X-ray photon flux for various energy ranges, overcoming the old configuration based on a U42 undulator, which created an energy gap between 15 and 18 keV.

A.2.2 End-station EH1

Microprobe setup

An overview of the experimental arrangements of ID22 end-stations is depicted in Fig. 2. The end station EH1 has two parts: the full field tomography table and the microcrope setup. In order to explore the merits of high energy (up to 65 keV), a special pair of crossed mirrors in Kirkpatrick-Baez (KB) configuration is installed at the microprobe setup (Borchert *et al.*, 2010). It comprises two elliptically shaped Si mirrors, a 170 mm long mirror focusing at 390 mm distance from the center of the mirror in the vertical direction, and a 92 mm long mirror with a 190 mm focusing distance in the horizontal direction. They are coated with graded multilayers (B4C/[W/B4C]40/Cr), playing both monochromatization and focusing roles. Four actuators (μ-Focus picomotors) bend the flat polished mirrors (CoastLine Optics) into the elliptical figures required for imaging the X-ray source. Both arms of each bender are equipped with linear encoders (Mercury 3500). This design provides reflectivity of 96 % at 65 keV and 75 % at 8 keV. Thus, we can exploit both pink and monochromatic beam operations based on Bragg diffraction and total external reflection modes, respectively. The pink beam approach uses the standard multilayer configuration to increase beam divergence (numerical aperture), producing a very high photon flux (10^{12} photons/s). The second strategy optimized for spectroscopic acquisitions relies on grazing incidence to provide a monochromatic beam flux of about 5×10^{10} photons/s. In the high energy range, the beamline is well-equipped: First, the in-vacuum undulator provides a high photon flux, and second, the Kozhu double crystal monochromator, which can cover an angular range from 2.6 to 32.5 degrees from 2.6 to 32.5 degrees [i.e., $(3.7 - 43.5)$ keV energy range for Si(111), and $(7.1 - 83.5)$ keV for Si(311)]. The resulting spot size at the focal plane of about 1×4 μm^2 (v $\times$ h) is shown in the upper part of Fig. 3.

Full field tomography setup

Figure 4 shows the full field micro-tomography setup, which is located upstream from the focusing optics on EH1 (Weitkamp *et at.*, 1999). This retractable stage provides complementary information and is often used preliminarily to investigate specimens (e.g. to the select a specific ROI within a larger object and/or to select the most

representative of a number of samples). The full setup is mounted on a table and a high precision linear stage that guarantees not only repeatability but also an easy and quick switch with the microprobe (Artioli *et al.*, 2010). The system includes the high precision air bearing rotation stage UPR-160Air (miCos GmbH), the tilt, the vertical translation stage, and the CCD camera ESRF standard FReLoN 2k 14bit (Labiche *et al.*, 2007). The readout speed of the FReLoN detector depends drastically on the operation mode (full-frame, frame transfer, kinetics pipeline), binning, dynamic range and the ROI. The most frequently employed mode gives about 100 ms readout time without region-of-interest or binning (Labiche *et al.*, 2007). Similarly, the spatial resolution depends on the scintillator screen, the numerical aperture of the objective, as well as the effective pixel size used. Frequently, it is adapted together with the desired field of view and can reach up to the sub-micrometer range. For the reconstruction of the tomographic images the filtered-backprojection algorithm is used via the ESRF software package PyHST (Mirone *et al.*).

A.2.3 End-station EH2-ID22NI

Nanoprobe setup

Located at 64 m from the source, the nano-focusing optics consist of two graded multilayer coated surfaces mounted in crossed KB configuration (Morawe *et al.*, 2006). It is composed of a 112 mm long mirror focusing at 180 mm distance from the center of the mirror in the vertical direction and a 76 mm long mirror with a 83 mm focusing distance in the horizontal direction. Four actuators (μ-Focus picomotors) bend the flat polished mirrors (CoastLine Optics) into the elliptical figures required for imaging the X-ray source. Both arms of each bender are equipped with linear encoders (Mercury 3500). This design provides reflectivity of 73 % at 17 keV and 74 % at 8 keV. The resulting spot size at the focal plane of about 60×60 nm^2 (v $\times$ h) is shown in the lower part of Fig. 3. The vertical mirror images the undulator source ($\sim$ 25 μm FWHM), whereas a virtual source is created in the horizontal direction using the high heat-load slits (depending on the spatial resolution and photon flux required by the experiment, from 10 up to 25 μm). The multilayer mirrors play both the role of focusing device and monochromator, resulting in a very high flux of about 5×10^{12} photons/s and medium

monochromaticity of $\Delta E/E \approx 10^{-2}$. Invar, as material of choice for the benders, has improved the thermal stability (Tucoulou *et al.*, 2008), and in particular, the stability of the incident angles and curvature of the elliptically shaped mirrors. A complete description of the nanofocusing optics and nanoimaging station can be found elsewhere (Barret *et al.*, 2011; Hignette *et al.*, 2007; Zhang *et al.*, 2010; Cloetens *et al.*, 2011). The main characteristics of previous focusing systems are listed in Table III.

Polycapillary optics

Policapillary optics in confocal detection geometry can be used as a spatial filter for all applications in which background radiation, from areas not in the region of interest, interferes with the signal under study. XOS monolithic polycapillary optics optimized to a working distance of 2.5 mm and a cut-off energy of 15 keV is available at the beamline with a transmission efficiency of about 2.5 % at 15 keV. Thus, the spontaneous radiation background is practically eliminated from the spectrum and therefore the detection sensitivity and accuracy is greatly improved. Also, buried structures can be studied by depth-sensitive X-ray absorption spectroscopy in fluorescence detection mode at the micrometer scale. In summary, these lenses can be used in our scanning fluorescence microscopes for high-resolution 2D mapping, as well as confocal XAS acquisitions, 3D XRI and XRF tomography experiments.

A.2.4 Sample Environments

HP and HT diamond anvil cell

Within the framework of a close collaboration with the Laboratoire des Sciences de la Terre (ENS-Lyon, France), a diamond anvil cell dedicated to XRF analysis under high pressure and high temperature was drafted, built and tested at EH1 (Petitgirard *et al.*, 2009), allowing *in-situ* geochemical studies of heavy elements, rare earth elements (REE), and first transition metals at ppm concentration levels. The designed system enables XRF detection at 90° from the incident beam using the thermally isolated 13 element Si(Li) solid state detector located 50 mm from the sample position. Elements like Rb, Sr, Y, Zr, with concentrations as low as 50 ppm were detected with the

cell operating at 5.6 GPa and 1273 K. Its vacuum chamber (10^{-3} mbar) presents an optimized shielding and collection geometry that significantly reduces the background radiation (Figure 5). As a result, for the above mentioned elements minimum detection limits of about 0.3 ppm were estimated using such a setup (Petitgirard *et al.*, 2009). In order to properly handle its 15 kg weight, special translation and rotation stages are incorporated, allowing a precise and robust positioning within the micrometer length scale (MICOS and Huber motors of high repeatability in the micron range, with also long travel and sub-micron resolutions). XRD acquisitions in transmission configuration are also suitable over the same high pressure-temperature range.

He mini-cryostat

A compact He mini-cryostat has also been well integrated in EH1. For variable low-temperature investigations (11 − 300 K), its special technical design provides precise scanning capabilities and allows easy access for multiple detection modes (Martinez-Criado *et al.*, 2007). The chamber is high-purity-Al made to avoid background contributions to collected XRF data. To guarantee an extremely short working distance (4.5 mm) and optimized numerical aperture for X-ray excited luminescence studies (Martinez-Criado *et al.*, 2011), the usual thermal shielding used between the sample holder and the window was not included. As a result, the He consumption (13 liters/day at 11 K) is a bit higher than in standard conditions. The sample change time (60 min), on the other hand, is determined by the long thermal response to warm the system up. Finally, the choice of the window material depends on the wavelength and intensity of radiation and, whether polarization is required. The mini-cryostat not only allows substantial access but also reduces X-ray scattering by eliminating air path (very important for XRF). In addition, electrical contacts are available when transport- and/or electric field-dependent studies are required.

Linkam stage

Commercially available heating-freezing stages also provide accurate and stable temperatures. To operate in the -196° to 600°C range, a HSF91 stage (Linkam Scientific Instruments) compatible with our microprobe setup is available. The scheme is op-

timized for vertical mounting and has high temperature stability (< 0.1°C). With a compact and versatile design for easy mounting, it is supplied with a thermal jacket for tighter control of the sample environment (kapton or mica windows). The pure silver heating element has even a transverse aperture to accept a quartz capillary loaded with sample. This guarantees the sample is heated from all sides ensuring temperature homogeneity. For operation below room temperature, there is an automated cooling pump with two litre dewar and 80 cm tube that tolerates a minimum stage temperature of -100°C. The system includes a standalone T95-LinkPad system controller with data sampling of 20 times per second. Heating rates can reach up to 150°C/min. The controller has RS232 connectivity control and programmable outputs for synchronization purposes with our beamline devices.

A.2.5 Detection Schemes

13 element detector

New requirements in terms of detection limits and acquisition rates fostered the installation and commissioning of a LN2 cooled multielement Si(Li) detector (Gresham Scientific Instruments, UK) (Letard *et al.*, 2006). Thirteen Si(Li) crystals mounted on a spherical holder form a close packed array, each element being equidistant from the centre of the sphere. The collimated, active area of each crystal is 50 mm^2. It provides a large total active surface (650 mm^2) in optimized compactness (95 mm diameter) without any observable cross-talk effect. The thickness of the crystals is 3.5 mm which preserves the efficiency over the $8 - 20$ keV energy range. The efficiency falls off above 25 keV, with 60 % at 30 keV. Each crystal is individually protected by a 12 μm-thick Moxtek DuraBeryllium vacuum window. The digital signal processing system was manufactured by X-ray Instrumentation Associates (XIA, California). It is made of four-channel Digital X-ray Processor XMAP modules, designed specifically for quick X-ray mapping (continuous scans). The theoretical maximum throughput is 10^6 counts per second (cps) and per channel. However, detection dynamics are significantly reduced by the detector linearity as well as scattering effects. The peaking time can be set between 0.1 and 100 μs. In a high counting rate configuration (1 μs peaking time), the linearity measurements showed less than 80 kcps for a dead time of about

30 % (much lower for low counting rate – 12 μs peaking time). External triggering can be used for synchronization with other processes such as energy scans or sample motions. The average energy resolution is 150 eV at 5.9 keV (for a peaking time of 12 μs and 1000 cps). The detection limits (for 10 s integration time) are below 0.1 ppm for elements heavier than Mn (Letard *et al.*, 2006).

Silicon drift detectors

Another alternative detection often used in EH1 is the silicon drift detector (SDD) technology. The use of the 13 element detector (13ED) has been proved to be efficient in many cases (e.g., experiments requiring high energy resolution or elemental traces), however often the relatively low photon count rate of such Si(Li) detectors limits the acquisitions (e.g. in XRF tomography). Furthermore, the combination of the high photon flux ($> 10^{11}$ photons/s in the focal spot) and a large variety of sample thicknesses and matrices makes scattering radiation frequently one of the saturation sources. In that context, the complementary SDD technology offers not only lower detection limits and photon count rates at the expense of a slightly decreased energy resolution (150 eV), but also compactness due to the absence of LN2 cooling. In consequence, based on the XIA electronics, two SDDs (Vortex-EX, SII NanoTechnology Inc.) are available. The 50 mm^2 single element SDD produced from high purity silicon using state-of-the-art CMOS production technology operates with thermoelectric cooling. The drift structure ensures very low capacitance and low noise. In principle, at a peaking time of 0.25 μs output count rates up to 600 kcps are achievable. The real count rate measured with 1 μs peaking time is about 175 kcps.

FReLoN camera for X-ray diffraction

For (powder-)diffraction experiments, commonly a large field of view camera with low resolution compared to XRF but high quantum efficiency is required. Accordingly, the taper version of the ESRF FReLoN camera (Labiche *et al.*, 2007) is used at the beamline. It consists of a FReLoN F_K4320T (Kodak) equipped with 3.3/1 demagnifying fibre optics taper hardly bonded to the CCD chip (46 μm effective pixel size, (94 mm)^2

field of view, sensitivity: 1 adu per incident 20 keV X-ray photon, 0.5 DQE at 20 keV). A 50 μm thick Gadox powder scintillator screen converts the X-rays into visible light photons. The use of a Kodak chip offers a high sensitivity of about 3.9 adu per incident 20 keV X-ray photon and a 0.6 DQE at 20 keV. A micro-photodiode is also integrated in the beamstop to record simultaneously the transmitted intensity.

A.3 Examples of recent scientific applications

The beamline's potential for simultaneous trace element detection and mapping, quantitative fluorescence analysis, chemical state specificity and structural probe, make it ideal for a wide range of disciplines: biology, medicine, environmental and earth sciences, art and archaeology as well as material sciences. The versatile instrumentation of ID22 have offer an excellent scheme to carry out unique projects. The next sections illustrate some of the research activities that have been carried out recently, focused mainly on, but certainly not limited to, the following fields: biomedical, earth and environmental, and materials sciences.

A.3.1 Biomedical sciences

Various examples of applications include cellular physiology, pharmacology, and toxicology of metal ions involved in biological processes, often called bio-metals (Bohic *et al.*, 2011; Lewis *et al.*, 2010; Carmona *et al.*, 2010; Bacquart *et al.*, 2010; Ortega *et al.*, 2009; Corezzi *et al.*, 2009). For instance, the biological role of trace elements of Zn and Fe in brain cells has recently been examined by Bohic *et al.* using nano-XRF on ID22NI. In the report the authors address some of the cellular and molecular processes controlling the entry and distribution of these metals in the brain, as well as their roles in synaptic transmission, in the pathogenesis of some neurologic diseases such as Parkinson's and Alzheimer's diseases, and their impact on cognitive functions.
Another example is the direct speciation analysis of As in sub-cellular compartments by micro-XAS in EH1 with a 10^{-15} g detection limit by Bacquart *et al.* Their findings show that inorganic arsenite, $As(OH)_3$, is the main form of arsenic in the cytosol, nucleus, and mitochondrial network of cultured cancer cells exposed to As_2O_3, whereas

As(III) species dominate in HepG2 cells exposed to $As(OH)_3$. On occasion, oxidation to a pentavalent form in nuclear structures of HepG2 cells was observed, suggesting an inter-individual variability in a cell population, that could only be examined by sub-cellular speciation analysis.

In cancer therapy, research has recently been focused on the development of nanocarriers that can aid diagnosis, deliver therapeutic agents and monitor treatment progress. In this context, nano-XRF has been used on ID22NI to investigate intracellular localization of novel lanthanide-coated nanoparticles in human cells and their genotoxicity screening after internalization (Lewis *et al.*, 2010). The results show that, depending on the charge of the coating complex and the presence of the DNA cargo, the internalization of functionalized nanoparticles by human fibroblasts can cause elevated levels of DNA damage. In the same way, applying nano-XRF on ID22NI, Carmona *et al.* recently found that manganese is located within the Golgi apparatus of PC12 dopaminergic cells at physiologic concentrations (see Fig. 6). Generally chronic exposure to manganese results in neurological symptoms called manganism, which is identified as a risk factor for Parkinson's disease. Thus, the striking intracellular redistribution of Mn found by Carmona and co-workers indicates that the Golgi apparatus plays an important role in the cellular detoxification of Mn.

A.3.2 Earth and environmental sciences

The investigations in this area cover exploration from the earth interior up to stellar particles: homogeneity of the deep mantle, fluid-mineral relationships in the upper mantle, tracking elemental speciation in crustal melts and fluid sources in hydrothermal settings, as well as the nature of extra-terrestrial materials (Carbone *et al.*, 2011; Simionovici *et al.* 2011; Borchert *et al.*, 2010; Petitgirard *et al.*, 2009; Reith et al., 2009). Carbone and co-workers recently used micro-XRD, micro-XRF and micro-XAS to investigate metal speciation in mine wastes and soils. The authors studied Fe-rich hardpans within waste-rock dump and show that the authigenic iron-rich phases generally contain significant amounts of hazardous elements such as Cu, Zn, Mo, As, and Se. Moreover, a significant mineralogical control on the mobility of these elements was observed; in particular, the goethite-rich assemblages show high affinity for Cu and Zn, whereas hematite-rich assemblages selectively concentrate As, Se, Mo, Cu and Zn.

On the other hand, Borchert *et al.* have examined the partitioning of Ba, La, Yb and Y between haplogranitic melts and aqueous solutions under *in-situ* conditions in EH1. Their findings show a strong influence of the composition of the starting fluid and melt with no dependence on temperature and only weak dependence on pressure. For chloridic fluids, there was a sharp increase in the Ba, La, Y and Yb partition coefficients with the alumina saturation index. Their results imply that both melt and fluid compositions have a strong influence on trace element behavior, while the complexation of Ba, REEs and Y is not controlled by the presence of Cl- in the fluid only, but likely by interaction of these elements with major melt components.
The cycling of rare and precious metals, such as gold, has been also analyzed in ID22NI. In previous studies, researchers reported the presence of bacteria on gold surfaces, but never clearly elucidated their role. Recently, Reith *et al.* found that the bacterium Cupriavidus metallodurans catalyses the biomineralization of gold by transforming toxic gold compounds to their metallic form using an active cellular mechanism. So, there may be a biological reason for the presence of these bacteria on gold grain surfaces. The distribution of gold and other elements was mapped in individual cells (see Fig. 7) After 1 min of exposure to Au(III), cells had taken up 1.82 ng cm^2 of Au, and accumulated Au was distributed throughout the cells. After 72 h, zones containing up to 34.6 ng cm^2 Au were detected. These hot spots were associated with cell envelopes, suggesting that cells actively removed gold from the cytoplasm and precipitated it as nano-particulate metallic gold in the periplasm. The discovery of an Au-specific means opens the doors to the production of biosensors, which will help mineral explorers to find new gold deposits.

A.3.3 Materials sciences

In this broad field, several scientific issues have been addressed using the beamline stations. The recent research comprises many materials with potential applications in spintronics, catalysis, optical sources, renewable materials like solid oxide fuel cell and silicon solar cells, etc (Sancho-Juan *et al.*, 2011; Basile *et al.*, 2010; Mino *et al.*, 2010; Palancher *et at.*, 2010; Kwapil *et al.*, 2009; Martinez-Criado *et al.* 2009). For example, the combined use of micro-XRF, micro-XRD and nano-XRF techniques has been applied to the characterization of active-phase-coated metallic supports, struc-

tured catalysts, at different scales in both scanning and tomographic modes by Basile *et al.* In particular, coating of FeCrAlY foams were examined, which are gaining attention because they improve heat transfer. The results show that the morphology of the coating depends on the synthesis conditions and that the catalyst may be described as Ni metal crystallites dispersed on γ-Al_2O_3, homogeneously coating the FeCrAlY foam. Another recent experiment applied XRD scanning tomography to an annealed γ-$U_{0.85}Mo_{0.15}$ multiphase particle. UMo/Al dispersion fuel is one of the prospective materials as a high uranium density fuel for high performance research reactors due to its excellent stability during irradiation. The results published by Palancher *et al.* revealed a micrometre-scale layered structure morphology, the presence of an embedded 5 μm-thick interdiffusion layer, and an unexpected phase at trace levels which plays a protective role by inhibiting thermally activated Al diffusion into UMo.

The structural characterization of multi-quantum wells in electroabsorption-modulated lasers by Mino *et al* is an excellent example of application in the microelectronic industry. The structural gradient (in both strain and barrier/well widths) that allows this system to operate as an integrated device has been determined with a 2 μm^2 beam, scanning both laser and modulator regions. The investigated material is used for 10 Gbs^{-1} telecommunication applications up to 50 km propagation span. In the same way, it has been recently reported the application of hard X-ray nanoprobe techniques to the structural analysis of pyramidal defects in Mg doped GaN, a potential material for optoelectronic devices (Martinez-Criado *et al.* 2009). Figure 8 shows the XRF data collected at ID22NI. The presence of elemental traces of Cr and Fe is revealed. A blue-red plot displays the Cr- and Fe-K intensity distributions. While the Ga arrangement presents equally spaced and periodic planes sequentially stacked from the hexagonal base (not shown), Cr and Fe exhibit a close correlation on their spatial locations without the 3D pyramidal shape. The observations emphasize the underlying diffusion mechanism, indicating local impurity agglomeration predominantly on the hexagonal base, supporting the occurrence of such pyramids by the kinetics of additional impurities that accompanied Mg incorporation. On the other hand, the strong polarization-dependent-XAS features showed the preservation of the hexagonal crystalline structure in both defect-free and hexagonal pyramids. The X-ray linear dichroism (XLD) shows no preferential disorder in the direction parallel or perpendicular to the crystal growth.

A.4 Long-term: Upgrade Beamline

ID22 will evolve within the frame of the upgrade programme of the ESRF towards the long (185 m), two-branch Nano Imaging and Nano-Analysis (NINA) beamline (https://www.esrf.fr/AboutUs/Upgrade/). The NI end-station will be located at 185 m from the source and will mainly address problems in biology, biomedicine and nano-technology. It is optimized for high-resolution quantitative 3D imaging techniques with a specific focus on X-ray fluorescence and projection microscopy. This branch will be optimized for ultimate hard X-ray focusing of a beam ($10 - 20$ nm) with a large energy bandwidth ($\Delta E/E \sim 10^{-2}$) at specific energies (11.2, 17 and 33.6 keV). Aiming at life science applications, it will operate in a cryo-environment. The NA end-station, in parallel operation, will be located at approximately 165 m from the source and will be optimized for high resolution (50 nm -1 μm) spectroscopic applications ($\Delta E/E \sim 10^{-4}$), including XRF, XAS and XEOL. It will offer a multi-modal approach (XAS, XRD, XRI) capable of *in-situ* experiments. In a complementary way to the NI end-station, NA will provide a monochromatic beam tunable in a large energy range ($5 - 70$ keV). The initial development is performed through the station ID22NI under the supervision of P. Cloetens. The NINA beamline will be located on port ID16 and is scheduled to open for users in 2014. In summary, the NINA beamline will provide complementary techniques at the nano-scale for the study of a wide variety of samples, overcoming current ID22 limitations to meet the growing user demands.

A.5 Conclusions

The ID22 beamline at the ESRF is a state-of-the-art instrument for hard X-ray micro-analysis and 2D/3D X-ray imaging at (sub-)micrometer scales. The end-stations suit a large variety of research fields demanding multiple techniques, very tiny spot sizes (from microns to 60 nm), high photon flux (up to 5×10^{12} ph/s) and also high energies ($6.5 - 65$ keV). The smooth operation derives from the successful integration of high quality focusing optics, reliable scanning mechanisms, high precision mechanical components, efficient detection schemes and stable alignment. Various sample environments allow versatile tailoring of experiments.

References

Artioli, G. & Cerulli, T. & Cruciani, G. & Dalconi, M. & Ferrari, G. & Parisatto, M. & Rack, A. & Tucoulou, R. (2010). *Anal. Bioanal. Chem.*, **397**, 2131–2136.

Bacquart, T. & Deves, G. & Ortega, R. (2010). *Environ. Res.*, **110**, 413–416.

Barrett, R. & Baker, R. & Cloetens, P. & Dabin, Y. & Morawe, C. & Rommeveaux, A. & Suhonen, H. & Tucoulou, R. & Zhang, L. *SPIE* (in press).

Basile F. & Benito P. & Bugani S. & De Nolf W. & Fornasari G. & Janssens K. & Morselli L. & Scavetta E. & Tonelli D. & Vaccari A. (2010). *Advanced Functional Materials*, **20**, 4117–4126.

Bohic S. & Ghersi-Egea J.-F. & Gibon J. & Paolettie P. & Arnaud J. & Hunot S. & Boom A. & Bouron A. (2011). *Revue Neurologique*, **167**, 269–279.

Borchert, M. & Wilke, M. & Schmidt, C. & Cauzid, J. & Tucoulou, R. (2010). *Chemical Geology*, **276**, 225–240.

Carmona A. & Deves G. & Roudeau S. & Cloetens P. & Bohic S. & Ortega R. (2010). *ACS Chemical Neuroscience*, **1**, 194–203.

Cauzid, J. & Philippot, P. & Martinez-Criado, G. & Ménez, B. & Labouré S. (2007). *Chemical Geology*, **246**, 39–54.

Hignette, O. & Cloetens, P. & Morawe, C. & Borel, C. & Ludwig, W. & Bernard, P. & Rommeveaux, A. & Bohic, S. (2007) *Synchrotron Radiation Instrumentation: Ninth International Conference, eds. J-Y Choi S. Rah, AIP Conference Proceedings* 879, 792-795.

Cloetens, P. *et al.* The Nano-Imaging end station ID22NI, under preparation.

Corezzi, S. & Urbanelli, L. & Cloetens, P. (2009). *Anal. Biochem.*, **388**, 33–39.

Kwapil, W. & Gundel, P. & Schubert, M. C. & Heinz, F. D. & Warta, W. & Weber, E. R. & Goetzberger, A. & Martinez-Criado, G. (2009). *Applied Physics Letters*, **95**, 232113.

http://www.esrf.fr/AboutUs/Upgrade/future−beamline−portfolio.

Labiche, J. C. & Mathon, O. & Pascarelli, S. & Newton, M. A. & Ferre, G. G. & Curfs, C. & Vaughan, G. & Homs, A. & Carreiras, D. F. (2007). *Review of Scientific Instruments*, **78**, 091301–091301.

Letard, I. & Tucoulou, R. & Bleuet, P. & Martinez-Criado, G. & Somogyi, A. & Vincze, L. & Morse, J. & Susini, J. (2006). *Review of Scientific Instruments*, **77**,

063705-063705.

Lewis, D. J. & Bruce, C. & Bohic, S. (2010) Nanomedicine, **5**, 1547–1557.

Martinez-Criado, G. & Steinmann, R. & Alen, B. & Labrador, A. & Fuster, D. & Ripalda, J. M. & Homs, A. & Laboure, S. & Susini, J. (2007). *Review of Scientific Instruments*, **78**, 025106–025106.

Martinez-Criado, G. & Alen, B. & Sans, J. A. & Homs, A. & Kieffer, I. & Tucoulou, R. & Cloetens, P. & Segura-Ruiz, J. & Susini, J. & Yoo, J. & Yi, G. (2011). *Nuclear Instruments and Methods in Physics Research B* (in press).

Martinez-Criado, G. & Tucoulou, R. & Cloetens, P. & Sans, J. A. & Susini, J. (2009). *Applied Physics Letters*, **95**, 151909–151909.

http://www.esrf.eu/UsersAndScience/Experiments/TBS/SciSoft/.

Mino, L. & Gianolio, D. & Agostini, D. & Piovano, A. & Truccato, M. & Agostino, A. & Cagliero, S. & Martinez Criado, G. & Codato, S. & Lamberti, C. (2010). *Advanced Materials*, **22**, 2050–2054.

Morawe, C. & Hignette, O. & Cloetens, P. & Ludwig, W. & Borel, C. & Bernard, P. & Rommeveaux, A. (2006). *Book Series: Proceedings of the Society of Photo-Optical Instrumentation Engineers (SPIE)*, **6307**, F3170–F3170.

Ortega, R. & Bresson, C. & Fraysse, A. & Sandre, C. & Devs, G. & Gombert, C. & Tabarant, M. & Bleuet, P. & Seznec, H. & Simionovici, A. & Moretto, P. & Moulin, C. (2009). *Toxicology Letters*, **188**, 26–32.

Palancher, H. & Tucoulou, R. & Bleuet, P. & Bonnin, A. & Welcomme, E. & Cloetens, P. (2010). *Journal of Applied Crystallography*, **44**, 1111–1119.

Petitgirard, S. & Daniel, I. & Dabin, Y. & Cardon, H. & Tucoulou, R. & Susini J., (2009). *Review of Scientific Instruments*, **80**, 033906–.

Reith, F. & Etschmann, B. & Grosse, C. (2009). *Proc. Natl. Acad. Sci. U. S. A.*, **106**, 17757–17762.

Sancho11 Sancho-Juan, O. & Martinez-Criado, G. & Cantarero, A. & Garro, N. & Salome, M. & Susini, J. & Olguin, D. & Dhar, S. & Ploog, K. (2011). *Physical Review B*, **83**, 172103.

Simionovici, A. & Allen, C. & Bajt, S. & Bastien, R. & Bechtel, H. & Borg, J. & Brenker, F. E. & Bridges, J. C. & Brownlee, D. E. & Burchell, M. J. & Burghammer, M. & Butterworth, A. & Cloetens, P. & Davis, A. M. & Floss, C. & Flynn, G. & Frank, D. & Gainsforth, Z. & Grun, E. & Heck, P. R. & Hillier, J. & Hoppe, P. & Howard, L. & Huss, G. R. & Huth, J. & Kearsley, A. T. & King, A. J. & Lai, B. & Leitner, J. &

Lemelle, L. & Leroux, H. & Lettieri, R. & Marchant, W. & Nittler, L. & Ogliore, R. & Postberg, F. & Sandford, S. & Tresseras, J. A. Sans & Schoonjans, T. & Schmitz, S. & Silversmit, G. & Sole, V. A. & Srama, R. & Stephan, T. & Stodolna, J. & Stroud, R. M. & Sutton, S. & Trieloff, M. & Tsou, P. & Tsuchiyama, A. & Tyliczs-zak, T. & Vekemans, B. & Vincze, L. & Westphal, A. J. & Zevin, D. & Zolensky, M. E. (2011). *Meteoritics and Planetary Science*, **46**, A213.

Somogyi, A. & Tucoulou, R. & Martínez-Criado, G. & Homs, A. & Cauzid, J. & Bleuet, P. & Simionovici, A. (2005). *J. Synchrotron Rad.* **12**, 208–215.

Tucoulou, R. & Martinez-Criado, G. & Bleuet, P. & Kieffer, I. & Cloetens, P. & Laboure, S. & Martin, T. & Guilloud, C. & Susini, J. (2008). *Journal of Synchrotron Radiation*, **15**, 392–398.

Vincze, L. & Vekemans, B. & Brenker, F. E. & Falkenberg, G. & Rickers, K. & Somogyi, A. & Kersten, M. & Adams, F. (2004). *Analytical Chemistry*, **76**, 6786–6791.

Weitkamp, T. & Raven, C. & Snigirev, A. (1999) *Book Series: Proceedings of the Society of Photo-Optical Instrumentation Engineers (SPIE)*, **3772**, 311–317.

Zhang, L. & Baker, R. & Barrett, R. & Cloetens, P. & Dabin Y. (2009). *10th International Conference on Radiation Instrumentation, ed. R. Garrett et al.*, **1234**, 801-804.

Table A.1: **Main characteristics of ID22 end-stations.**

	EH1	EH2-ID22NI
Spatial resolution (μ)	1×4	0.065×0.050
Focusing optics	KB Mirrors	KB Mirrors
Max. Flux (ph/s)	5×10^{11}	2×10^{12}
Energy range	$6.5 \rightarrow 65$ keV	17 and 29 keV
Techniques	XRF, XAS, XRD	XRF, XRD
	XRI-2D/3D	XRI-2D/3D

Table A.2: **Summary of the relevant parameters of the revolver undulator U35/19 and the in-vacuum undulator U23.**

Insertion Device	U35/19	U23
Period (mm)	35 / 19	23
Length (mm)	1.6	2.0
Magnet material	NdFeB	Sm_2Co_{17}
Minimum gap (mm)	11	6
Peak field at min. gap, I=200 mA (T)	0.74 / 0.32	0.78
Power density at 30 m, min. gap, I=200 mA (W/mm^2)	97 / 82	181

Table A.3: **Summary of the relevant characteristics of the KB systems.**

KB system	EH1	EH2-ID22NI
Lengths V×H (mm)	170 × 92	112 × 76
Material	Si	Si
Coating	$B_4C/[W/B_4C]_{40}/Cr/Si$	$B_4C/[W/B_4C]_{25}/Cr/Si$
Source Distances, p (m)	41	64
Focal Lengths V×H, q (m)	0.390 × 0.190	0.180 × 0.083
Incidence angles V×H (mrad)	2.5 × 3.5 @ 65 keV	8.1 × 8.2 @ 17 keV
	10.7 × 15.1 @ 15 keV	4.8 × 4.8 @ 29 keV
Spot size (μm)	1 × 4	0.060 × 0.060

Figure A.1: The output spectra of the undulators of ID22 shown as photons s^{-1} (0.1% bandwidth)$^{-1}$ through a 0.5 mm (H) $\times$ 0.5 mm (V) pinhole at 30 m (equivalent to the position and normal slit gaps of the primary slits) from the centre of the undulator. U42 is shown for reference purposes only.

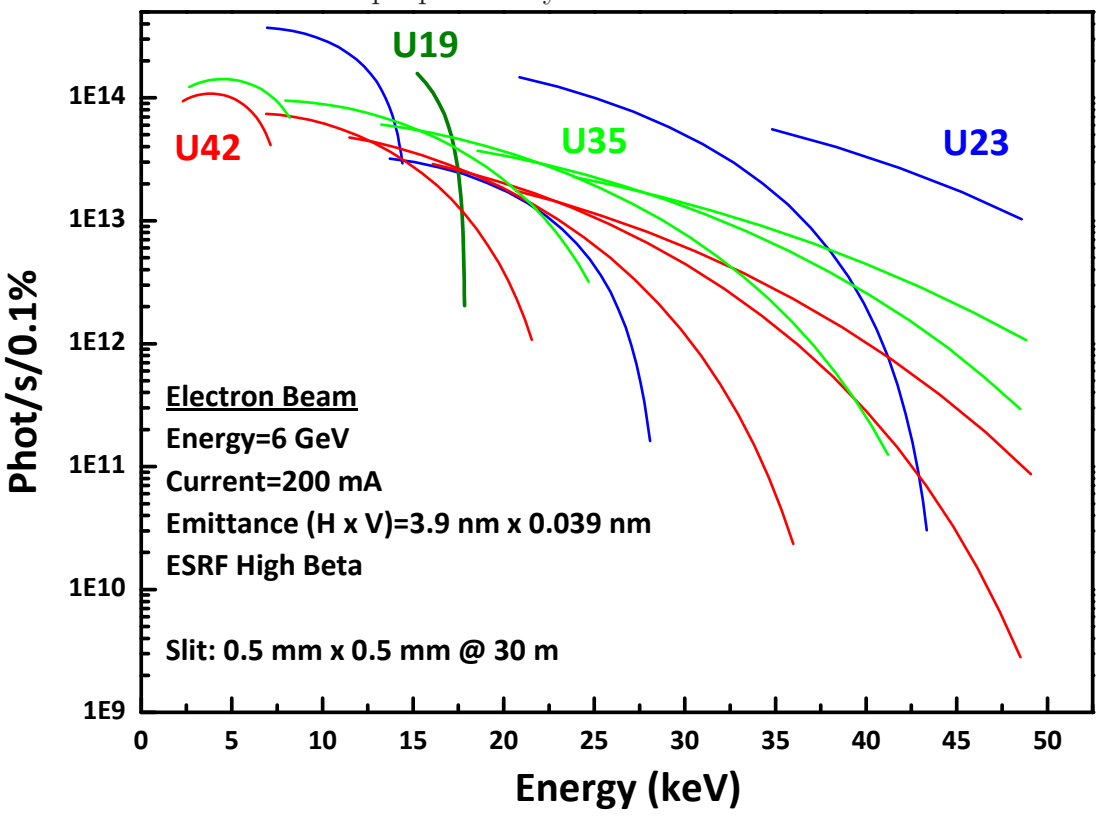

Figure A.2: Overview of the experimental arrangements of ID22 end-stations: EH1 and ID22NI. The upper part illustrates the EH1 end-station: on the right is the full field tomography setup, and on the left the microprobe. The lower part depicts the ID22NI end-station. The direction of the X-ray beam is also indicated. KB represents the Kirkpatrick-Baez mirrors, 13-ED the 13-Element Detector, SDD the Si drift detector,

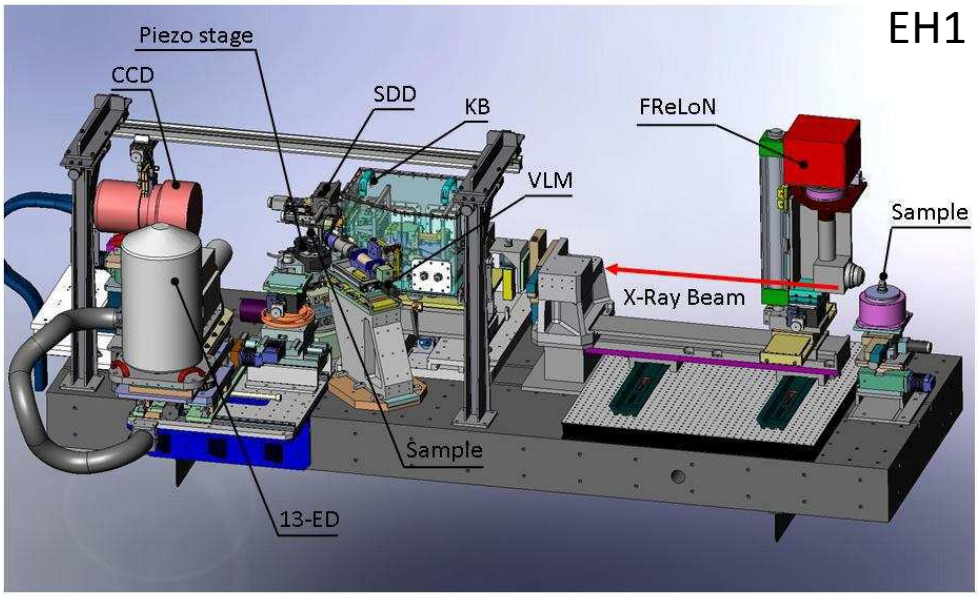

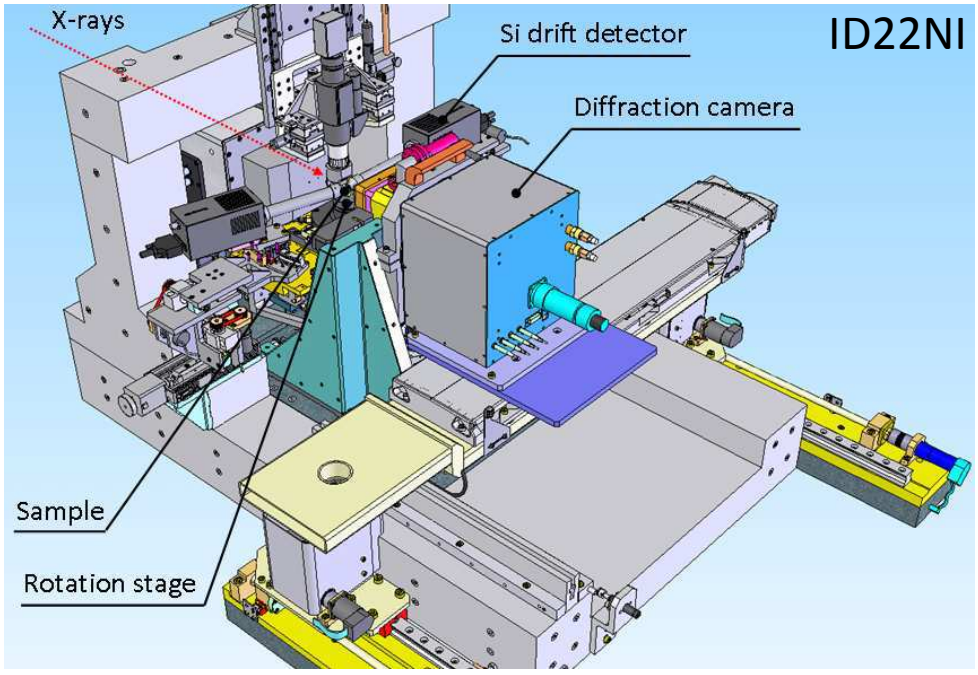

Figure A.3: Focused beam profiles taken at 12 and 17 keV in EH1 (upper part) and ID22NI (lower part) by means of Ni and Au knife-edge scans, respectively. Solid circles represent the raw data and solid lines the respective Gaussian fits.

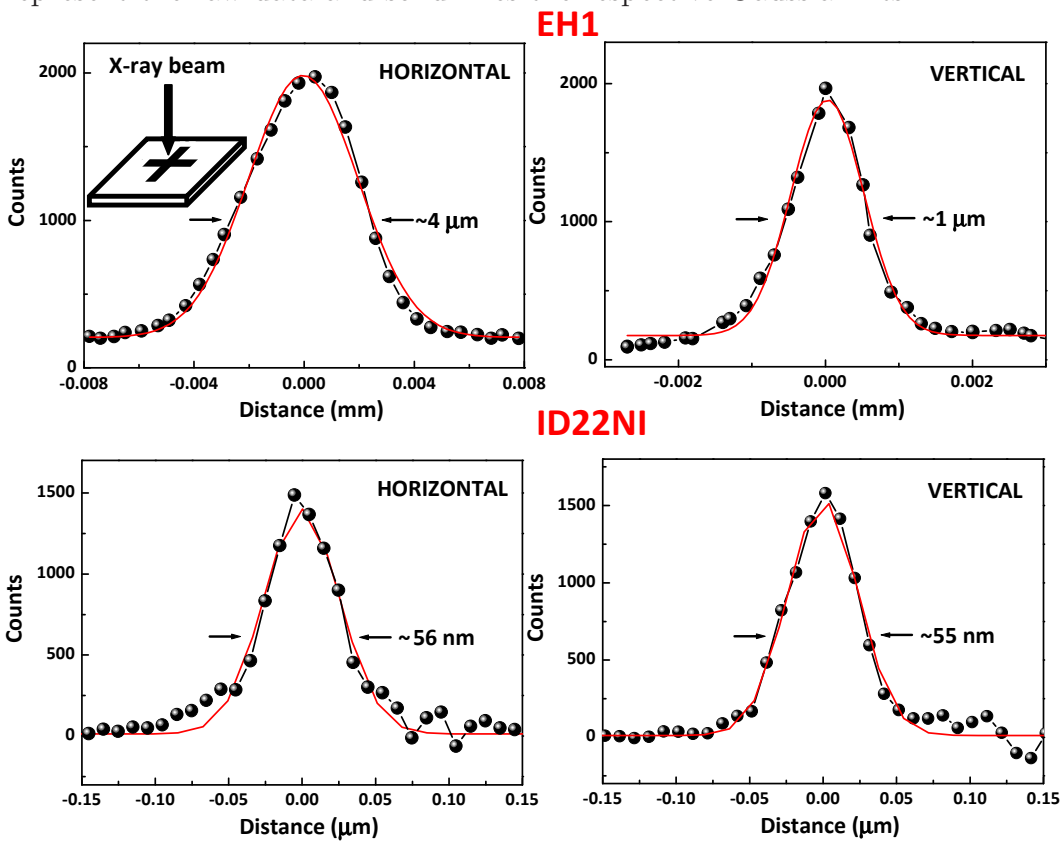

Figure A.4: Photograph of the microtomography station in EH1. The sketch shows the classical layout of a high resolution indirect X-ray detector compromising a scintillator screen, visible light optics and a digital camera (Weitkamp *et al.*, 1999). For alignment
; shown in the
proximately 6

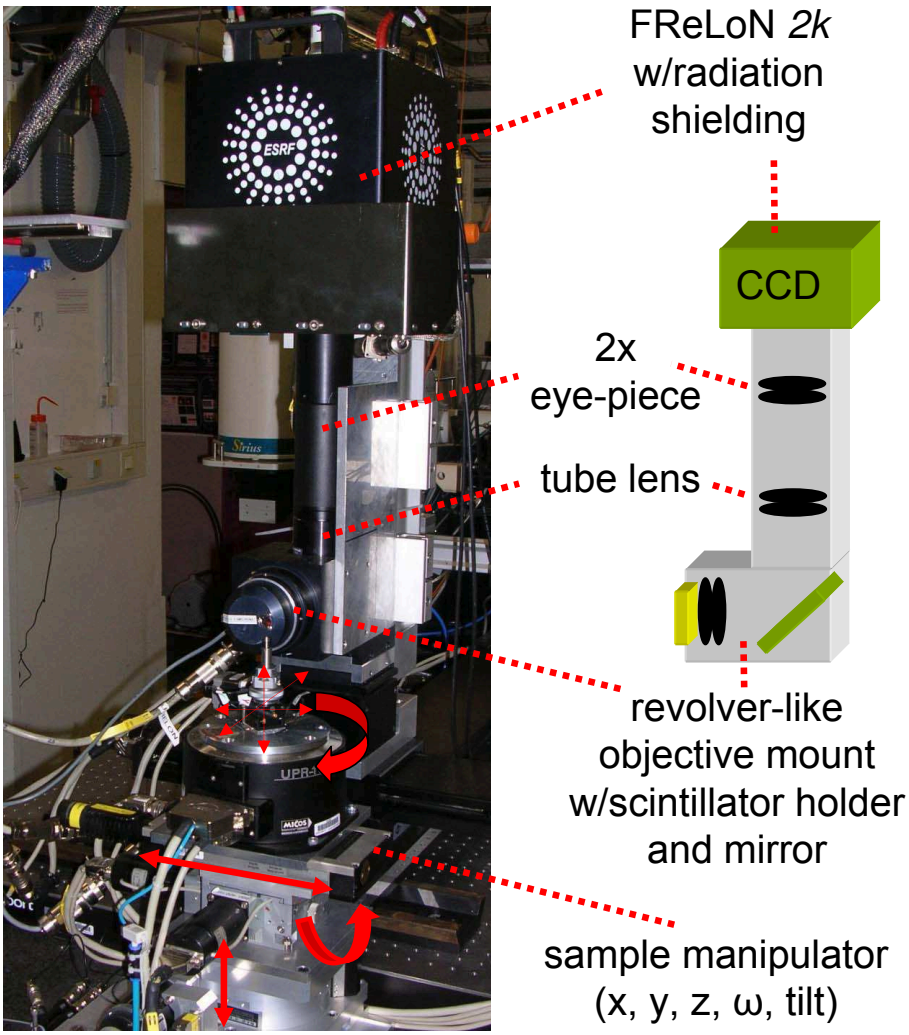

Figure A.5: Schematic cross-section view of the HP (10 GPa) and HT (1000°C) diamond anvil cell showing the optimized geometry that allows simultaneous measurements of XRF, XAS and XRD in EH1. The drawing displays the different components: vessel, cooling, feedtroughs, cell holder. The direction of the X-ray beam is also indicated.

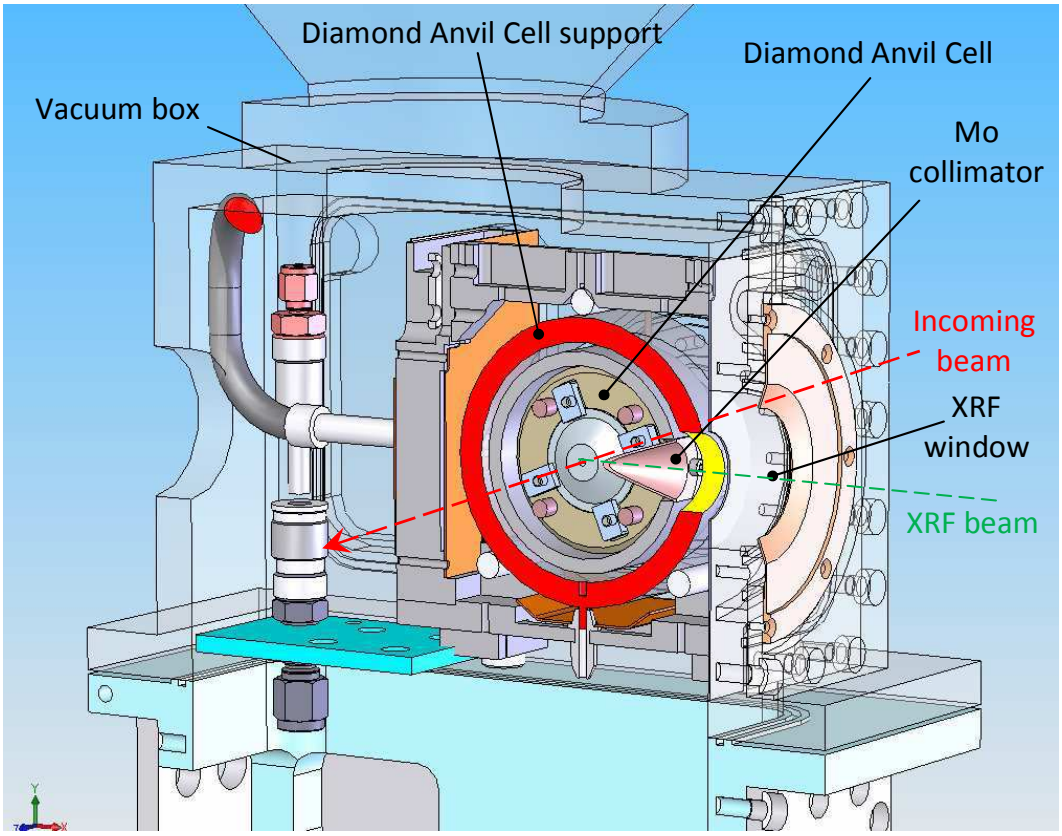

Figure A.6: Optical image, visible fluorescence, X-ray fluorescence and Mn elemental distribution in a PC12 cell exposed to 50 μM of $MnCl_2$ during 24 hours. Scan size is 5 x 5 μm^2. Color bar ranges from blue to red (min to max) is proportional to the number of X-rays detected. Reproduced with permission from Carmona *et al.* (2010),

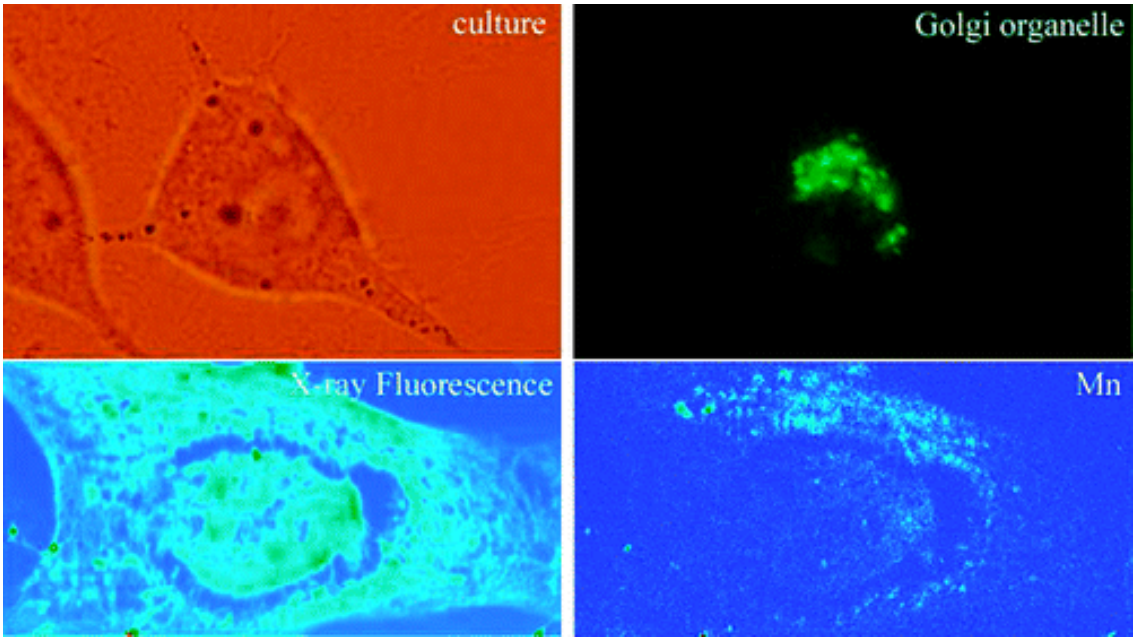

Figure A.7: Quantitative micro-XRF-maps showing the distribution of Au, Ca, Cu, Fe, S, and Zn in an individual cell after 1 min exposure to Au(III) at pH 7.0 [the quantified area is marked in the image, and concentrations are given in the image, concentration ranges for elements are given in the image, concentration ranges for elements are Au, 0-4.16; Ca, 0-18.78; Cu, 0-0.29; Fe, 0-0.44; S, 0-60.52; and Zn, 0-24.57 ng cm-2]. Reproduced with permission from Reith *et al.* (2009), Copyright © 2009 by the National Academy of Sciences.

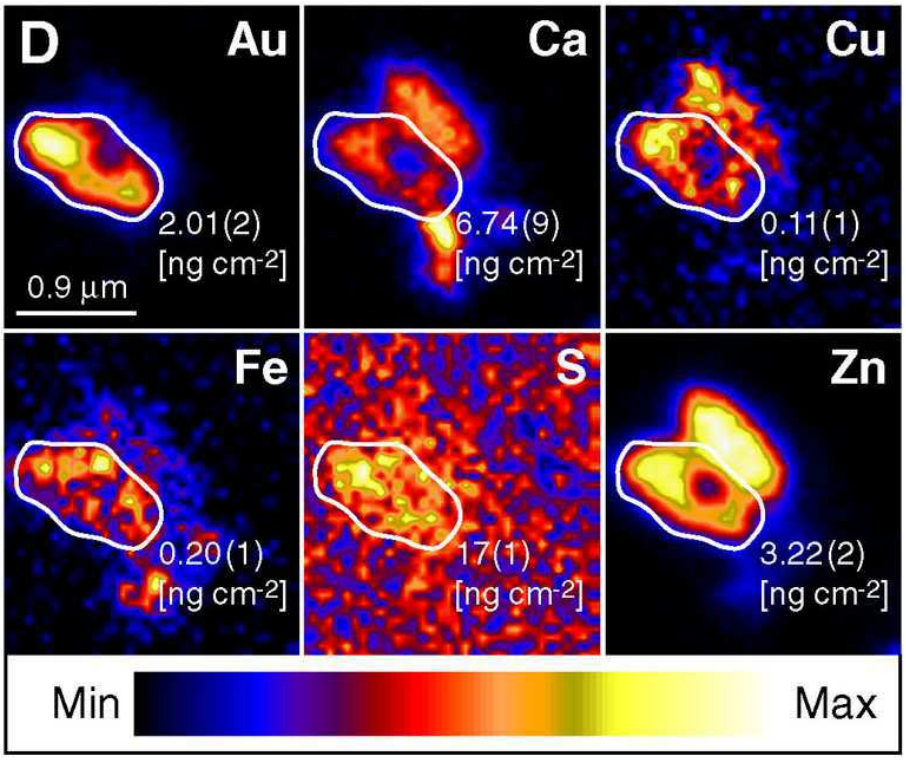

Figure A.8: Upper part: Optical micrograph of the Mg-rich hexagonal pyramids in GaN and blue/red plot displaying the Cr-/Fe-K_α intensity distributions with their corresponding concentrations in the color scales. Lower part: Calculated and measured XANES data around the Ga K-edge for perpendicular/parallel incidence on the pyramid center and outside it, as well as calculated and measured XLD also recorded at the Ga K-edge with the bean [illegible] id outside it.

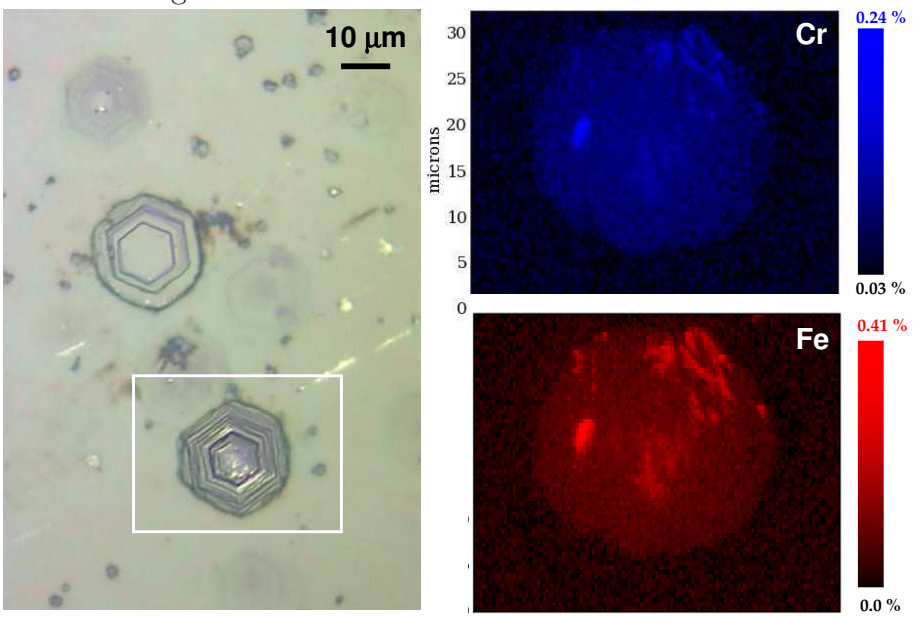

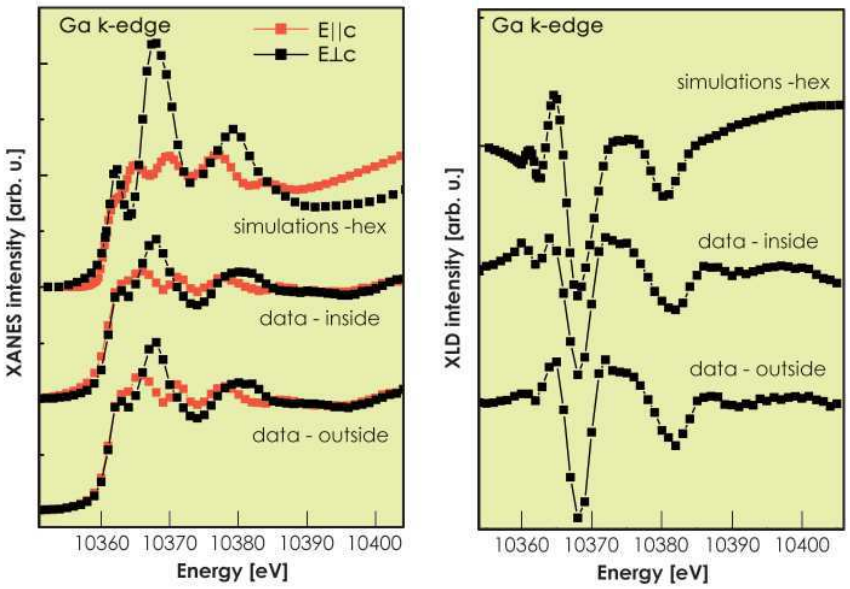

Bibliography

Bibliography

[1] Motz, H. J. Appl. Phys. 22 (1951), 527-535

[2] Kim, K.J. proc. VII National Conference on Synchrotron Radiation. 1986

[3] Born, M. and Wolf, E., Principles of optics, 6th ed. (Pergamon Press, Oxford, New York, 1980). Chapter 10

[4] Goodman, J.W., Statistical Optics (John Wiley and Sons, New York, 1985). Chapter 5

[5] K.J.Kim Nucl. Instr. Meth. Phys.Sect.A 246, 1-3, 1986, 71-76

[6] Auger, P. Sur les rayons secondaires produits dans un gaz par des rayons X, C.R.A.S. 177 (1923) 169-171.

[7] Compton, A. The spectrum of scattered X-rays. Phys. Rev. 22 (1923), 409-413

[8] Huang R. and Bilderback D.H., J. Synchr. Radiat. 13,(2006) 74-84

[9] Pfeiffer F., David C., Burghammer M., Riekel C., Salditt T. Science 297 (5579), 230-234 (2002)

[10] Lagomarsino, S. et al., JAP 79, 44-71 (1996)

[11] Einstein A. Deutsche Physikalische Gesellschaft, 20:86, 1918

[12] Hecht, E. Optics. Reading: Addison Wesley, 1990

[13] Hidekazu M., Soichiro H., Takashi K., Hirokatsu Y., Daisuke Y., et al. Nature Physics, 6(2), 2010, 122-125.

[14] Chao W., Kim J., Rakewa S., Fischer P., Anderson E.H. Optics Express 17(20) 2009

[15] Yang, B.X. Nucl. Instr. and Meth. A 328 (1993) 578.

[16] Snigirev, A., Kohn, V., Snigireva, I., Lengeler, B. Nature 384 (1996) 49

[17] Baryshev, V., Kulipanov, G., Skrinsky, A., Handbook on Synchrotron Radiation, Vol. 3, chapter 16. Elsevier/North Holland (1991)

[18] Bohic, S., Simionovici, A., Snigirev, A., Ortega, R., Devès, G., et.al., 2001. Appl. Phys. Lett. 78 (22), 3544 - 3546.

[19] Ortega, R., Bresson, C., Fraysse, A., Sandre, C., Devès, G., et.al., 2009. Toxicology Lett. 188, 26-32.

[20] Ohsumi, K., Hagiya, K., Ohmasa, M., 1991. J. Appl. Cryst. 24, 340

[21] Bilderback, D.H. 1982. Nucl. Instr. Meth. 195, 67

[22] Berman, L.E. and Hart, M. 1993. Nucl. Instr. Meth. Phys. Res. A334, 617

[23] Marot, G., Rossat, M., Freund, A.K., Joksch, St., Kawata, H., Zhang, L., Ziegler, E., Berman, L.E., Chapman, D., Iarocci, M. 1992. Rev. Sci. Instr. 63, 477

[24] Lee, W.K., Macrander, A.T., Mills, D.M., Rogers, D.S., Smither, R.K. 1992. Nucl. Instr. Meth. Phys. Res. A320, 381

[25] Streenstrup, S. 1981. J. Appl. Cryst. 14, 226

[26] Als-Nielsen, J. and McMorrow, D. Elements of Modern X-ray Physics, Wiley, Chichester (2001) pp. 23, 24, 61106.

[27] Gerchberg, R.W. and Saxton, W.O. 1972. Optik 35, 237-246

[28] Turner, L.D., Dhal, B.B., Hayes, J.P., Nugent, K.A., Paterson, D. et al. 2004. Opt. Express, 12

[29] Paganin, D.M. Coherent X-Ray Optics, Vol.6 of Oxford series on synchrotron radiation, Oxford University Press, Oxford 2006

[30] Langer, M., Cloetens, P., Peyrin, F. IEEE Trans. Im. Proc. 19;9. 2010

[31] Guigay J.P. 1977, Optik 49(1), 121

[32] Zabler, S., Cloetens, P., Guigay, J.P., Baruchel, J., Schlenker, M., 2005. Rev. Sci. Instrum. 76, 1-7.

[33] Mokso, R., Cloetens, P., Maire, E., Ludwig, W., Buffiere, J.Y., 2007. Appl. Phys. lett. 90, 144104.

[34] Cloetens, P., Ludwig, W., Baruchel, J., V.Dyck, J., V.Landuyt, J., et.al., 1999. Appl. Phys. Lett. 75, 2912-2914.

[35] Hignette, O., Cloetens, P., Rostaing, G., Bernard, P., Morawe, C., 2005. Rev. Sci. Instrum. 76.

[36] Blattner, F.R., Guy Plunkett III, Bloch, C., Perna, N., Burland, V., et al. 1997. Science 277 (5331) 1453-1462.

[37] Godin, M., Bryan, A., Burg, T., Babcock, K., Manalis, S. 2007 Appl.Phys.Lett. 91, 123121

[38] Meares, C., Wensel, T., 1984. Acc. Chem. Res. 17 (6), 202-209.

[39] Bush, AI., Curtain, CC., 2008. Eur. Biophys. J 37 (3), 241-5.

[40] Sundberg, RJ., Martin RB, 1974. Chem. Rev. 74 (4), 471-517

[41] Lippard, S. J., Berg, J. M., 1994. Principles of Bioinorganic Chemistry. University Science Books: Mill Valley, CA.

[42] Greene, L. A. and Tischler, 1976. A. S. Proc. natn. Acad. Sci. U.S.A. 73, 2424 2428.

[43] Carmona, A., Devès, G., Ortega, R., 2008. Anal Bioanal Chem 390: 1585-94.

[44] Carmona, A., Devès, G., Cloetens, P., Bohic, S., Ortega, R., et.al., 2010. ACS Chemical Neurosciences. 1, 194-203.

[45] de Jonge, M., Hornberger, B., Holzner, C., Paterson, D., Jacobsen, C., et.al., 2008. Phys. Rev. Lett. 100, 163902.

[46] Di Fabrizio, E., Cojoc, D., Cabrini, S., Kaulich, B., Susini, J., et.al., 2003. Opt. Express 11, 2278-2288.

[47] Marchi, F., Dianoux, R., Smilde, H.J.H., Mur, P., Comin, F., et.al., 2008, 538-547.

[48] Alessandrini, A., Facci, P., 2005. Meas. Sci. Technol. 16, R65-R92.

[49] Barberet, Ph., Incertia, S., Andersson, F., Delalee, F., Serani, L., et.al., 2009. Technical description of the CENBG nanobeam line. Nucl. Instrum. and Methods in Phys. Res. Section B: Beam Interactions with Materials and Atoms. 267, 12-13.

[50] Devès, G., Cohen-Bouhacina, T., Ortega, R., 2004. Spectrochim. Acta B. 59, 1733-1738.

[51] Sole, V., Papillon, E., Cotte, M., Walter, P., Susini, J., 2007. Spectrochim. Acta Part B At. Spectrosc. 62, 63-68.

[52] NBS Journal of Research 87, pp 377-385

[53] Langer, M., Cloetens, P., Guigay, JP., Peyrin, F., 2008. Med. Phys. 35(10), 4556-66.

[54] Snyder, W. S., Cook, M. J., Nasset, E. S., Karhausen, L. R., Howells, G. P., et.al., 1975. Report of the Task Group on Reference Men. International Commission on radiological protection No. 23. Pergamon Press Oxford.

[55] Carmona, A., Devès, G., Ortega, R., 2008. Anal. and Bioanal. Chemistry 390(6), 1585-1594.

[56] Holzner, C., Feser, M., Vogt, S., Hornberger, B., Jacobsen, C., et.al., 2010. Nature Physics 6,883-887.

[57] Lagomarsino, S., Iotti, S., Farruggia, G., Cedola A., Trapani, V. et al. Spectrochim.Acta.B 66 (2011) 834-840

[58] Vincze, L., Janssens, K., Adams, F., Rivers, M.L., Jones, K.W., 1995. Spectrochimica Acta B, 50B, 127-147.

[59] Golosio, B., Simionovici, A., Somogyi, A., Lemelle, L., Chukalina, M., et.al., 2003. Internal elemental microanalysis combining X-ray fluorescence, Compton and transmission tomography. J. of Appl. Phys. 94, 145-156.

[60] Adams, F., van Vaecka, L., R. Barrett, Spectrochim.Acta Part B 60 (2005) 13.

[61] Sayre, D., Kirz, J., Feder, R., Kim, M.D., Spiller, R. Science 196 (1977) 1339.

[62] Weiss, D., Schneider, G., Niemann, B., Guttmann, P., Rudolph, D., et al. Ultramicroscopy 84 (2000) 185.

[63] Larabell, C.A., Le Gros, M.A. Mol.Biol.Cell 15 (2004) 957.

[64] Howells, M.R., Beetz, T., Chapman, H.N., Cui, C., Kirz, J., et al. J. Electron. Spec. Rel. Phen. 170 (2009), 4-12.

[65] Williams, S., J.Microsc. 170 (1993) 155.

[66] R.M. Glaeser and K.A. Taylor, J.Microsc. 112 (1978), 127-138.

[67] Dubochet, J., Adrian, M., Chang J.J., Lepault, J., McDowall, A.W. Cryotechniques in Biological Electron Microscopy, edited by R.A. Steibrech and K. Zierold (1987), 114-131. Berlin:Springer-Verlag.

[68] Beetz, T. and Jacobsen, C., J. Synchr. Rad. 10 (2003), 280-283.

[69] Schneider, G. Ultramicroscopy 75 (1998), 85-104

[70] Maser, J., Osanna, A., Wang, Y., Jacobsen, C., Kirz, J. et al. J. Microsc. 197 (2000), 68-79.

[71] Martinez-Criado, G., Bohic, S., Cloetens, P., Kosior, E., Suhonen, H. et. al. J. Synchr. Rad. 19 (2012), 10-18

[72] Kosior, E., Bohic, S., Suhonen, H., Ortega, R., Devès, G. et al. J. Struct. Biol. 177 (2012), 239-247

[73] Devès, G. and Ortega, R. Nucl. Instr. and Methods in Physics Research Section B. 181 (2001), 460-464

[74] F. Watt, P.S.P. Thong, A.H.M. Tan, S.M. Tang. Nucl. Instr. and Methods in Physics Research Section B. 130 (1997) 188-192.

[75] Slatkin, D.N., Hanson, A.L., Jones, K.W., Kraner, H.W., Warren, J.B. Nucl. Instr. and Methods in Physics Research Section A. 227 (1984), 378-384.

[76] Kirz, J., Jacobsen, C., Howells. M. Q. Rev. Biophys. 28 (1995), 33 130

[77] Zhang, X., Jacobsen, C., Lindaas, S., Williams, S. J. Vac. Sc. Tech. B 13 (1995), 1477-1483.

[78] Maetz, M., Przybylowicz, W.J., Mesjasz-Przybylowicz, J., Schuessler, A., Traxel. K., Nucl. Instr. and Methods in Phys. Res. B 158 (1999) 292

[79] Meents, A., Gutmann, S., Wagner, A., Schulze-Briese, C. Proc. Natl. Acad. Sci. USA 107 (2010), 1094-1099.

[80] http://www.esrf.eu/UsersAndScience/Experiments/Imaging/ beamline-portfolio/CDR_UPBL04_future-ID16.pdf

[81] Fahimian, B.P., Mao, Y., Cloetens, P., Miao. J., Phys. Med. Biol. 55 (18) 2010, 5383-400.

[82] Daniel, M.C., Astruc, D. Chem. Rev. 104, (2004) 293-346.

[83] Ghosh, P., Han, G., De, M., Kim, C.K., Rotello, V.M. Adv. Drug Deliv. Rev. 60, (2008) 1307-1315

[84] Lewis, D.J., Bruce, C., Bohic, S., Cloetens, P., Hammond, S.P. et al. Nanomedicine (Lond). 2010 (10) 1547-57

[85] Kong, X.L., Qiao, F.Y., Qi, H., Li, F.R. Biotechnol. Lett. 12, (2008) 2071-2077

[86] Zheng, Y., Hunting, D.H., Ayotte, P., Sanche, L. Radiat. Res. 2008,169:19-27

[87] Thurn, K.T., Paunesku, T., Wu, A., Brown, E.M., Lai, B., et al. Small. 2009 Jun;5(11):1318-25

[88] Ridler, T.W., Calvard, S. IEEE Trans. System, Man and Cybernetics, SMC-8 (1978) 630-632.

[89] Jahn, K.A., Barton, D.A., Kobayashi, K., Ratinac, K.R., Overall, R.L. et al. Micron 43 (2012) 565-582

List of publications

E. Kosior, S. Bohic, P. Cloetens "Trace elements mapping at the sub-cellular level using X-ray fluorescence and phase contrast imaging" conf.proceed. ICOBTE 2011

G. Martinez-Criado, R. Tucoulou, P. Cloetens, P. Bleuet, S. Bohic, J. Cauzid, I. Kieffer, **E. Kosior**, S. Labouré, S. Petitgirard, A. Rack, J.A. Sans, J. Segura-Ruiz, H. Suhonen, J. Susini and J. Villanova "Status of the hard X-ray microprobe beamline ID22 of the European Synchrotron Radiation Facility" (2012) J. Synchr. Rad. 19, 1

E. Kosior, S. Bohic, H. Suhonen, R. Ortega, G. Devès, A. Carmona, F. Marchi, J.F. Guillet and P. Cloetens "Combined use of hard X-ray phase contrast and X-ray fluorescence microscopy for sub-cellular metal quantification" (2012) J. Struct. Biol. 177, 2

E. Kosior, P. Cloetens, G. Devès, R. Ortega, S. Bohic "Study of radiation effects on the cell structure and evaluation of the dose delivered by X-ray and α-particles microscopy." 2012, Appl. Phys. Lett. *in press*

E. Kosior, S. Bohic, H. Suhonen, P. Cloetens "Absolute zinc quantification at the sub-cellular level by combined use of hard X-ray fluorescence and phase contrast imaging techniques" conf.proceed. X-Ray Microscopy 2012, Journal of Physics: Conference Series (JPCS) *accepted*